UNIVERSITÀ
DEGLI STUDI
FIRENZE

School of
Mathematical, Physical
and Natural Sciences

Master Degree in Physics

Ultranarrow laser stabilization with long-distance optical-fiber link for experiments with Ytterbium ultracold gases.

Stabilizzazione di un laser ultra-stretto con collegamento in fibra ottica a grande distanza per esperimenti con gas ultrafreddi di Itterbio.

Advisor:
Leonardo Fallani

Candidate:
Francesco Poggiali

Academic year: 2014-2015

Contents

Introduction

Nowadays ultracold atoms are giving experimental answers to many open problems of general physics, such as condensed-matter and high-energy physics. In fact, they are naturally quantum simulators, in which the control of the atomic motion to the quantum level allows the production of quantum systems on demand and the precise measurement of their properties [15].

The basis of the reached progress is the realization and manipulation of ultracold atoms in optical lattices [2]. These are an ideal tool to accurately control the various properties of the atomic system, such as the mobility of the atoms in the lattice, the number of interacting particles per site, the system dimensionality and the precise amount of disorder. In particular, very important results have been achieved in many-body physics concerning the observation of quantum phase transitions [3] and in the quantum simulation of solid-state models due to the analogies between electrons in crystals and atoms in optical lattices [4].

Moreover, the possibility to "freeze" the motion of the particles trapped in the optical lattice has allowed the realization of spectroscopic measurements with very high accuracy of the atomic transition frequencies, basis of optical clock development [5].

These two research fields, the one related to many-body systems for quantum simulation and the one relative to ultraprecise spectroscopy measurements, were hardly connected each other until recent days. This separation was caused mostly by the very different experimental requirements: while at the basis of optical clocks realizations there is the atomic spectroscopy performed on samples of two-electron atoms with low densities and fast production cycles, the quantum simulation in atomic physics is possible due to Bose-Einstein condensation and Fermi degeneracy in atomic gases, especially alkaline metals, with high density values and much slower production rates.

A recent possibility for the union of these two fields is represented by the study of degenerate two-electron gases. This class of atoms is characterized by a metastable level $^3P_0$ connected to the fundamental state $^1S_0$ through a doubly forbidden transition, named "clock" transition since widely used to

realize optical lattice clock. In addition to the electronic state, the fermionic isotopes of these atoms exhibit a nuclear spin degree of freedom, that in these two states is decoupled from the electronic degree of freedom. The ability to coherently control with very-high precision these two degrees of freedom, the spin and the electronic state, makes two-electron atoms ideal candidates for a new class of quantum simulation experiments, e.g. for the study of quantum magnetism in two-orbital systems [9], or for quantum information applications [11].

However, the excitation of the clock transition poses severe requirements due to its extremely small linewidth (only a few mHz), that necessitates an extremely good stability of the excitation laser. For an experiment that is designed for quantum simulation it is difficult to use the atomic system itself as a self-reference for the clock laser, therefore an external frequency reference is required.

A very promising solution for this issue is related to the recent development of optical reference distribution systems through optical fiber links for use in atomic physics. These have already proved to be an useful tool in novel applications such as relativistic geodesy [6], where they could provide frequency references without need of a local microwave clock, and radioastronomy [7], linking and synchronizing antennas that may be tens of kilometers apart. Furthermore, the realization of giant gyroscopes based on optical fiber rings has been demonstrated [8].

This master thesis work has been realized as a part of a wider experiment running at *University of Florence-European Laboratory for Non-Linear Spectroscopy* (UNIFI-LENS), whose goal is to implement quantum simulation techniques with ultra-cold neutral Ytterbium atoms. In this context the subject of this thesis is the development of a novel technique for the stabilization of an ultranarrow laser source for experiments performed with fermionic Ytterbium ultracold gases trapped in three-dimensional optical lattices. For this purpose I have taken advantage of the optical fiber link between UNIFI-LENS and INRIM, which provides UNIFI-LENS with an absolute frequency reference coming from the national atomic clocks through the Italian Link for Time and Frequency (LIFT) infrastructure.

In chapter 1 I will present the main properties of Ytterbium for atomic physics and the experimental systems, the one at the Department of Physics and Astronomy in Florence and the optical fiber link infrastructure that connects INRIM and UNIFI-LENS. Then I will discuss the experimental techniques for the frequency measurements and comparisons through the use of a frequency comb that have been exploited in order to characterize the 578 nm laser (realized before this master thesis work) used to excite the doubly forbidden transition $^1S_0 \rightarrow ^3P_0$. Then in chapter 2 I will show the

system that I have implemented in order to stabilize the laser frequency shifts: a digital proportional-integral controller that realizes the stabilization to the INRIM absolute reference through a Direct Digital Synthesizer. In chapter 3 I will present the application of this new tool to the absolute frequency measurement of the $^1S_0 \rightarrow ^3P_0$ transition in ^{173}Yb, which has been performed for the first time with a precision of the order of ≈ 10 Hz, demonstrating the feasibility and utility of optical fiber links for ultracold atoms experiments.

Chapter 1

Yb experiment and optical fiber link

Ytterbium (Yb) is an important element for atomic physics, both for high-precision measurements and for quantum simulation experiments with ultracold degenerate gases. In Sec. 1.1 we will introduce the main properties of Ytterbium, with a particular focus on the $^1S_0 \rightarrow ^3P_0$ clock transition that will be studied in this thesis work: we will describe its properties and its diverse applications in atomic physics experiments. In Sec. 1.2 we will describe the procedures that allow the production of fermionic ^{173}Yb gases in the laboratories of the Department of Physics and Astronomy of the University of Florence (UNIFI).

In order to exploit the clock transition of Ytterbium, because of its extremely small linewidth, it is fundamentally important to have access to an ultrastable frequency reference. For this goal I have exploited a collaboration between UNIFI-LENS and the *Istituto Nazionale di Ricerca Metrologica* (INRIM) in Turin, demonstrating the remote stabilization of the Yb clock laser in Florence thanks to absolute frequency dissemination from INRIM.

In Sec. 1.3 we will describe the Italian Link for Time and Frequency (LIFT) infrastructure, consisting in a 642-Km long optical fiber that connects the two institutes. In Sec. 1.4, 1.5 and 1.6 we will give an outlook of several instruments and techniques that have been used for the laser stabilization,including a discussion on the behavior of the optical frequency comb that allows comparison between distinct laser frequencies and their reference to a primary time standard.

1.1 Ytterbium in atomic physics experiments

In this section we present the main properties of Ytterbium, discussing in particular the applications given by the $^1S_0 \rightarrow ^3P_0$ clock transition both in high-precision spectroscopic measurements and in quantum simulation experiments with ultracold atomic gases.

1.1.1 Ytterbium properties

Ytterbium is a metal belonging to the group of lanthanides having atomic number 70 and seven stable isotopes (see tab. 1.1), divided between bosonic (^{168}Yb, ^{170}Yb, ^{172}Yb, ^{174}Yb, ^{176}Yb) and fermionic (^{171}Yb, ^{173}Yb). It is characterized by an electronic configuration in the fundamental state of [Xe] $4f^{14}6s^2$; with two electrons in the most external orbital, it presents an energetic level structure similar to alkaline-earth elements and Helium. In fact, its levels scheme can be divided in two branches, having total spin angular momenta S = 0, spin singlet group, and S=1, spin triplet group. The basic structure with the first levels is shown in Fig. 1.1.

Table 1.1: Stable isotopes and principal properties of Ytterbium. [31]

Isotope	**Abundance** (%)	**Nuclear spin**	**Nuclear magn. moment** $[\mu/\mu_N]$
168	0.13	0	0
170	3.05	0	0
171	14.3	1/2	+0.4919
172	21.9	0	0
173	16.12	5/2	-0.6776
174	31.8	0	0
176	12.7	0	0

Among the various transitions that characterize the Ytterbium spectrum, those that connects the $|^1P_1\rangle$ e $|^3P_1\rangle$ with the ground state (see Fig. 1.1) are particularly important for experiments in ultracold atom physics. The allowed transition $^1S_0 \rightarrow ^1P_1$ exhibits a wavelength of 398.9 nm [51] and a natural linewidth of $2\pi \times 28$ MHz [31], corresponding to a mean lifetime of the excited level of $\approx$ 5.5 ns. The short mean lifetime of the level $|^1P_1\rangle$ allows us to use it both for the laser deceleration of atomic beams with the aid of a Zeeman slower and to perform absorption imaging processes

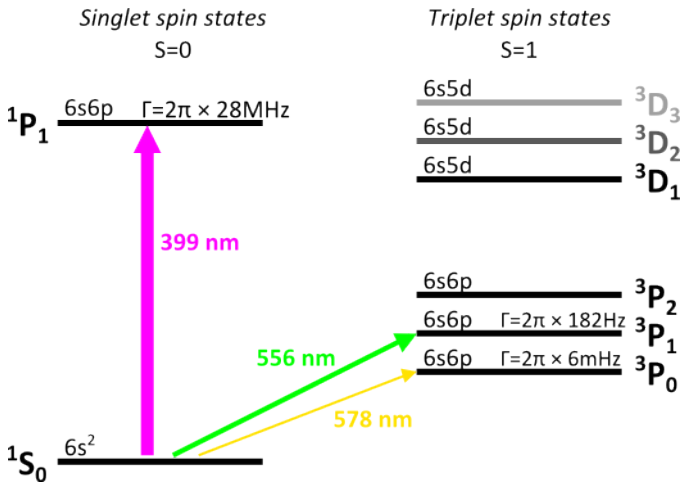

Figure 1.1: Scheme of the first excited levels of the Ytterbium with some relevant transitions following.

on ultracold atomic clouds exploiting 398.9 nm laser light. The $^1S_0 \rightarrow ^3P_1$ is an inter-combination transition because it violates the selection rule of spin conservation $\Delta S = 0$. However, this selection rule is relaxed in atoms with large atomic number ($\geq$ 30) where the spin-orbit coupling becomes comparable with respect to the other terms of the atomic Hamiltonian, and this transition becomes weakly allowed. It is characterized by a wavelength $\lambda = 555.8$ nm [51] and a mean lifetime $\Gamma = 2\pi \times 182$ kHz and find application in the cooling and trapping of Ytterbium atoms through Magneto-Optical Traps (MOTs).

The most relevant feature of Ytterbium for this thesis is the presence of a metastable state $|^3P_0\rangle$, with a radiative lifetime > 20 s. The $^1S_0 \rightarrow ^3P_0$ "clock" transition, also represented in Fig. 1.1, is a doubly forbidden ($\Delta S \neq 0$ and $J = 0 \rightarrow J' = 0$) transition at $\lambda = 578$ nm, with $\Gamma = 2\pi \times 6$ mHz, and it will be widely discussed later in chapter 3. The long mean lifetime allows us to consider the $^3P_0$ state stable within the experimental time-scale, making it an ideal candidate both for the encoding of quantum information and as an additional degree of freedom for quantum simulation experiments.

Finally, the two clock states $|^1S_0\rangle$ and $|^3P_0\rangle$ are weakly affected by an external magnetic field and its perturbations, which would generate undesired decoherence into the system. In fact, the interaction with the magnetic field B is given at the first order by the Zeeman Hamiltonian:

$$H_z = (-\mu_B g_J \mathbf{J} + \mu_N g_I \mathbf{I}) \cdot \frac{\mathbf{B}}{h} \tag{1.1}$$

with $\mu_B = e\hbar/2m_e$ and $\mu_N = e\hbar/2m_p$ the Bohr and nuclear magneton, g_J and

g_I the electronic and nuclear g-factors, $\mathbf{J} = \mathbf{L} + \mathbf{S}$ and $\mathbf{I}$ the total electronic and nuclear angular momentum, respectively. Since $|^1\mathrm{S}_0\rangle$ and $|^3\mathrm{P}_0\rangle$ have both a zero total orbital angular momentum J, the first term in Eq. 1.1 is null. For bosonic isotopes, which have also nuclear momentum $I = 0$, the ground state is completely insensitive to external magnetic fields. In fermionic isotopes, $I \neq 0$ and the clock states exhibit a small nuclear spin Zeeman shift, suppressed by a factor $g_I \approx \mu_N/\mu_B \approx 1/2000$ with respect to that of a level with nonzero electronic angular momentum. The Zeeman shift will be studied in detail in Sec. 3.3.2.

1.1.2 Applications of the Yb $^1\mathrm{S}_0 \rightarrow ^3\mathrm{P}_0$ clock transition

Here we review some of the most important applications of the Ytterbium $^1\mathrm{S}_0 \rightarrow ^3\mathrm{P}_0$ clock transition in atomic physics experiment.

The first application concerns the possibility of performing high-precision spectroscopic measurements, taking advantage of the extremely small natural linewidth of the transition. Together with Strontium, Yb is one of the most promising candidates for the realization of optical lattice clocks. In these experiments an optical lattice is needed in order to enter the Lamb-Dicke regime (see Sec. 3.3.1) and control several systematic effects. The optical lattice is produced with laser light at the "magic wavelength" (see Sec. 3.3.3) for which the light shift on the two clock levels is the same and the transition frequency is independent from the presence of a trapping light. For Ytterbium this wavelength is 759 nm and can be conveniently produced by semiconductor or solid-state lasers.

High precision frequency measurements with bosonic ^{174}Yb have been reported [10], while fermionic ^{171}Yb has proved to be an ideal system for optical clocks with 10^{-18} stability [12]. An ^{171}Yb optical clock is also operating at the Italian Metrology Institute INRIM.

A distinct field of application of the Ytterbium clock transition, pioneered in experiments at the Department of Physics and Astronomy of the University of Florence (UNIFI), concerns the realization of new classes of quantum simulation experiments. Fermionic ^{173}Yb is particularly suited for these experiments, because of its interesting collisional properties. On one hand, the purely nuclear spin in both the $^1\mathrm{S}_0$ and $^3\mathrm{P}_0$ state causes the independence of the scattering length on the particular nuclear spin states involved in the collisions. This property is at the basis of the SU(N) symmetry exhibited by these atoms (where N is the number of spin states, up to $N = 2I + 1$ for ^{173}Yb, which has a nuclear spin $I = 5/2$), which may find applications in quantum simulations of condensed-matter and high-energy models [13]. On the other hand, the existence of two distinct degrees of freedom - the nuclear

spin and the electronic state - is responsible for new interaction processes which are absent in alkali atoms. Recent measurements performed on the UNIFI Ytterbium experiment have evidenced the presence of a strong spin-exchange interaction between atoms in different electronic states, driven by the difference in scattering lengths between symmetric and antisymmetric two-particle electronic states [34]. As an example, in Fig. 1.2 we show the coherent oscillation of the magnetization in the ground state induced by this spin-exchange interaction.

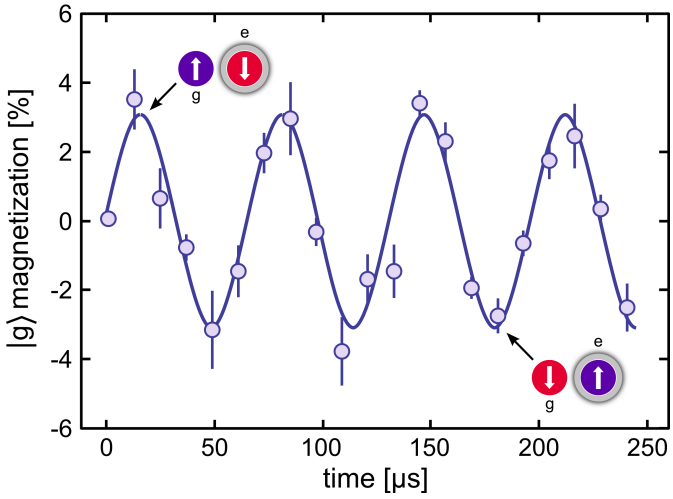

Figure 1.2: Example of spin-exchange dynamics. Magnetization of the ground state $|g\rangle = {}^1\mathrm{S}_0$ as a function of time: the oscillation is induced by a coherent exchange of spin between $|g\rangle = {}^1\mathrm{S}_0$ and $|e\rangle = {}^3\mathrm{P}_0$ atoms (as indicated by the up and down arrows). Taken from [34].

In addition, very recent experiments performed on the same setup have shown the existence of a magnetic Feshbach resonance between ${}^1\mathrm{S}_0$ and ${}^3\mathrm{P}_0$ atoms, that could be exploited for the investigation of fermionic superfluidity in a new system made by atoms in different electronic states [14].

All these applications require the initial preparation of a quantum gas of ${}^{173}\mathrm{Yb}$ atoms in the electronic states ${}^1\mathrm{S}_0$ and ${}^3\mathrm{P}_0$. This can be obtained by using the ultranarrow clock transition and realizing appropriate excitation pulses.

Finally, the Ytterbium clock transition could find applications in many other quantum simulation experiments, for instance for the generation of spin-orbit coupling between atoms in different electronic states [15] or for the high-resolution detection of interesting many-body states.

All these quantum simulation applications are pursued in the UNIFI Ytterbium experiment. The next section is devoted to a brief illustration of the

experimental setup.

1.2 Experimental setup and ultracold Ytterbium gas preparation

In this section we synthetically describe the experimental setup used to generate and trap an ultracold degenerate ^{173}Yb gas. For further details the reader can refer to [16, 17].

A sample of Ytterbium with natural isotopic composition placed inside an oven at the temperature of ≈ 500 °C represents the atomic source for the mono-atomic gas. The atoms are channeled in a square array of 100 microtubes and exit the oven producing a collimated atomic beam with a thermal velocity of the order of 300 m/s. A sketch of the following experimental setup is represented in Fig. 1.3. The atomic beam is then decelerated by a Zeeman slower to velocity of ≈ 20 m/s using a laser beam at the wavelength of 399 nm, exploiting the $^1S_0 \rightarrow {}^1P_1$ transition. After the Zeeman slower, the

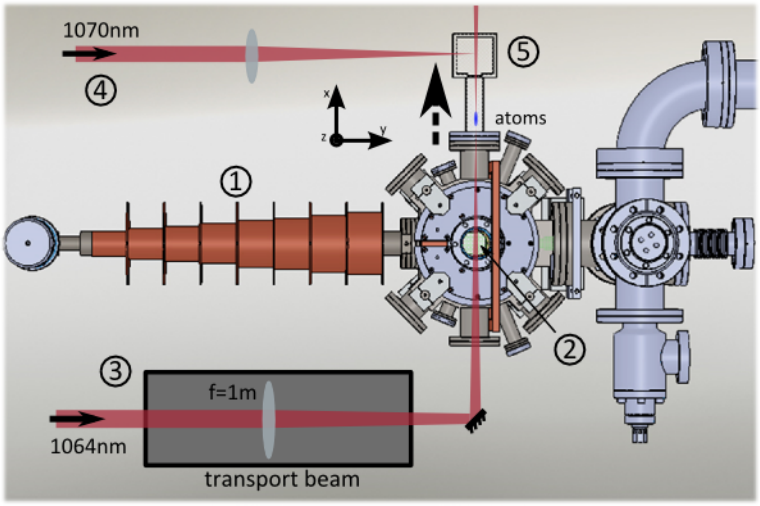

Figure 1.3: Sketch of the experimental setup for the cooling and trapping of a cloud of Ytterbium atoms. The Zeeman slower stage (1), the MOT cell (2), the air-bearing translation stage (3), the crossed dipole trap (4) and the glass cell (5) are shown.

atoms are captured in a magneto-optical trap (MOT) inside a MOT chamber. Here they are further cooled exploiting the interaction with three pairs of counterpropagating beams (a pair for every spatial direction) at the characteristic wavelength of the intercombination transition $^1S_0 \rightarrow {}^3P_1$, 556 nm.

A quadrupole magnetic field allows us to trap atoms at the intersection of the six laser beams. Changing the MOT and Zeeman slower beams frequency, thanks to the isotopic shift, it is possible to decide which isotope of Ytterbium to trap and discard the others. For the experimental purposes of this thesis work we are interested in ^{173}Yb and the following values are relative to this isotope.

The duration of the MOT stage is 20 s, after which the number of atoms at the center of the trap is roughly $N \approx 4 \cdot 10^8$, with a temperature of 30 ± 1 μK. The cloud is then transferred in a "resonator": a one-dimensional optical lattice at 1064 nm realized inside a resonating cavity placed at the center of the MOT chamber; the efficiency of this process is about 80%. Then, by lowering the lattice depth through two exponential ramps in order to maximize the phase space density, we realize a first stage of evaporative cooling that leads to an atom number $N \sim 10^7$ at a temperature $T \simeq 5$ μK. The basis of the evaporative cooling is the thermalization of the atom sample that happens through s-wave collisions, and in this case it is allowed because the atoms are trapped in a mixture of different spin states and therefore are distinguishable each other.

Finished the cooling, the atoms are loaded in an off-resonant Optical Dipole Trap (ODT) generated by a laser beam at 1064 nm and characterized by a waist of 30 μm. Once loaded in the ODT the atoms are transferred inside a glass cell placed 26 cm away from the MOT chamber center. A sketch of this procedure is illustrated in Fig. 1.3. The transport has a duration of 2 s and is realized moving the atomic cloud along with the trap waist, mechanically shifted by a lens mounted on an air-bearing translator. The efficiency of the transport is around 80% ($N \approx 2 \cdot 10^5$) and induces an heating of just 2.5 μK [18]. Once the sample arrives at the center of the glass cell, a second beam at 1070 nm, orthogonal to the first, is switched on in order to realize an optical crossed trap. Reducing the laser beams power, again with exponential ramps, we perform a second evaporative cooling stage for a time of 4 s that allows us to obtain a degenerate Fermi gas of roughly 10^5 atoms at a temperature of 0.15 T_F, with $T_F \simeq 100$ nK the Fermi temperature. In addition to these processes, an optical pumping procedure allows us to prepare different mixtures containing a well defined number of spin states. The method will be discussed in detail in Sec. 3.2.1.

Finally, the atoms are loaded in a three-dimensional optical lattice realized with laser light at the magic wavelength 759 nm. The lattice depth is controlled by changing the power of the laser beams that generate the lattice: it is possible to obtain a depth up to 40 E_R, with $E_R = h \times 2.0$ kHz the recoil energy of an ^{173}Yb atom. The ultracold Ytterbium gas trapped in the optical lattice is the starting point for the experimental routines discussed in

Ch. 3. The imaging process, performed evaluating the atoms number in the electronic ground state $^1S_0$ through the absorption of 399 nm laser light, will described in Sec. 3.2.2.

1.3 Long distance optical fiber link

In this thesis we describe the development of a remote stabilization system for the experimental setup described in the previous section, that will allow us to perform high-precision frequency measurements on the Ytterbium clock transition. The comparison between different frequency references is indeed necessary in order to realize high precision spectroscopy and frequency (or time) standards. This is the basis of the achievement of atomic clocks with a relative uncertainty of the order of 10^{-18}. To obtain these precision levels there is a fundamental issue to solve: the frequency distribution. In fact, atomic clocks are unlikely transportable, hence these systems are generally compared "at a distance".

In this section I'll describe the techniques implemented for these purposes and in particular the long-distance optical fiber link realized between *Istituto Nazionale di Ricerca Metrologica* (INRIM) in Turin and *University of Florence-European Laboratory for Non-Linear Spectroscopy* (UNIFI-LENS).

The first system implemented was microwave links to satellites that has contributed to the realization of the Universal Coordinated Time (UTC) and of the International Atomic Time (TAI) linking more than 250 clocks located all over the world. In this case, the accuracy of the primary time and frequency standards is about 2 x10^{-16} [19]. These are related through microwave links for time transfer, based on the US Global Positioning System (GPS), or on the network for Two-Way Time and Frequency Transfer (TWTFT). These systems allow us to achieve a stability in the atomic clocks comparison of 10^{-14} for an averaging time of about a day. Therefore, in order not to be limited by the link uncertainty, a time of measurements of the order of 20 days is necessary. Still, this would not be enough to reach the uncertainty limits of optical clocks, currently well below 10^{-17}. In any case these techniques still remain the only ones for implementing ultra-distance and intercontinental links.

It is evident that, in order to exploit the opportunities given by optical clocks, the implementation of more precise frequencies comparisons is necessary. This has been realized since the early 2000s [20] by the development of optical fiber links. This technique has reached a stability of 10^{-13} at 1 s averaging time and consequently a resolution of the order of 10^{-18} in the clocks comparisons for few hours of integration time. The technique uses

the telecommunications optical fiber infrastructure exploiting a single International Telecommunication Union (ITU) fiber channel and therefore it is compatible with the data transfer. The signal consists in a continuous and non modulated carrier wave wherein the useful information for the metrological optical link is the frequency of the carrier itself that is measured at the input and output of the fiber. There are several applications of this technique in various research field, such as geodesy and radioastronomy [6, 7], where they could provide frequency references without need of a local microwave clock and synchronize antennas for astronomical measurements that may be tens of kilometers apart and the realization of giant fiber optic gyroscopes [8].

Showed the evident precision benefits that we can get, it is fair to point out the two principal issues that affect this system. The first is the fiber signal attenuation due to intrinsic properties or impurities of the medium and to geometrical architecture of the fibers, that is of the order of 0.25 dB/km. This implies that for long-distance fiber links a re-amplification of the signal along the way is necessary, causing a second noise generation due to the amplifier itself. Both these processes have the effect to reduce the signal noise ratio (SNR) and to potentially limit the employment of this technique. Therefore to solve these problems generally bidirectional amplifiers are placed along the fiber path and, in correspondence of those, bandpass filters are located in order to reduce the resulting noise. Moreover, for fiber links of several kilometers there are many causes for optical path length variations such as acoustic and seismic noise or mechanical and temperature stresses, that in particular cause a refractive index variation; all of these make the signal transfer less stable. A solution for this problem consists in the stabilization of the optical path length with an interferometric technique, which is based on the self beating between part of the signal that makes a round trip through the fiber and a sample of the same light before the fiber; this technique is called "fiber noise cancellation" and will be discussed in detail in section 1.3.2.

The infrastructure that has been used during this thesis work is the optical fiber link of 642 km named Italian Link for Time and Frequency (LIFT), implemented in Italy [21] [22]. Before UNIFI-LENS in Florence, LIFT connects INRIM to several Italian scientific poles providing a reference signal to the Institute for Photonics and Nanotechnologies in Milan, to the Institute for Radio-Astronomy in Medicina (Bologna); finally it reaches UNIFI-LENS for precision measurements in atomic and molecular physics. A scheme of its path is represented in Fig. 1.5. LIFT will also connect Italy to the forthcoming European fiber network.

This link is composed by three main parts: the INRIM setup for the generation and the control of the reference signal at 1542 nm, the real fiber link

between Turin and Florence and the regeneration setup present in Florence at the Department of Physics and Astronomy. Now we will discuss them singularly in detail.

1.3.1 INRIM link setup

The first part consists in the generation of an optical signal that should be a frequency standard and, at the same time, be transportable far away through the telecommunications infrastructure.

The starting point is a benchtop Distributed-Feedback (DFB) fiber laser (FL) source Koheras-Adjustik laser, with emission wavelength centered on the channel 44 of the ITU grid (1542.14 nm) with a linewidth of about 10 kHz. The important feature of this laser is the possibility to exploit the standard optical fiber net used in telecommunications for the distribution of its signal. The details of this optical source are presented in [23, 24]. In

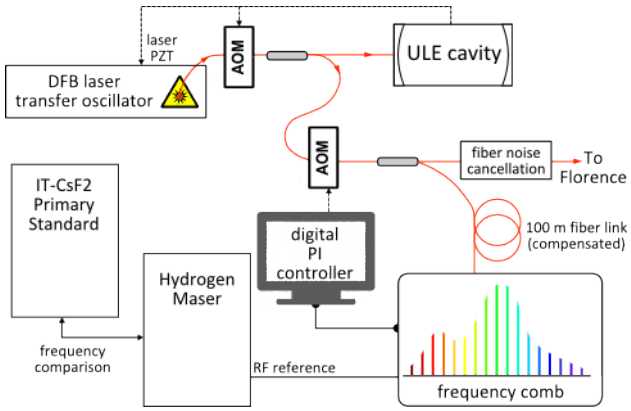

Figure 1.4: Block scheme of the setup for the generation of the 1542.14 nm signal, referred and stabilized to the italian primary time standard "IT-CsF2" Cesium fountain.

order to obtain a further narrowing of the emission linewidth it is necessary to stabilize the laser frequency on the fundamental mode of a Fabry-Pérot (FP) cavity with high finesse (ULE cavity). The basic scheme is reported in Fig. 1.4. This experimental technique is analogue to that we will discuss in details in Sec. 2.1. The resulting linewidth is of the order of 30 Hz.

In order to transfer the accuracy of a frequency standard to the laser frequency, the latter is compared with the microwave frequency of a Hydrogen maser (HM), characterized by a high stability, using a frequency comb with the technique that will be shown in Sec. 1.5.1. A stabilization system is implemented with the same principle of operation as the one implemented in

this thesis work and illustrated in Sec. 2.3. After the stabilization, the FL inherits the same accuracy of the maser. Finally, the chain for the reference generation is completed by a comparison system between the HM and the italian primary standard for time and frequency represented by the Cesium fountain "IT-CsF2". In fact, even the maser has some fluctuations in the course of a day, with a relative shift of its frequency of the order of $0.5 \cdot 10^{-15}$, and therefore a periodic comparison with the Cesium fountain is realized in order to monitor and measure it. This frequency mismatch represents a bias on the reference frequency signal distributed through the long-distance optical fiber link that should be manually corrected for its value at the time of the remote measurement.

1.3.2 LIFT fiber link

Once the signal is generated and referred to the absolute reference of the Cesium fountain, it is sent through the infrastructure based on a dedicated 642-km long optical fiber (see Fig. 1.5); due to the long distance, it exhibits 171 dB losses, that are compensated by nine bidirectional Erbium Doped Fiber Amplifiers (bEDFA), placed on the track as shown in table 1.2. These

Figure 1.5: Path of the optical fiber link from Turin to Florence. The green arrows represent the bEDFAs along the path.

are characterized by a gain up to 20 dB. However, because of the residual spontaneous emission of the gain medium, they also produce a noise that is optically amplified by the process of stimulated emission inside the EDFAs

Table 1.2: Length, optical losses, and amplification of the various sections on the LIFT fiber path. Stars indicate the bEDFAs placement.

From:	**To**:	**Length** [km]	**Loss** [dB]	**Gain** [dB]
INRIM	Torino v. Lancia	25	-9	
Torino	Santhià*	67	-18	19
Santhià	Novara*	77	-18	16
Novara	Lainate*	50	-15	13
Lainate	Milano*	60	-18	20
Milano	Piacenza*	67	-16	17
Piacenza	Reggio Emilia*	94	-23	19
Reggio Emilia	Bologna*	74	-19	16
Bologna	Rioveggio*	38	-10	17
Rioveggio	Firenze*	72	-18	19
Firenze	LENS	18	-7	
	Total	**642**	**-171**	**156**

themselves; this process is named Amplified Spontaneous Emission (ASE). In our case the bEDFAs affect the signal with an ASE noise of about -35 dBm at 0.5 nm from the coherent carrier at 1542.14 nm for a 18 dB gain and on a bandwidth of 0.1 nm. In order to reduce the ASE, the signal is filtered on a bandwidth of 0.8 nm by eight telecom optical filters that prevent the amplifiers gain saturation and the onset of auto-oscillations.

As we mentioned, there is a deterioration of the delivered signal due to mechanical stresses and temperature variations of the fiber and therefore the link is phase-stabilized through the Doppler noise cancellation technique. The setup is shown in Fig. 1.6. A fiber beam splitter divides the optical signal coming from the ultrastable 1542.14 nm laser into two parts: only ≈ 1 mW of optical power are delivered to Florence (in order to avoid saturation effects in the amplifiers due to the ASE noise), after a frequency shift of 40 MHz operated by an AOM; the remaining power is reflected by a Faraday mirror (FM1), providing the local reference for the stabilization technique. The characteristic of this mirror is to rotate the beam polarization of the reflected beam by 90° with respect to the incident beam polarization. In the remote laboratory, the delivered signal passes again through an AOM and a fiber beam splitter respectively: part of the signal is extracted and represents the ultrastable reference, while the other is reflected back to INRIM by a Faraday mirror (FM2). The two AOMs are used in order to respectively

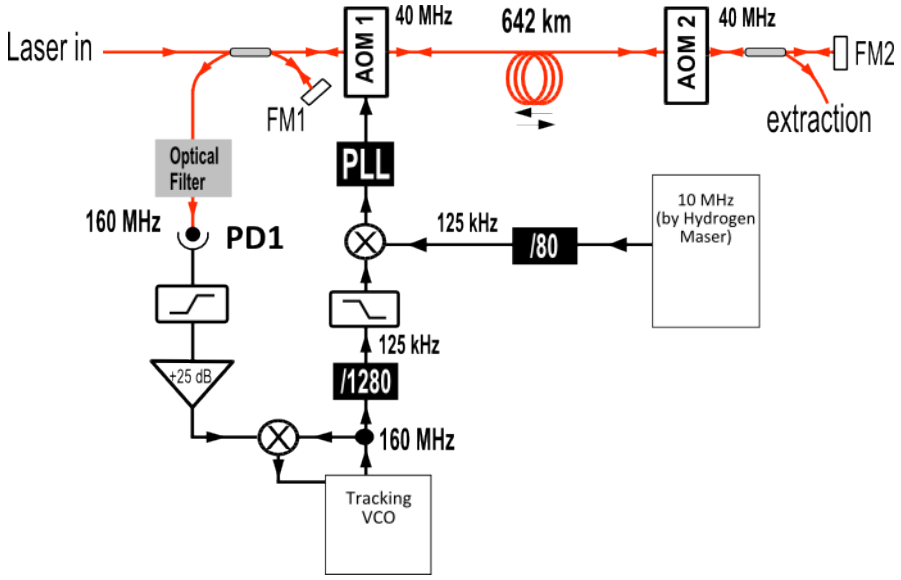

Figure 1.6: Sketch of the setup for the fiber noise cancellation implemented at INRIM and UNIFI.

separate in frequency the signal that has done a round-trip from the part that is reflected by FM1 and to distinguish the real signal of the LIFT from undesired backreflections along the fiber link. At INRIM, the round-trip signal is phase-compared to the local reference on photodiode PD1. The two FMs allow us to maximize the polarization alignment of the two beatnote branches in order to maximize the beatnote on PD1. This 160 MHz beatnote (corresponding to the frequency shift induced by the four passages through the AOMs) contains the information about the noise added by the fiber on the round trip and it is used to stabilize the fiber-link optical path with a phase-locked loop (PLL), realized with the aid of the Hydrogen maser as a local oscillator, acting on AOM1.

In order to perform the correction of the fiber noise, ideally, one would need a monochromatic optical signal, in order not to introduce unwanted noise induced by phase fluctuations. However, any real light source is characterized by a finite coherence time, that is:

$$t_c = \frac{1}{\Gamma} \tag{1.2}$$

where Γ is the linewidth of the laser. This in turn is related to the quantity called coherence length by:

$$l_c = n\frac{c}{\Gamma} \tag{1.3}$$

with n refractive index of the medium in which the light propagates. l_c represents the length under which the phase difference between two points of the wavefront is constant. It is evident that, for a correct phase comparison between the signal that has traveled the round-trip and the original one, the coherence length must be greater than the path length of the fiber link. In our case in the limit in which they are equal, the laser linewidth $\bar{\Gamma}$ should be of the order of:

$$\bar{\Gamma} \simeq 1.5 \frac{3 \cdot 10^8}{1284 \cdot 10^3} \text{ Hz} \simeq 2\pi \times 56 \text{ Hz} \tag{1.4}$$

where we have chosen as refractive index $n = 1.5$ as order of magnitude for the value relative to the fiber.

We note that, even in presence of an ideal laser, the finite propagation time along the fiber links determines a finite bandwidth for the correction system. $\bar{\Gamma}$ represents the inverse of the time that the light takes to make a round-trip and therefore it is also the bandwidth limit for the fiber noise correction.

With the implemented techniques for the generation and the stabilization of the signal, the LIFT link achieves a short-term instability of $1 \cdot 10^{-14}$ at 1 s in a 1 Hz bandwidth [22]. The stability is limited by the loss of phase coherence given by cycle slips on the PLL, that affect both the instability and the inaccuracy of the link. The rate of the cycle slips mainly depends on the signal-to-noise ratio of the beatnote.

1.3.3 LENS link setup

Thanks to the Cesium reference and to the fiber noise cancellation system the signal coming from INRIM has an high accuracy and stability, but is too weak (about 100 nW of power) for a further distribution that would be required for the various experiments performed at LENS-UNIFI that could exploit the LIFT. For this reason, in the laboratory at the Department of Physics of UNIFI where the signal arrives a regeneration system, schematically represented in Fig. 1.7, is implemented. The setup is primarily composed by a laser module built by Redfern Integrated Optics (RIO) that emits a carrier wave with power 1 mW at the same wavelength of the signal coming from Turin. Then this source is locked to the INRIM reference with a PLL setup that exploits a 10 MHz signal obtained by a GPS reference. We note that the PLL lock adds an offset of -100 MHz to the original frequency coming from the link. Part of the signal of the local laser is extracted and sent to the laboratory 69 of the Department of Physics and Astronomy ("Ytterbium

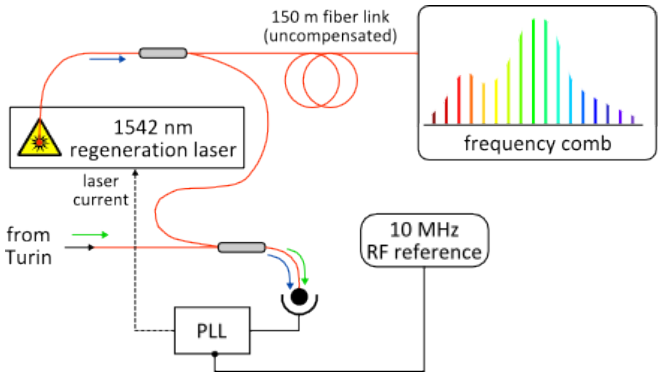

Figure 1.7: Block scheme of the signal regeneration setup that sends the INRIM signal to the frequency comb of the "Yb" laboratory, where it provides the reference for the calibration of the local 578 nm laser.

lab") through an optical fiber of about 150 m uncompensated[1]. This light provides the reference for the stabilization of the local 578 nm laser for the excitation of the $^1S_0 \rightarrow ^3P_0$ transition in Ytterbium, via an "optical lock" technique made possible by the use of a frequency comb.

1.4 Frequency measurements with a frequency comb

After showing the structure and the characteristics of the long-distance optical fiber link between INRIM and UNIFI-LENS, in this section we discuss the use of an optical reference for the frequency measurement of other laser sources through the use of a frequency comb. For more details, both theoretical and technical, we refer to [25].

The principle of operation of this instrument is quite simple and could be simply understood also by referring to Fig. 1.8. A frequency comb is based on a mode-locked pulsed laser, characterized in the time domain by gaussian pulses, with distance ΔT between the wavetrains, pulse duration Δt (defined as the Full Width Half Maximum (FWHM) of the envelope) and a carrier-envelope phase shift $\Delta\phi$ between two consecutive pulses. In the Fourier-transformed space, the frequency domain, we obtain a series of equispaced emission lines with an overall envelope with a width Δf equal to:

$$\Delta f = \frac{1}{2\sqrt{2\ln 2}\Delta t} \tag{1.5}$$

[1] We have verified that this additional fiber path does not introduce a significant noise on the laser frequency.

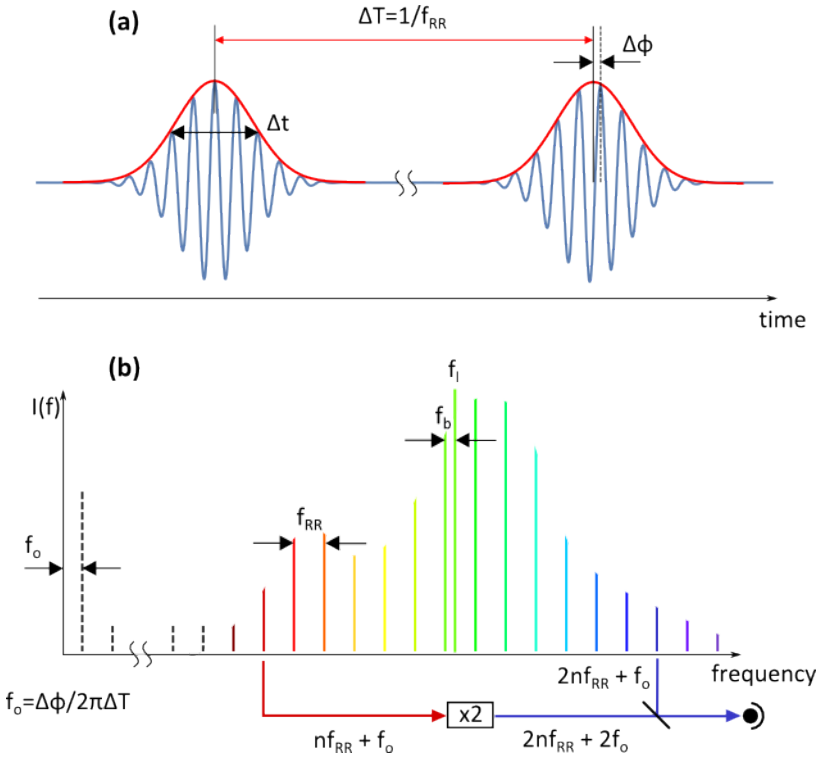

Figure 1.8: Sketch of the behavior of a pulse laser that generates a frequency comb. **(a)** Representation of the electric field in the time domain. **(b)** Intensity of the spectrum of the laser, corresponding to the Fourier transformed representation of the time domain. There is also a block scheme of the $f-2f$ technique for the f_o measurement (see Sec. 1.5).

where we have exploited the property of the Fourier transform of a gaussian distribution. Moreover, the distance between two consecutive peaks is the inverse of the distance in time between two consecutive pulses, i.e.:

$$f_{RR} = \frac{1}{\Delta T} \tag{1.6}$$

where f_{RR} is called "repetition rate" frequency. The phase shift instead corresponds to a carrier–envelope offset frequency: it is the rate at which the peak of the carrier frequency slips from the peak of the pulse envelope on a pulse-to-pulse basis; this "offset frequency" f_o is equal for every frequency components and is:

$$f_o = \frac{\Delta\phi}{2\pi\Delta T} \tag{1.7}$$

As said, we obtain a real frequency comb, with every n peaks as teeth all equal distant. The total number of teeth N of the frequency comb spectrum is

given by the ratio between the width of the comb and the frequency difference between consecutive peaks:

$$N = \frac{\Delta f}{f_{RR}} \tag{1.8}$$

Furthermore, the absolute frequency f_n of the n-th tooth is univocally defined as a function of the repetition rate and offset frequency:

$$f_n = n f_{RR} + f_o \tag{1.9}$$

If we consider the characteristics of some typical pulsed lasers that form the sources for frequency combs, for example $\Delta T \simeq 10\ ns$, we note that f_{RR} and f_o are both in the RF-microwave range.

Known the value of the repetition rate and offset frequency, we can exploit the frequency comb as a ruler in order to measure the frequency f_l of any other laser source that emits in the range Δf, i.e.:

$$f_l = n' f_{RR} + f_o + f_b \tag{1.10}$$

where n' is the number of the comb's closest tooth, that can be measured through a wavelength-meter with a resolution ≈ 100 MHz, and f_b is simply the difference between the n'-th tooth frequency and f_l, that can be measured by analizing the beatnote between the laser and the frequency comb. However, the precision and accuracy with which we know the repetition rate and the offset limits the uncertainty of every absolute frequency measurement performed with the frequency comb.

Everything said applies to an ideal pulsed laser. A first difference with respect to a real frequency comb is that the teeth intensity envelope is not a perfect gaussian, but there are frequency intervals within which the intensity profile exhibits dips. In fact it reflects the gain curve of the gain medium of the laser and the response of the photonic crystal fibers that are used to broaden the pulsed laser spectrum. Even more, for a pulse laser the distance in time and the duration of the various pulses are prone to fluctuations, that implicate that both f_{RR} and f_o should be stabilized in order to maintain the "ruler" for the f_l measurement constant in time.

To evaluate and stabilize them it is necessary to rely on an external frequency reference, and their evaluation is as precise as the reference signal. At this point the importance to have an absolute frequency available for this task can be understood.

1.5 Comb parameters evaluation and stabilization

In this section we discuss the various techniques for the measurement and stabilization of the repetition rate and offset frequency and the aftermath that they have on the uncertainty related to the measurement of an unknown laser frequency with a frequency comb.

Concerning the measurement of the offset frequency, the most common system is the so called "f-$2f$" technique, schematically represented in Fig. 1.8.

In order to implement it, a Δf that includes an octave is necessary. In general, the comb lines emitted by the mode-locked laser span a region up to only several tens of nanometers in a spectral region near 1 μm (typical values for a pulsed Ti:Sa laser). This spectrum is usually broadened using micro-structured optical fibers, where nonlinear optical effects (self phase modulation) are enhanced, in order to change the group velocity dispersion of the medium, which in turns affects the comb spectrum, making it span a full optical octave.

In this case, the lowest part of the frequency band is frequency-doubled by a nonlinear process of second harmonic generation (SHG). The frequency-doubled comb spectrum and the original octave-spanning spectrum are then compared, and the beatnote generated by all comb lines is:

$$\delta f = 2(m_i f_{RR} + f_o) - (n_i f_{RR} + f_o) \tag{1.11}$$

where m_i and n_i are generic teeth of the doubled and non-doubled spectra, respectively. Selecting with a low-pass filter only the lowest frequency peak of the beatnote spectrum (i.e. for each $n_i = 2m_i$) we obtain exactly f_o. It is clear that the evaluation of f_o is possible only with a known frequency for a comparison. Usually this method is implemented with a radio frequency synthesizer, which can also be used to stabilize f_o with a PLL technique. Since the offset frequency is related to the phase velocity dispersion inside the cavity, its stabilization is realized making a dispersion adjustment changing the laser pump power, whose variations slightly modify the refractive index of the active medium. For larger adjustments, intra-cavity wedges can be used. With common radio frequency sources it is possible to achieve easily a relative precision of f_o of the order of 10^{-10}.

Regarding the repetition rate, there are two different main systems for its evaluation that merit attention and therefore we discuss them in detail.

1.5.1 RF reference lock technique

The former technique to measure f_{RR} involves the use of a radio frequency (RF) reference and is called "RF lock" technique. Each pair of consecutive comb teeth generate a beatnote exactly at the frequency that separates them, typically a radio frequency. Measuring the signal with a photodiode and comparing it with another known RF frequency it is possible to extract the f_{RR} value and stabilize it (or its i-th harmonic) directly phaselocking to the RF reference; this active stabilization is realized by controlling the cavity length of the frequency comb laser. In practice, this is made by mounting one of the cavity mirrors on a piezo actuator.

At this point it is possible to measure the value of the beatnote between a generic laser and the closest tooth of the frequency comb, f_b, again with the mixing method with the RF reference, and extract the unknown value of f_l. From Eq. 1.10, the uncertainty Δf_l that affects this measurement is given by:

$$\Delta f_l = n' \Delta f_{RR} + \Delta f_o + \Delta f_b \tag{1.12}$$

with Δf_{RR}, Δf_o, Δf_b the error associated to the repetition rate, the offset, and the beatnote frequency respectively. Considering that $f_{RR} \approx 10^8$ Hz and that typical values of the laser frequency are in the visible or near infrared spectrum, it means that n' is of the order of 10^6. Thus, even if we consider an uncertainty on the evaluation and stabilization of the repetition rate frequency of the order of 1 mHz (i.e. a relative uncertainty better than 10^{-10}), we would have an error Δf_l of about 1 kHz. This represents the real limit of this technique.

1.5.2 Optical lock technique

Since the tooth number of the unknown source enters directly the uncertainty expression 1.12 as high multiplying factor, the best solution would be to stabilize directly the n'-tooth frequency. A system with this principle is based on the use of an optical reference and is the so called "optical lock" technique. Defining f_r the frequency of this reference, if we compare it to the frequency comb we obtain:

$$f_r = \bar{n} f_{RR} + f_o + f_{br} \tag{1.13}$$

where $\bar{n}$ is the number of the closest tooth with respect to f_r and f_{br} is defined as the difference between the reference and the $\bar{n}$-tooth frequency, which can be measured by analyzing the beatnote between the frequency comb and the optical reference. Since f_r is known, measuring and stabilizing f_{br} using a

RF as for the f_o stabilization, we can invert Eq. 1.13 and evaluate f_{RR}. The new expression for f_l as a function of the optical reference frequency is:

$$f_l = \frac{n'}{\bar{n}}(f_r - f_o - f_{br}) + f_o + f_b \tag{1.14}$$

and the uncertainty related to the repetition rate is:

$$\Delta f_{RR} = \frac{\Delta f_r + \Delta f_o + \Delta f_{br}}{\bar{n}} \tag{1.15}$$

The state of the art of the optical reference gives us a value for their absolute uncertainty $\Delta f_r \leq 1$ Hz. Despite it is the dominant term in the numerator in Eq. 1.15, in this case the value of Δf_{RR} is of the order of 10^{-6} Hz. This implies that Eq. 1.12 becomes:

$$\Delta f_l = \frac{n'}{\bar{n}}(\Delta f_r + \Delta f_o + \Delta f_{br}) + \Delta f_o + \Delta f_b \tag{1.16}$$

This time the multiplier factor is $n'/\bar{n} \simeq 1$ and therefore the global uncertainty on the unknown frequency is of the order of (the other quantities are generally known with smaller absolute uncertainties) $\Delta f_r \simeq 1$ Hz.

In the actual realization of the "optical lock" technique, f_{RR} is locked onto the optical reference in order to keep f_{br} stable. However, since in this case the f_{RR} phase noise is multiplied from the microwave to the optical domain and increases by over 100 dB, a faster actuator with respect to the piezoelectric is needed. Most often, an intra-cavity Electro-Optic Modulator (EOM) is used, whose bandwidth exceeds 200 kHz.

1.6 Use of FC1500-250-WG frequency comb

Illustrated the main properties of a frequency comb and the techniques that involve it for the frequency measurements, we describe now the instrument used for this purpose in this thesis work, a FC1500-250-WG producted by MenloSystems. It is basically composed by two main parts: one that includes the optical components and the rack with the electronics. We can see their pictures in Fig. 1.9.

The optical part is in turn divided in three modules. The first contains the real pulsed laser: a "femtosecond" Er^{3+} fiber laser, with a repetition rate $f_{RR} \approx 250$ MHz and a central wavelength ≈ 1.5 μm. The second module is dedicated to the amplification and the spectral broadening of the comb; the process happens inside an Erbium Doped Fiber Amplifier (EDFA) that permits non linear processes that change the dispersion of the medium; the

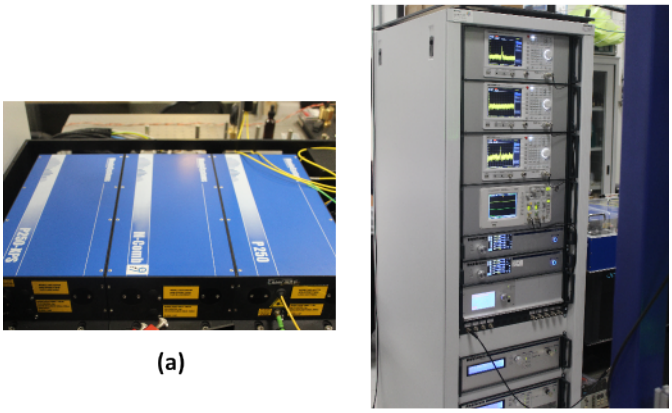

Figure 1.9: Pictures of the optical **(a)** and electronic **(b)** parts of the frequency comb.

generated frequency spectrum of the comb has a range of $\approx$ 1-2 μm. The third module is used to perform the SHG and the beatnote detection for the f-$2f$ measurement.

The electronic part is very articulate and we describe here only the key components without entering into details that are beyond this thesis work. First of all there are two Proportional Integral Derivative (PID) control systems for the stabilization of the offset frequency and the repetition rate, respectively represented by the Syncro-CEO and the Syncro-RRE boxes shown in Fig. 1.11. The offset lock consists in a PLL where the offset beatnote coming from the f-2f optical module is stabilized at $\pm$20 MHz exploiting a duplicated external 10 MHz reference. The sign of the offset is determined depending on the frequency-doubled teeth having a frequency higher or lower with respect to the teeth of the other part of the spectrum. An intra-cavity translation stage is used as the lock actuator.

For the repetition rate lock, we describe the procedure for the optical lock with the INRIM frequency reference. A dedicated optical fiber exits from the first laser module and is connected to an input of a dedicated Beat Detection Unit (Fig. 1.10). The fiber with the 1542 nm reference is connected to the other BDU input. Inside the BDU there is a fiber optimized for the propagation at 1542 nm and a fiber beam splitter. In this way the beatnote between the two signals is realized directly in the fiber, the output of which is connected to a photodiode that measures the beatnote signal. It is possible to optimize the beatnote signal-to-noise ratio through a micrometric screw acting on an attenuator . Then the repetition rate stabilization is realized

Figure 1.10: Beat Detection Units for the 1542.14 nm and 1156.84 nm.

thanks to a synthesizer that use the 10 MHz reference for the generation of its radio frequency f_S; this is then multiplied by a 12 factor and mixed with the beatnote coming from the BDU. The resulting signal is phase locked via an EOM in the first module.

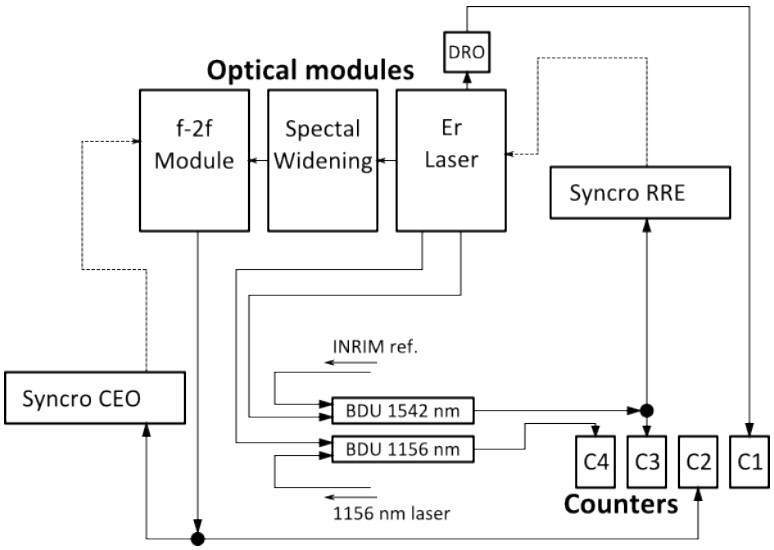

Figure 1.11: Block scheme of the setup for the lock and control of the repetition rate and offset frequency of the frequency comb. The BDU for the 1156 nm beatnote measurement is also represented.

There are also four counters dedicated to measure and monitor the various quantities. The first counts the beatnote signal of the repetition rate processed by the Dielectric Resonator Oscillator (DRO) unit. This extracts the fourth harmonic of f_{RR} and downmixes it with 980 MHz referred to the RF reference. The resulting $\approx$ 20 MHz are measured by the counter. Therefore

the repetition rate value is:

$$f_{RR} = \frac{980 \text{ MHz} + \text{C1}}{4} \tag{1.17}$$

where C1 is the lecture of the counter. The second and the third counters measure f_o and the optical reference beatnotes from the third optical modules and the BDU@1542 nm respectively. The last counter will be used, as we will see in chapter 2, to measure the beatnote signal of the 1156 nm laser present in the Ytterbium laboratory. For this purpose the frequency comb is equipped with an amplifier, a polarization maintaining optical fiber and a dedicated BDU shown in Fig. 1.10. The counters C3 and C4, dedicated to the optical beatnotes, are coupled with two band-pass filters in ranges 20-26 MHz and 50-65 MHz in order to achieve a better signal-to-noise ratio. Since the f_l beatnote of the laser to be measured with the frequency comb depends on f_{RR}, this means that the beatnote for the optical lock should be chosen appropriately in order to allow the counters to measure both the beatnote with the optical reference and that with f_l within their frequency ranges.

With a computer placed in the electronic rack it is possible to monitor and adjust every comb parameter, concerning both the laser mode locking and the f_{RR} and f_o lock. It also has a software provided by MENLO System to record the counters readings.

Chapter 2

578 nm laser stabilization

In the first part of chapter 1 we have discussed the importance of the presence of a doubly forbidden atomic clock transition for quantum simulation experiments with ultracold Ytterbium gases.

In this chapter in Sec. 2.1 I describe the 578 nm laser source present in the Ytterbium laboratory in Florence to excite this ultranarrow transition. In Sec. 2.2 I will discuss the problem concerning the laser stability, for which we have exploited the LIFT infrastructure and the techniques for the absolute frequency measurements discussed in the previous chapter. In Sec. 2.3 I will describe the long-term stabilization system implemented in this master thesis through the realization of a digital Proportional-Integral controller with a direct Digital Synthesizer (DDS). Finally, the results of this stabilization technique and a comparison with the previous conditions are shown in Sec. 2.4.

2.1 578 nm atomic clock laser: experimental setup

For the spectroscopy of the double-forbidden transition ${}^1S_0 \rightarrow {}^3P_0$ the experiment is equipped with a laser source, already present at the beginning of this Master thesis work, which is capable to excite the 578 nm transition with a linewidth of the order of 50 Hz. The experimental setup [26] [27] for this laser source is schematically presented in figure 2.1.

The External Cavity Diode Laser (ECDL) is composed by an InGaAs quantum-dot laser diode placed in a resonance optical cavity in Littrow configuration, emitting at a wavelength of λ=1156 nm. As well as the gain medium, the ECDL is composed by a diffraction grating at 45°; in this way the first order of grating diffraction is re-injected in the laser diode whereas

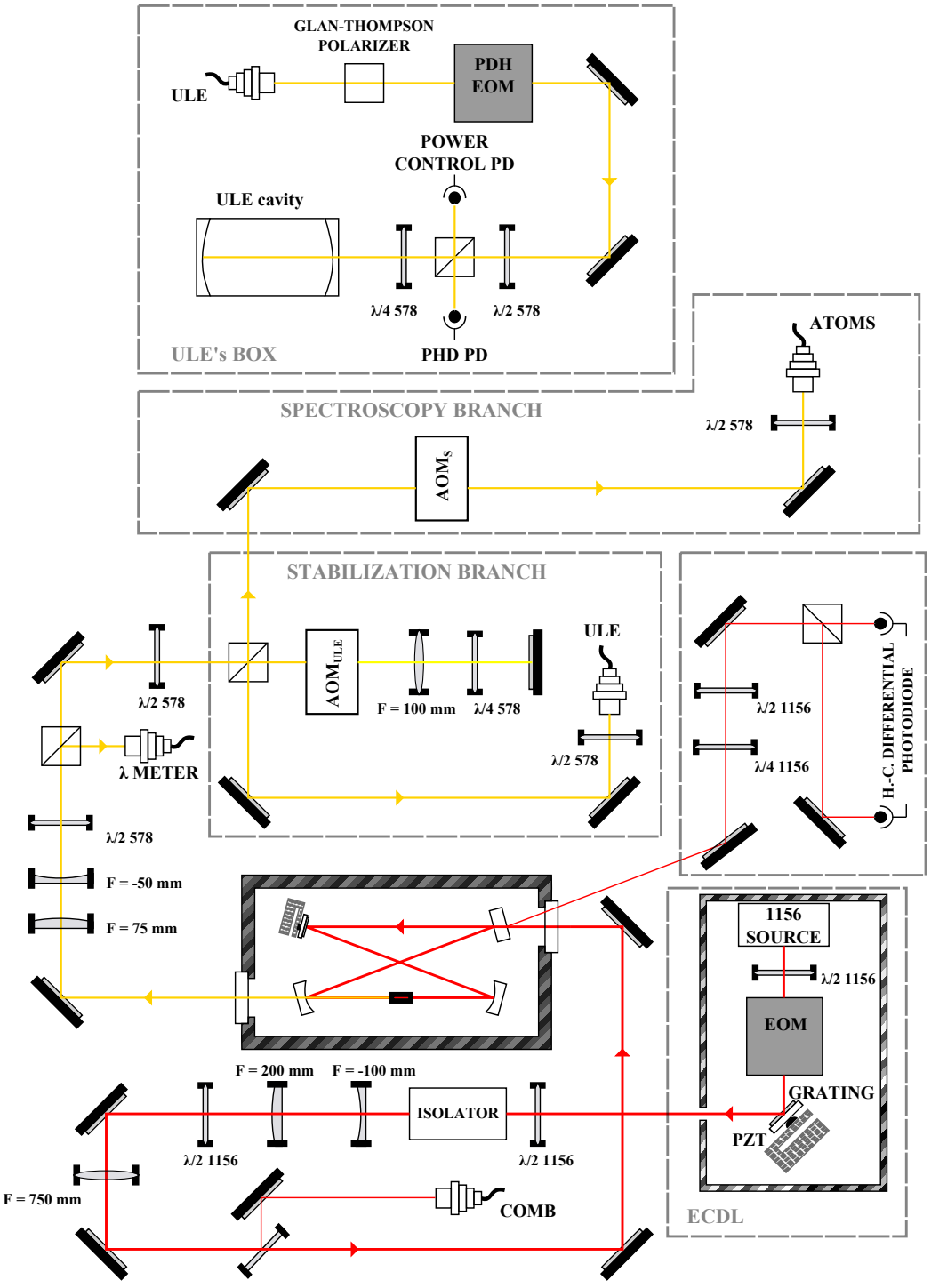

Figure 2.1: Scheme of 1156 nm and 578 nm laser sources.

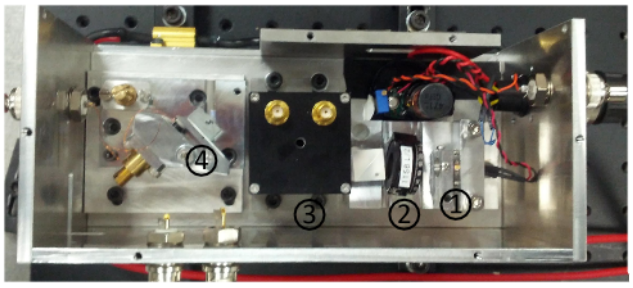

Figure 2.2: Picture of the ECDL: housing of the Quantum Dot (1), waveplate $\lambda/2$ for 1156 nm (2), EOM (3), grating and piezo actuator (4).

the order zero makes the output signal. Inside the optical cavity, there are two actuators used for changing the laser frequency: a piezoelectric actuator, placed on the grating mount, and an Electro-Optic Modulator (EOM), mounted between the laser diode and the grating. The system is illustrated in Fig. 2.2.

The ECDL output power is nearly 200 mW with a linewidth of the order of 20 kHz [28]. A beam sampler permits to pick a small fraction of the output which is sent, through an optical fiber, to a frequency comb, in order to measure the laser frequency stability. This measurement will be described in detail later in Sec. 2.2. The main part of the output is instead sent to a frequency-doubling cavity (Fig. 2.1) for the $\lambda = 578$ nm beam generation. The nonlinear medium for the second harmonic generation (SHG) is a $LiNbO_3$ crystal and the cavity, designed in a Symmetrical Bow-Tie configuration, is used to increase the conversion efficiency of the input infrared radiation into visible light. The crystal is periodically poled to ensure the quasi-phase matching condition in the SHG process. An Hansch-Couillaud locking system [29] is used to keep the cavity on resonance with the laser through a piezoelectric actuator mounted on a SHG cavity mirror.

The output radiation has a power of about 50 mW and then is divided by a polarizer beam splitter (PBS) in a stabilization branch and a spectroscopy branch. It is possible to vary the power in each branch through a $\lambda/2$ waveplate situated before the PBS. The beam in the first (stabilization) branch passes through an Acousto Optic Modulator (AOM), mounted in double passage at the order -1 and, through a polarization maintaining (PM) optical fiber, is delivered in a box containing a 10 cm long ultrastable Fabry-Pérot cavity. This cavity is completely built (spacer and mirrors) in Ultra Low Expansion (ULE) glass and is characterized by a very high finesse $\mathcal{F} \simeq 150000$ and a free spectral range $\Delta_{FSR} = c/2L$ of 1.5 GHz. The laser is locked to

the ULE cavity with a Pound-Drever-Hall (PDH) technique [30]: an EOM introduces two sidebands on the laser carrier frequency at ±7 MHz and a photodiode detects the light that is reflected back from the ULE input coupler, providing the error signal for the lock. As mentioned, the ULE cavity and the PDH optics are placed inside a box, which is a cube of 1 m side made of extruded polyester, in order to insulate thermally and acoustically the ULE cavity from the rest of the laboratory; in this regard more details will be given in the next section. A second photodiode is used to measure the incident power on the cavity which allows for its stabilization. In the second (spectroscopy) branch there is another AOM, used to control the frequency of the laser and the optical fiber that brings the laser beam to the table on which it will be directed on the Ytterbium atoms gas.

2.1.1 Transition frequency and lock system

As shown in Sec. 1.1, in order to observe the ${}^1S_0 \rightarrow {}^3P_0$ transition it is necessary that the laser linewidth is at most few tens of Hz on the experimental timescale (~ 1 s) and exceptionally stable on the long term, i.e. that the central frequency of the laser spectrum does not drift with respect to the atomic transition. In this section we report various methods used to "squeeze" and stabilize the laser and the evaluation of the limits reached before this thesis work.

From the scheme in Fig. 2.1 we obtain that the laser frequency f_l, as a function of the frequency f_{ULE} of the ULE mode used for the locking, will be:

$$2f_l = f_{ULE} + 2f_{AOM_{ULE}} \tag{2.1}$$

where we consider that the AOM_{ULE} is used at the order -1. The frequency outgoing from the spectroscopy branch is:

$$f_s = 2f_l + f_{AOM_s} \tag{2.2}$$

In order to excite the ${}^1S_0 \rightarrow {}^3P_0$ Ytterbium transition, this frequency must be equal to [31]:

$$f_s = 518.294576850 \text{ THz} \tag{2.3}$$

At the moment in which this thesis work was started, this value was known with an uncertainty of 4.4 kHz.

In order to chose the proper value of $f_{AOM_{ULE}}$, it was necessary to measure the ULE modes frequency. This was realized before this thesis work with the use of a frequency comb locked to a GPS reference [27]. The used method

is the one presented in section 2.2 and the frequency evaluation obtained in date 02/11/14 is:

$$f_{ULE} = 518.294325748 \text{ THz} \tag{2.4}$$

with a free spectral range, estimated at the kHz precision, equal to 1496.089 MHz. Therefore, it is evident that the reported f_{ULE} value is the frequency of the closest mode to the atomic transition.

In such a system, which uses the lock to a cavity mode for the stabilization of the laser frequency, the stability of the modes is one of the factors that contributes to the laser spectral width. It is in turn linked to the cavity length fluctuations due to a variation of both the refractive index of the cavity mirrors and the cavity geometrical length. These fluctuations affect the locking frequency, causing a phase noise which defines the laser linewidth. In our case, to achieve a linewidth of the order of 10 Hz, the cavity was accurately stabilized both thermally and mechanically. For the mechanical stabilization, the cavity design was realized in order to minimize the vibrational effects by placing the cavity on the Airy points; in fact these are defined as the reference points which minimize the distortion of the cavity [32]. Furthermore, the cavity and its support are placed inside a vacuum chamber which operates as an acoustic and thermal insulator and avoids air density fluctuations; these would change the air refractive index causing a variation of the optical path. The thermal stabilization is achieved setting the temperature of a copper shield, which encloses the cavity, through a resistive heater mounted externally to the vacuum chamber. The system is able to maintain the temperature fluctuations in a range of 3 mK. Finally, as we have already explained, the chamber is inside the polyester box; the air inside the box is in turn stabilized at 17.5 °C through a second feedback mechanism, based on Peltier cells, which maintains the temperature fluctuations in a range of 0.1 K. The temperature setpoint at which the cavity is stabilized must be chosen in order to minimize the glass coefficient of thermal expansion. For our ULE cavity this setpoint has been evaluated as 20.82 °C.

If we replace equations 2.1 in 2.2 and subtract Eq. 2.4 from Eq. 2.3, it is evident that in order to keep the laser in resonance with the atomic transition we have to impose:

$$2f_{AOM_{ULE}} + f_{AOM_s} = 251.102\text{MHz} \tag{2.5}$$

We have to consider, though, that the cavity glasses are fluids and therefore their molecules are subjected to a brownian motion. This leads to an aging drift which changes the frequency of the ULE cavity modes. Indeed the drift was observed during the measurements realized for the observation of coherent interorbital spin-exchange dynamics in a previous experiment [34]: after

at most 30 minutes the laser frequency was not in resonance with the atomic transition. A first analysis of the drift led to the approximate evaluation of 5 kHz/day. Despite this preliminary evaluation, a first attempt with a linear passive correction on the laser frequency made in order to compensate the drift did not show any significant improvement; this was a first proof of the fact that this drift has a non linear component and requests an active correction. The effect has been attributed to a finite stabilization of the ULE temperature, that is therefore characterized by an oscillation around the equilibrium point. This implies a laser frequency oscillation.

Since this effects, due to the nature of the cavity material itself, constitute a not-suppressible limit, recent researches have led to the development of single-crystal optical cavities [33], where both spacer and the mirror substrates are constructed from single-crystal silicon. In this way is possible to exceed the fundamental limit of ULE cavities given by the thermal noise due to cavity length fluctuations of an order of magnitude. However, the temperature where the silicon thermal expansion coefficient is zero and the mechanical loss is small is 124 K, hard to obtain, stabilize and isolate in a laboratory where the environmental work temperature is around 20°C.

2.2 Aging drift evaluation with a long-distance optical fiber link

It is evident that in order to perform measurements lasting more than few tens of minutes it is necessary to characterize the clock laser drift and to develop a correction system, which is the subject of this Master thesis. To achieve the first of these goals we compared our laser through a frequency comb with the absolute optical reference coming from INRIM in Turin.

As shown in section 2.1, between the ECDL and the frequency-doubling cavity a part of the "clock" laser beam is sampled and, through an optical fiber, arrives to the Beat Detection Unit (BDU) shown in Sec. 1.6 optimized for the wavelength 1156 nm, inside of which the beatnote with the frequency comb is made. To do this, an high power optical fiber for 1156 nm wavelength exits from the first frequency comb's module and is in turn inserted at the BDU input. Then the output of the BDU is directed to one of the four counters of the frequency comb's electronic rack. Recalling what we have discussed concerning the locking system of a frequency comb to an optical reference in section 1.4, we remark that the offset frequency ν_{offset} is stabilized with a PLL with a GPS reference and the repetition rate ν_{RR} is locked stabilizing the beatnote signal between the optical reference and its closest

tooth of the frequency comb. Moreover, the frequency comb parameters have been chosen in order to allow the measurement of the beatnote signals both with the absolute reference at 1542 nm and with the 1156 nm laser, namely signals both have to be in a frequency range measurable by the counters, as explained in Sec. 1.6. We report the found parameters and the considered absolute frequencies:

$$\begin{aligned}
&\textbf{1542 nm link frequency: } \nu_{Tu} = 194400155.6583695 \text{ MHz} \\
&\textbf{1156 nm frequency: } \nu_{1156} = 259147163 \pm 2 \text{ MHz} \\
&\textbf{Offset: } \nu_{offset} = +20 \text{ MHz} \\
&\textbf{Downmixed repetition rate: } \nu_{DRR} = 20.00376986 \text{ MHz} \\
&\textbf{Frequency comb DDS value: } 4.4 \text{ MHz}
\end{aligned} \tag{2.6}$$

With these settings we obtain:

$$\begin{aligned}
&\textbf{Beatnote with 1542 nm laser: } +52.8 \text{ MHz } (4.4 \text{ MHz x } 12) \\
&\textbf{Rep. Rate: } \nu_{RR} = \frac{980 \text{ MHz} + \nu_{DRR}}{4} \simeq 250.000942465 \text{ MHz} \\
&\textbf{Reference tooth: } N_{Tu} = \frac{\nu_{Tu} - \nu_{offset} - 52.8 \text{ MHz}}{\nu_{RR}} = 777597
\end{aligned} \tag{2.7}$$

That lead to the 1156 nm laser's values:

$$\begin{aligned}
&\textbf{Beatnote with 1156 nm laser: } +21.500 \text{ MHz} \\
&\textbf{Reference tooth: } N_{1156} = \left\lfloor \frac{\nu_{1156} - \nu_{offset} - 22.550 \text{ MHz}}{\nu_{RR}} + 0.5 \right\rfloor = 1036585
\end{aligned} \tag{2.8}$$

where $\lfloor x + 0.5 \rfloor$ symbol indicates the closest integer to x. The beatnote frequency reported above is a rough estimate (with $\sim$ 10 kHz accuracy) of the beatnote frequency with the 1156nm laser locked to the ULE cavity mode closer to the resonance frequency of the atomic transition $^1S_0 \rightarrow {}^3P_0$ of ^{173}Yb, shown in Eq. 2.4. At this point it was possible to record the beatnote frequencies measured by the counter on a text file using the software supplied by MENLO System. This will allow us to completely characterize the trend in time of the clock laser frequency.

2.2.1 Statistical tools

Any frequency reference, e.g. the one provided by an optical radiation stabilized to an atomic clock, is characterized by two properties: accuracy and stability:

- **Accuracy**: It is a systematic uncertainty. In the case of the spectroscopic measurement, it is the capability to reproduce the unperturbed atomic transition. The accuracy limit of the measurement can be estimated by the quantitative knowledge of the various physical effects which shift the atomic transition (e.g. presence of magnetic fields or ultracold atoms collisions, temperature via the blackbody radiation). These effects, in correction to the $^1S_0 \rightarrow ^3P_0$ absolute frequency measurement, will be discussed in Ch. 3.

- **Stability**: It is the attitude of a measure to maintain a time constant value and therefore it is a kind of statistical uncertainty. The measured variations of a physical observable may be discontinuous and with a random amplitude, or continuous and monodirectional (the latters called drifts); their possible causes are: environmental perturbations, instruments quality or effectives observable variations. In an atomic clock the statistical tool that quantifies the system stability is the Allan deviation and it is able to distinguish between the various typical noise sources which concern an oscillator.

Defining y the relative frequency variation of an oscillator frequency $\nu(t)$:

$$y = \frac{\delta\nu}{\nu} = \frac{1}{2\pi\nu}\frac{d\delta\phi}{dt} \tag{2.9}$$

with $\delta\phi$ the phase variations, the Allan deviation is obtained starting from the N-sample variance of the frequency fluctuations, defined as [23, 35]:

$$\sigma^2(N, t_a) = \left\langle \frac{1}{N-1}\left\{\sum_{n=1}^{N}\left[\bar{y}(t_n)\right]^2 - \frac{1}{N}\left[\sum_{m=0}^{N}\bar{y}(t_m)\right]^2\right\}\right\rangle \tag{2.10}$$

where N is the number of frequency samples, t_a the time interval on which we average, $\bar{y}(t_k)$ the average frequency related to an arbitrary time t_k:

$$\bar{y}(t_k) = \frac{1}{t_a}\int_{t_k - t_a}^{t_k} y(t)dt \tag{2.11}$$

In particular, Eq. 2.10 is valid in the hypothesis that there is not dead time between each frequency sample and each frequency estimate. Particularly useful is the 2-sample variance, also named *Allan variance*, given by:

$$\sigma_y^2(t_a) = \frac{1}{2}\langle(\bar{y}(t_k) - \bar{y}(t_{k+1}))^2\rangle \tag{2.12}$$

that is equal to:

$$\sigma_y^2(t_a) = \frac{1}{2(M-1)} \sum_{i=1}^{M-1} \left[\bar{y}_{i+1}(t_a) - \bar{y}_i(t_a)\right]^2 \tag{2.13}$$

where $\bar{y}_i$ is the i-th of M frequency values averaged over the measurement interval t_a. This is called *non-overlapping* Allan variance; if the original data were taken with the $\bar{y}$'s spaced by τ, we could pick t_a to be any integer multiple of τ [36] and the the resulting *overlapped* Allan variance would be:

$$\sigma_y^2(n\tau, M) = \frac{1}{2n^2(M-2n+1)} \sum_{j=0}^{M-2n} \left(\sum_{i=j}^{j+n-1} \bar{y}_{i+n} - \bar{y}_i \right)^2 \tag{2.14}$$

The Allan deviation (ADEV) is defined as the square root of the Allan variance.

Another tool, very useful to investigate the noise in an oscillator, is the noise Power Spectral Density (PSD) $S_y(f)$, defined as the Fourier transform of the autocorrelation function $R(\tau)$ of $y(t)$:

$$R(\tau) = \int_{-\infty}^{+\infty} y(t+\tau)y(t)dt \tag{2.15}$$

$$S_y(f) = \int_{-\infty}^{+\infty} R(\tau)e^{-i2\pi f\tau}d\tau \tag{2.16}$$

Thanks to these statistical tools we have done the drift analysis.

2.2.2 Drift analysis

For the drift characterization, some beatnote measurements have been acquired for the duration of the order of a day in order to highlight the mid-long term trend of the drift. They have been recorded with the fourth counter of the frequency comb by its computer. We note that the gate time of the counter for every measurement performed is set to 1 s. In Fig. 2.3 we report in blue and black the plots of the beatnote frequency values for two measurements on two consecutive days. The empty regions inside the single acquisition are due to the exclusion of the data acquired when one of the components of the measurement chain (INRIM reference, 1156 nm laser or frequency comb) was not properly locked. We note the presence of both linear and non linear trends.

Recalling what we discussed at the end of Sec. 2.1.1, in order to try to fit these data we have chosen a test function $y(t)$ with two contributions: one

that would correspond to the aging drift of the ULE cavity glasses, a linear term, the other to the temperature oscillations of the ULE cavity, for which we have picked a sinusoidal term:

$$y(t) = q + at + b\sin(\omega t + \phi) \tag{2.17}$$

The relative results for the two datasets are displayed through the red and green lines in the graph and with the tables 2.1 and 2.2.

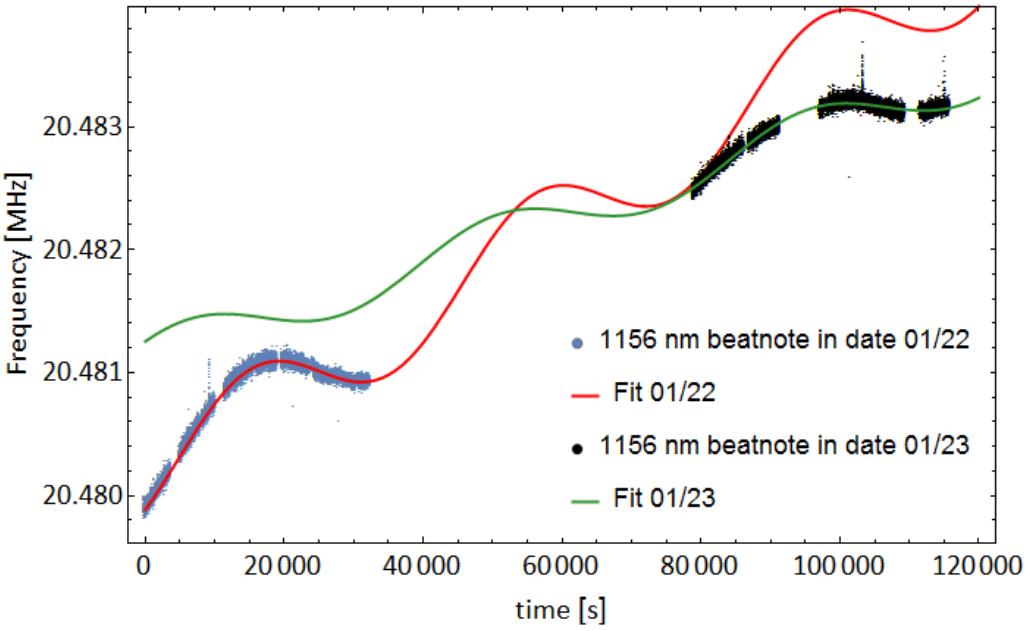

Figure 2.3: Comparison of the drift trend in two consecutive days. The graph shows the frequency values of the beatnote between the 1156 nm laser (blue and black plots) and the fits with a test function as presented in Eq. 2.17 (red and green lines).

Table 2.1: Fit parameters for the day 01/22/2015.

	Estimate	Standard error	Confidence interval
q	20.4801292 MHz	1.9x10^{-6} MHz	[20.4801255 ,20.4801330] MHz
a	3.4898x10^{-2} Hz/s	6.6x10^{-5} Hz/s	[3.4768x10^{-2} , 3.5028x10^{-2}] Hz/s
b	369.9 Hz/s	1.0 Hz/s	[368.0 , 371.9] Hz/s
ω	1.5343x10^{-4} rad/s	3.6*10^{-7} rad/s	[1.5273x10^{-4} , 1.5413x10^{-4}] rad/s
ϕ	-0.7221 rad	6.7*10^{-3} rad	[-0.7352, -0.7090] rad

Table 2.2: Fit parameters for the day 01/23/2015.

	Estimate	Standard error	Confidence interval
q	20.4826322 MHz	2.1x10^{-6} MHz	[20.4826282 , 20.4826362] MHz
a	1.9133x10^{-2} Hz/s	6.5x10^{-5} Hz/s	[1.9006x10^{-2} , 1.9259x10^{-2}] Hz/s
b	192.90 Hz/s	0.92 Hz/s	[191.08 , 194.71] Hz/s
ω	1.4040x10^{-4} rad/s	6.3*10^{-7} rad/s	[1.3916x10^{-4} , 1.4163x10^{-4}] rad/s
ϕ	-0.729 rad	1.3*10^{-2} rad	[-0.756, -0.703] rad

We note immediately from both the graph and the tables that the two fits are not consistent each other. Evidently this drift, that has no deep physical meaning, is not corresponding to our model and depends from the specific environmental conditions in which the experimental setup is. This underlines the fact that a simple passive correction is not able to remove this phenomenon. Therefore the system that we will see in Sec. 2.3 implemented in this thesis work consists in a feed-back system.

Now we report in Fig. 2.4 and 2.5 the respective behaviors of the overlapped Allan deviation and of the frequency noise PSD; from now on the uncertain on the ADEV values is estimated by the simple subtraction between the maximum and the minimum values returned by the analysis program for each point.

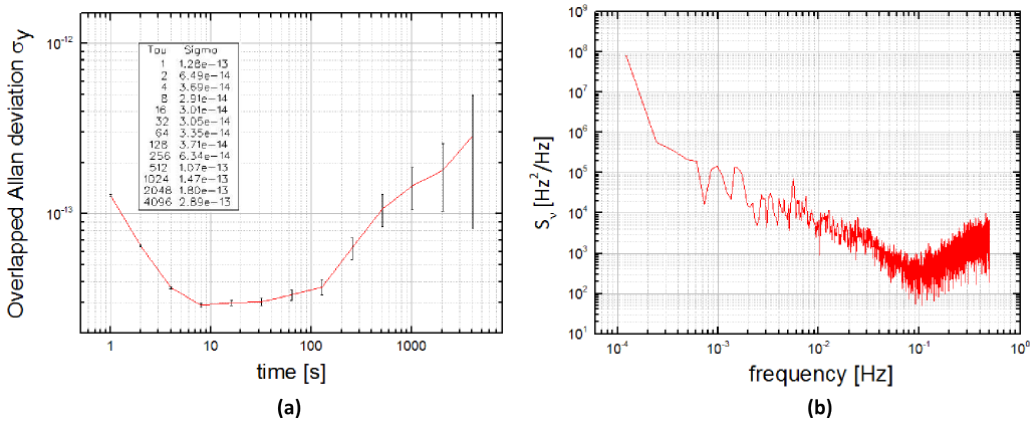

Figure 2.4: Analysis of the 01/22/2015 data. **(a)** Overlapped Allan deviation. **(b)** Power spectral density expressed as $S_\nu = \nu_0^2 S_y$, with ν_0^2 frequency of the 1156 nm laser approximated to GHz.

We observe an ADEV at 1 second of about 1.5*10^{-13}, which decreases initially with a trend of $\simeq t^{-1}$, which corresponds to a phase modulation noise [35]; then it smooths, achieves a minimum value between $3 \cdot 10^{-14}$ and

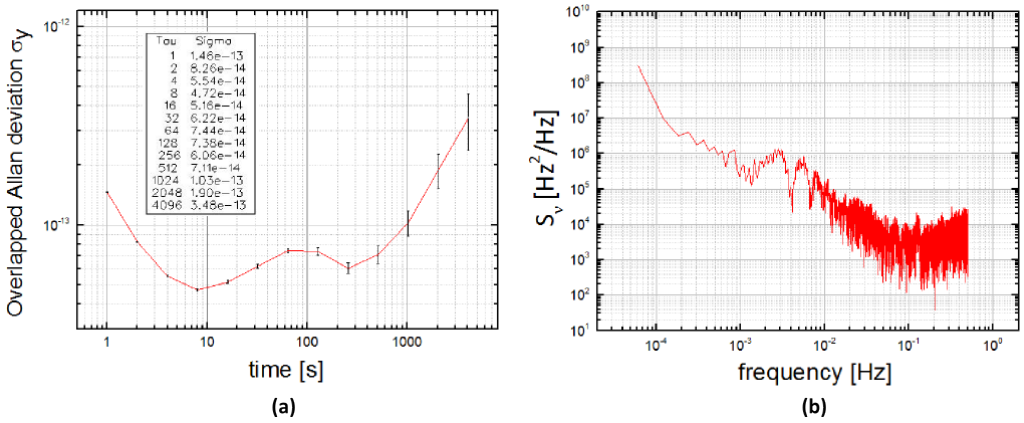

Figure 2.5: Analysis of the 01/23/2015 data. **(a)** Overlapped Allan deviation. **(b)** Power spectral density expressed as $S_\nu = \nu_0^2 S_y$, with ν_0^2 frequency of the 1156 nm laser approximated to GHz.

$4 \cdot 10^{-14}$ for time values of 8-15 s and later increases with time. In particular we note a bump followed by a linear (in logarithm scale) trend; a bump denotes an oscillating noise term, with period and amplitude indicated by the peak, whereas the linear trend indicates a drift. The oscillating terms of the two days are different: the 01/22 term has a period and an amplitude of about 1000 s and 1.8*10^{-13} respectively and the 01/23 term has about a 100 s period and 7.5*10^{-14} amplitude. Concerning the PSDs, they reflect the Allan deviation behavior with a noise which decreases for short times until $\simeq$0.1 Hz and then increases again.

We can conclude that the laser has a linear drift which arises roughly at time included between 10 s and 25 s; on this are superimposed various oscillating noise components, one at very long time period, about 15h, and two other at midterm, about 1000 s and 100 s. The long term oscillation could be caused by a residual temperature oscillation of the ULE cavity, the amplitude of which, however, would change depending on the specific experimental conditions of the environment; instead the other two were due to a INRIM reference instability. In fact, if the 1542 nm signal coming from Turin and locked to the Hg maser has a residual oscillation, this affects the repetition rate of the frequency comb. Consequently we observe an oscillation of the beatnote between the 1156 nm and the frequency comb. Moreover, since the frequency of the 1156 nm laser ($\sim$ 259 THz) is greater than the INRIM reference ($\sim$ 195 THz) at which is locked the repetition rate, from equation 1.16 we observe that a small oscillation hardly to observe on the 1542 nm laser would have an amplified effect (equal to the ratio between the 1156 nm and 1542 nm lasers frequencies) on our laser. To verify this

hypothesis we did a simple test, performing a control measure between our laser and the 1542 nm laser: we make the difference Δ(beatnotes) between the beatnote of 1156 nm with Florence frequency comb (and so with the 1542 nm) and beatnote of 1542 nm with the maser; in this way we subtract the noise due to the INRIM lock system and Δ(beatnotes) represents the behavior that the 1156 nm laser would have if locked to the maser; the simple relationship is:

$$\Delta(\text{beatnotes}) = f_{beat_{1156}} - f_{beat_{1542}} * \frac{259}{195} \tag{2.18}$$

where $f_{beat_{1156}}$ is the beatnote between our laser and the closest tooth of the frequency comb in Florence locked to the 1542 nm reference, $f_{beat_{1542}}$ the beatnote between the 1542 nm laser and the frequency comb in Turin locked to the maser and 259/195 is the ratio between respectively 1156 nm and 1542 nm laser frequencies approximated at the order of THz. In this

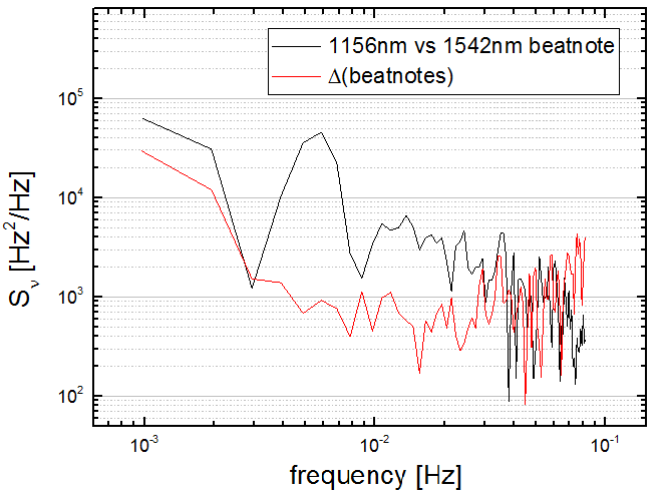

Figure 2.6: Comparison between the power spectral densities of the beatnotes between 1156 nm laser and Florence frequency comb (black line) and Δ(beatnotes) (red line).

way comparing the PSD without and with the subtraction in Eq. 2.18, see respectively the black and the red lines in Fig. 2.6, we can observe that the typical noise peak at $6 * 10^{-3}$ Hz present in the single beatnote (which corresponds to an oscillation with a period of $\sim$ 150 s and therefore to the midterm oscillation) completely disappears if we remove the noise due to the INRIM lock system to the maser. After an upgrade of the link system of the 1542 nm to the maser reference this issue has been solved.

Another noise source is the uncertainty on the count system of the comb's counters. In fact the uncertainty on every count value acquired in 1 s of gate time is principally due to a phase uncertainty, because only two phase measurements are used, essentially detecting the times of the signal's zero-crossings at the beginning and at the end of the measurement interval, making this technique, called Π-averaging, very susceptible to wide-bandwidth phase noise [37]. However, renouncing the possibility of use of the analysis software of the frequency comb computer, there is the possibility to set the counters in order to average the phase over parts of the interval and in this way effectively reduce the bandwidth, and thus the influence, of phase noise; in this second mode, called Λ-averaging, for a data over a time interval τ the phase is averaged between times $0 < t < \tau/2$ and $\tau/2 < t < \tau$.

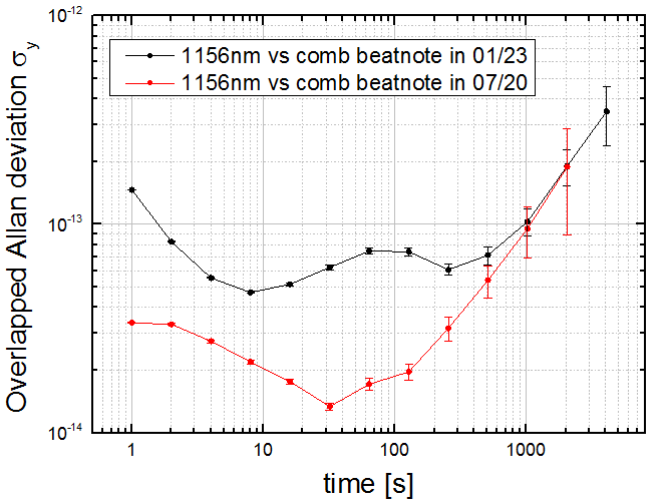

Figure 2.7: Comparison between the Allan deviations with the old INRIM lock to maser and the frequency comb counter in Florence in Π-averaging (black plot) and with the new INRIM lock and the frequency comb counter in Λ-averaging (red plot).

With this changing the measurement of the stability is improved at short times of about an order of magnitude, as shown in Fig. 2.7, and the curve has a different slope, of $\sim t^{-1/3}$, therefore corresponding to another source: a frequency noise modulation; on the other hand, at long time the Allan deviation, that is affected by the drift, has the same values than before. In Fig. 2.8 and 2.9 we report also the trend of the 1156 nm laser frequency and the respective PSD.

At this point the characterization of the ULE drift is concluded and the last conditions illustrated in Fig. 2.9 are the starting point for its correction.

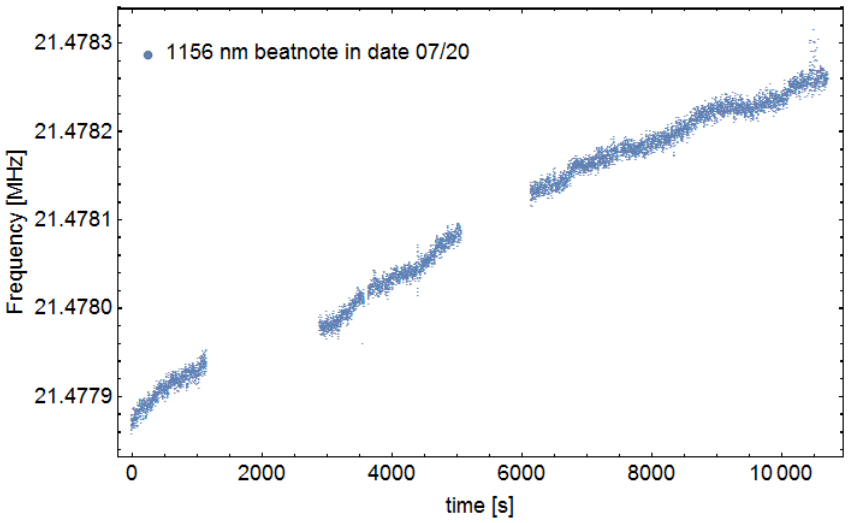

Figure 2.8: ULE drift trend with Λ-averaging counter in date 07/20/2015.

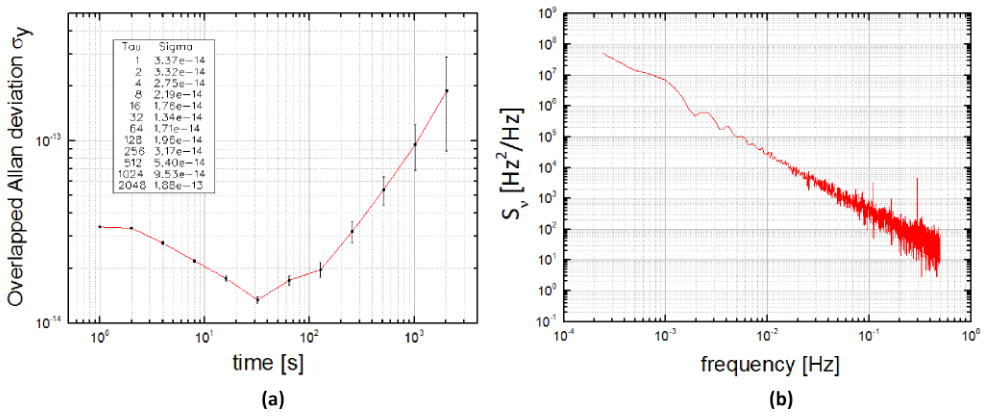

Figure 2.9: Overlapped Allan deviation for the dataset in figure 2.8.

We remark that the long term oscillation (even if it is not evident in Fig. 2.8 due to the insufficient time acquisition) is still present; it involves that it will not be sufficient to implement a simple linear and passive correction but that a feed-back system will be necessary in order to remove properly the drift in every part of the day.

2.3 Long term correction system

In this section we show the experimental strategy performed in this master thesis work to eliminate the slow drift of the ULE cavity and stabilize the

frequency of the 578 nm clock laser. For this purpose we use the absolute frequency reference given by the optical link and we actively compensate the ULE cavity drift changing automatically the frequency of the ULE's AOM lock (see Sec. 2.1) in order to stabilize the beatnote between the laser and the frequency comb locked to the LIFT link, that is chosen as setpoint frequency $f_{setpoint}$ for the correction system. In figure 2.10 we can see a block scheme of the correction setup. The correction is actuated through a Direct Digital Synthesizer (DDS).

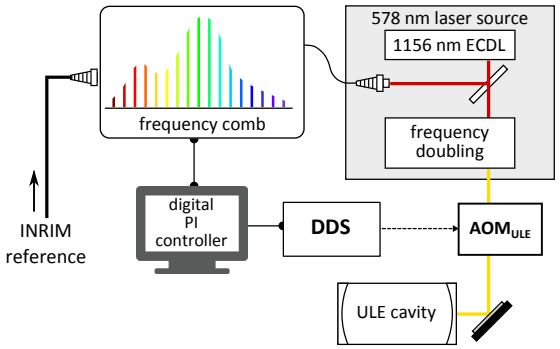

Figure 2.10: Block diagram of the dedrift system setup.

2.3.1 Analysis and correction

First of all, we note that the benchmark value $f_{setpoint}$ for the correction system corresponds to f_b in Eq. 1.12, that can be rewrite as:

$$f_l = nf_{RR} + f_o + f_{setpoint} \tag{2.19}$$

where n is the closest tooth of the frequency comb to the 1156 nm laser. Since f_{RR} and f_o are respectively locked to the 1542 nm and GPS reference, once stabilized $f_{setpoint}$, the value f_l will be fixed. To implement the stabilization system the benchmark for our correction $f_{setpoint}$ is arbitrary, but in Ch. 3 we will see that for our experimental purpose it will be determined in Sec. 3.4 in order to maintain the laser frequency in resonance with the atomic transition.

Chosen an $f_{setpoint}$, the associated error ϵ will be given by the gap from this frequency, represented by the difference between the $f_{setpoint}$ and the measured beatnote signal; since our correction must be effective on the long-term trend, for an ϵ evaluation we will not consider a single beatnote count measurement, acquired by the frequency comb counter on 1 s interval, but

its average on the correction timescale, represented by the one at which the laser drift arises: 10-25 s. So we can write:

$$\epsilon_i = \pm(f_{setpoint} - f_{average_i}) \tag{2.20}$$

where ϵ_i is the error relative to the i-th time interval and $f_{average_i}$ is:

$$f_{average_i} = \frac{\sum_{n=1}^{N} f_n}{N} \tag{2.21}$$

with f_n a single beatnote measurement value and N the number of the measurements for the average.

Concerning the correction sign in Eq. 2.20, it depends on the beatnote sign; with reference to section 2.1.1, this ensues from Eq. 2.1 in absence of correction:

$$\begin{cases} f_{ULE} = 2f_l - 2f_{AOM_{ULE}} \\ f'_{ULE} = 2f'_l - 2f_{AOM_{ULE}} \end{cases} \tag{2.22}$$

f_i are the frequency values at time t and f'_i indicate the value of the same quantity at a time $t' > t$. Therefore without any correction it would be:

$$\Delta(f_{ULE}) = f'_{ULE} - f_{ULE} = 2f'_l - 2f_l = 2\Delta(f_l) \tag{2.23}$$

On the other hand, our correction will operate on the ULE's AOM, changing its frequency in order to maintain f_l constant, obtaining:

$$f'_{ULE} = 2f_l - 2f'_{AOM_{ULE}} \tag{2.24}$$

From Eqs. 2.22 and 2.24 we find:

$$\begin{aligned} \Delta(f_{ULE}) &= -2f'_{AOM_{ULE}} + 2f_{AOM_{ULE}} \\ \Rightarrow \Delta(f_{AOM_{ULE}}) &= -\frac{\Delta(f_{ULE})}{2} \end{aligned} \tag{2.25}$$

Therefore comparing Eqs. 2.23 and 2.25 we achieve:

$$\Delta(f_{AOM_{ULE}}) = -\Delta(f_l) \tag{2.26}$$

So if we consider a positive drift we must apply a correction that decreases the ULE's AOM frequency and vice versa. Otherwise, maintaining a positive drift example, the beatnote will seem to increase or decrease depending on the laser frequency being respectively greater or smaller than the frequency of the comb closer tooth. We can resume all conditions schematically as:

$$\begin{cases} \Delta(f_{ULE}) > 0 \Rightarrow \begin{cases} f_l > f_{comb} \Rightarrow \epsilon_i = +(f_{setpoint} - f_{average_i}) \\ f_l < f_{comb} \Rightarrow \epsilon_i = -(f_{setpoint} - f_{average_i}) \end{cases} \\ \Delta(f_{ULE}) < 0 \Rightarrow \begin{cases} f_l > f_{comb} \Rightarrow \epsilon_i = +(f_{setpoint} - f_{average_i}) \\ f_l < f_{comb} \Rightarrow \epsilon_i = -(f_{setpoint} - f_{average_i}) \end{cases} \end{cases} \tag{2.27}$$

For every analysis cycle, that occurs after a number of seconds equal to N, we run a ULE's AOM frequency correction such as:

$$f_{AOM_i} = f_{AOM_{offset}} + K_P \epsilon_i + K_I \sum_{j=1}^{i} \epsilon_j \tag{2.28}$$

where to simplify the notation the ULE subscript is implied and $f_{AOM_{offset}}$ and f_{AOM_i} are respectively the start frequency and the one set by an actuator on the AOM_{ULE} at the i-th correction, and K_P and K_I are defined as the proportional and integral correction gains respectively. We chose an algorithm such as the one in Eq. 2.28 because a Proportional-Integral controller is necessary to achieve a stationary stabilization to the setpoint.

2.3.2 Actuation system: Direct Digital Synthesizer

To actuate the correction on the AOM we used a Direct Digital Synthesizer (DDS). This device is based on direct digital synthesis, that is a method for a periodic waveform generation using digital electronics starting from a reference oscillator. The advantage of this system is that the only generated error on the waveform is due to the reference oscillator. For further details concerning operation of a DDS refer to [38].

The DDS model used in this thesis is the AD9910 produced by ANALOG DEVICES [39]. This is in turn already integrated on the UG-207 Evaluation Board. The main features provided by the manufacturer are:

- 1 Giga-sample per second (GSPS) internal clock speed, 14-bit DAC
- 32-bit accumulator, up to 400 MHz analog output
- Frequency resolution: 0.23 Hz (see **??**)
- Phase locked loop (PLL) reference clock multiplier

Furthermore, the relative phase and amplitude can be digitally controlled by means of a 16-bit phase offset word (POW) and a 14-bit amplitude scale factor (ASF).

In particular, the PLL enables to use a reference clock frequency much lower than the system clock frequency. The PLL output frequency range is given by the internal voltage controlled oscillator (VCO). In addition, the user can program the VCO to one of six operating ranges, shown in Fig. 2.11. The UG-207 Evaluation Board on which the DDS is mounted is provided with an USB interface and a serial port (mutually exclusive) that provide access to the memory of the AD-9910 and can be used to program it.

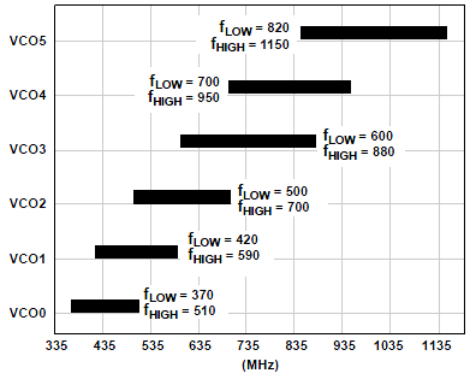

Figure 2.11: VCO ranges of the DDS AD-9910.

In order to actuate the drift correction it has been inserted in the experimental setup as ULE's AOM driver and connected to the frequency comb computer by USB port. So the correction chain, shown also in Fig. 2.10, consists in the comb counter that measure the laser drift, the comb's computer where the counter acquisitions are stored and analyzed to evaluate the f_{AOM_i} values and the DDS through the correction is actuated. To realize the setup, during this thesis also the DDS power supply system has been prepared and its picture is shown in Fig. 2.12.

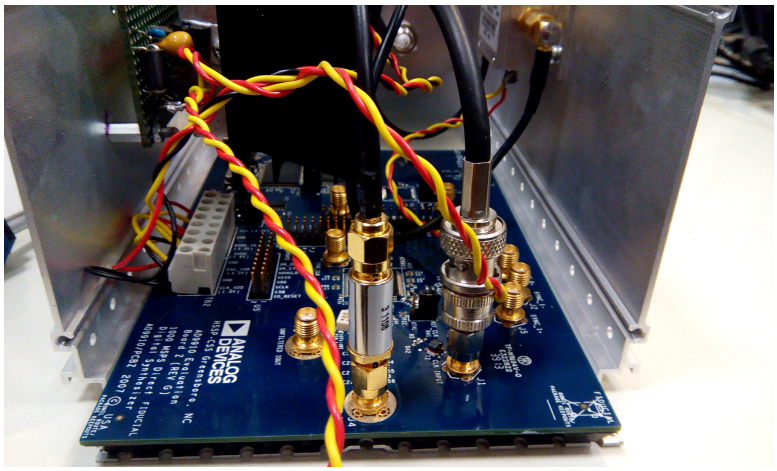

Figure 2.12: Picture of the DDS setup. We can see in the bottom the UG-207 evaluation board and in the high left corner the power supply system with a dissipator mounted to prevent overheating.

We then move on to consider how the correction system presented in subsection 2.3.1 has been implemented. Starting by the DDS software source code supplied by ANALOG DEVICES, I modified the program in order to

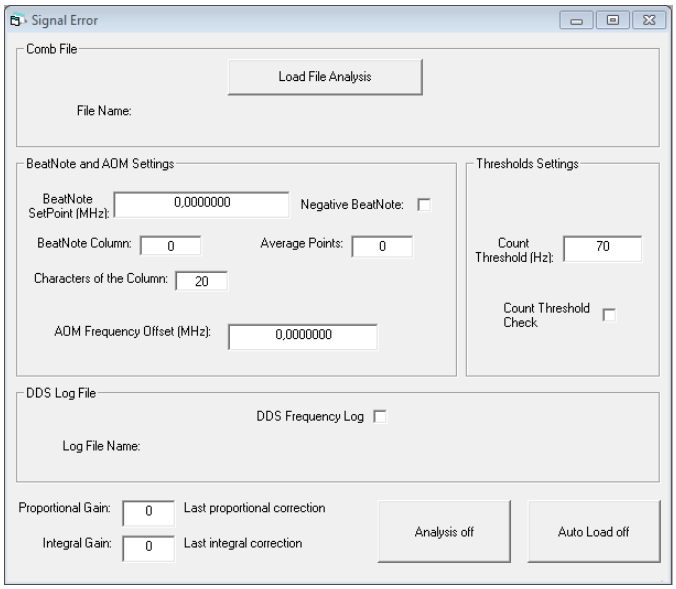

Figure 2.13: User interface of the dedrift system programmed into the UG-207 ANALOG DEVICE software.

open and read the file where the frequency comb software stores the beatnote counter readings during the acquisition. The beatnote setpoint, the number of readings on which the average is calculated, the starting AOM frequency offset and the proportional and integral gains must be set before starting the correction. In Fig. 2.13 a screenshot of the programmed user interface is reported. The code with which is I write the software is Visual Basic. Beyond the analysis algorithm it contains the possibility to set a threshold of the difference between the single 1 s count and the $f_{setpoint}$ over which the data is rejected and does not contribute to the average. It is also possible to choose the sign of the beatnote in order to discern the sign in Eq. 2.20. Clicking on the "Analysis" check-box in the bottom, the correction routine starts and operates like the algorithm in Eq. 2.28, with an internal timer that cyclically activates the error calculation after a number of seconds equal to the number in the "Average points" text-box. Moreover, the user can create a file wherein all the DDS output frequency values are stored in order to check the dedrift algorithm behavior and, indirectly, the laser drift.

We stress that what has been done corresponds to a digital Proportional-Integral (PI) controller, where proportional and integral gains are decided by user.

2.4 Dedrift data analysis

With this correction system several dedrift tests have been done with various setpoints, number of average points and gain values in order to find the best settings configuration. First of all, for the time scale of the correction we selected an interval near the minimum of the Allan deviation for the beatnote of the laser with the frequency comb: 12-20 s (see Fig. 2.4 and 2.5); in fact that corresponds to the time above which the ULE drift starts to dominate the laser instability. Regarding the setpoint value, during the two principal periods of measurements (approximately March and July), we chose two different values that permitted to maintain the 578 nm laser near the atomic resonance and, therefore, to perform both the dedrift system analysis and spectroscopy measurements: $f_{setpoint} = 22.5315697$ MHz or 21.4772180 MHz. The difference between them is due to a changing of the 1542 nm reference coming from INRIM and the explanation of their experimental values will be discussed in Sec. 3.4. The proportional and integral gains were changed searching the configuration that minimizes the Allan deviation for a long-term correction, without inducing frequency auto-oscillations due to the corrections. We report the analysis of some typical measurements.

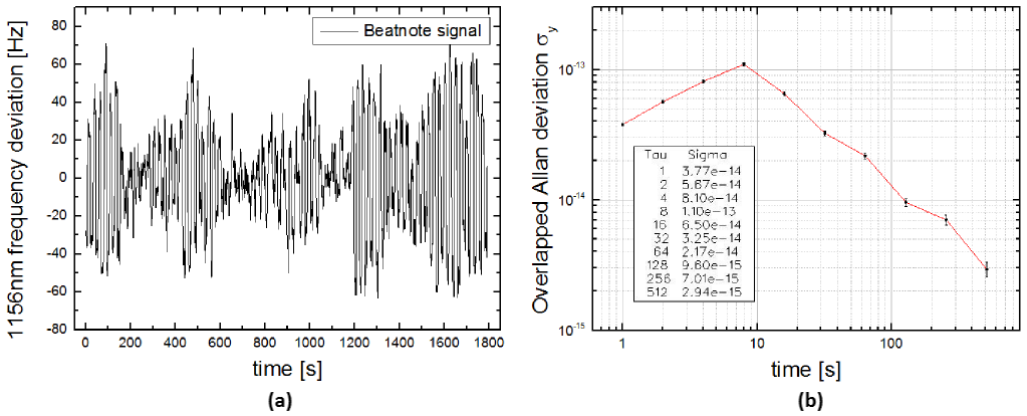

Figure 2.14: Dedrift measurement data with $K_P = 0.66$, $K_I = 0.66$ and $t_{average} = 12s$. **(a)** 1156 nm vs comb beatnote trend after removing the beatnote setpoint offset; it is evident an high frequency oscillation with period of about $t_{average}$ and an envelope of hundreds of seconds. **(b)** Overlapped Allan deviation.

In particular, before we illustrate the effect of different gains constants with tha same correction time scale. The graphs in Fig. 2.14 and 2.15 refer to the same acquisition time $f_{average} = 12$ s and gain constants $K_P = 0.66$ and $K_I = 0.66$ (Fig. 2.14), $K_P = 0.50$ and $K_I = 0.050$ (Fig. 2.15(a)) and $K_P = 0.20$ and $K_I = 0.15$ (Fig. 2.15(b)). In the first case in Fig. 2.14

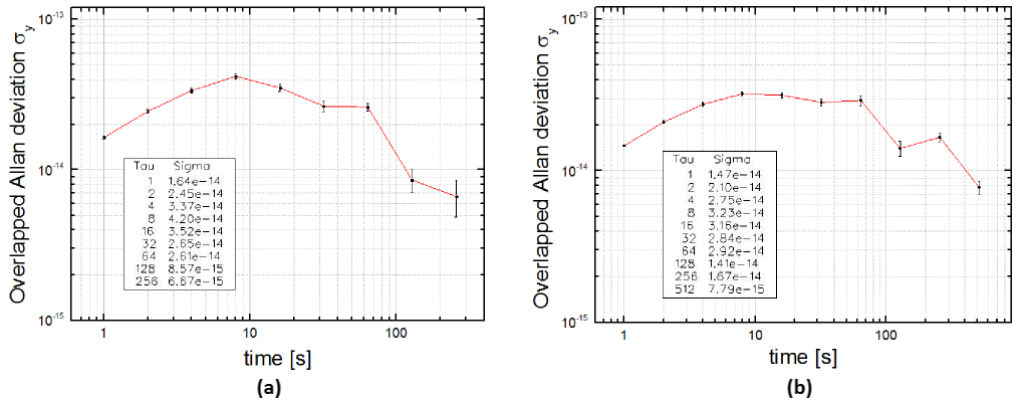

Figure 2.15: (a) Overlapped Allan deviation of a dedrift measurement data with $K_P = 0.50$, $K_I = 0.50$ and $t_{average} = 12s$. (b) Overlapped Allan deviation of a dedrift measurement data with $K_P = 0.20$, $K_I = 0.15$ and $t_{average} = 12s$.

we can see the gains limit at which a laser frequency auto-oscillation arises: here it is evident also in the frequency trend and it is therefore reported. Fig. 2.15(a) exhibits a similar behavior since the gain values are still too high. Fig. 2.15(b) shows a measurement with low gains and represents instead a case for which the correction does no have effect for times lower than roughly 300 s: it is the signal that the gain values are too small. Also for this case we can observe an increase of the instability for a time of the order of the correction timescale, even if smaller than the previous cases; the cause was that the correction being too fast, intervening when the drift had not yet emerged and so introducing another noise.

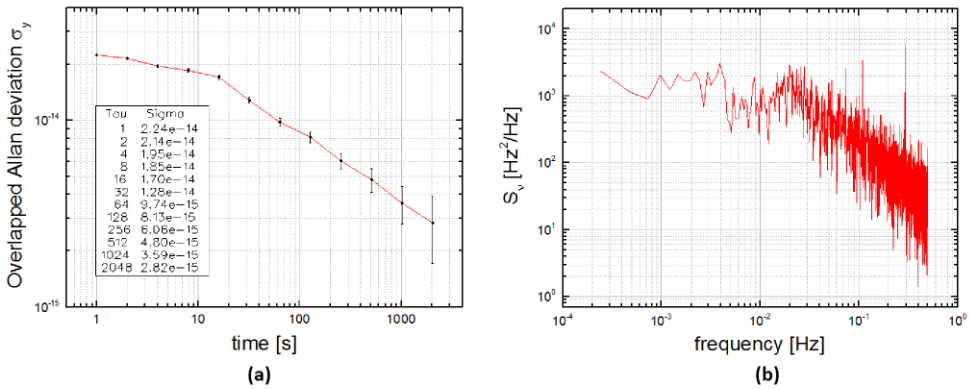

Figure 2.16: Analysis of a dedrift measurement data with $K_P = 0.30$, $K_I = 0.20$ and $t_{average} = 20s$. **(a)** Overlapped Allan deviation. **(b)** Power spectral density.

Therefore we changed $t_{average}$ to the value of 20 s and performed mea-

surements with intermediate gain values, obtaining the results shown in Fig. 2.16 for $K_P = 0.30$ and $K_I = 0.20$, where two different regions are evident. Considering Fig. 2.16(a), the first region is under the time of analysis, where the overlapped Allan deviation has a trend $\sim t^{-1/10}$, and the second that starts at $\simeq 20$ s where σ_y goes $\sim t^{-2/5}$. In both cases the noise source should be a frequency modulation, but while for $t < 20$ s the leading term is the flicker noise (characterized by a $\sigma_y^2 \propto t^0$), in the other one it is the white noise (with $\sigma_y^2 \propto t^{-1}$). From the fact that the slope of the Allan deviation for long times does not change, we can conclude that the limit of our correction system is not yet reached. The 578 nm laser stability, equal to that of the 1156 nm laser, at $t \sim 2000$ s is $\simeq 2.8 * 10^{-15}$, corresponding to an absolute frequency fluctuation of the order of:

$$\Delta(\nu) = 518.294 \text{ THz} * 2.8 * 10^{-15} \simeq 1.5 \text{ Hz} \tag{2.29}$$

With reference to [40], the relative PSD, showed in Fig. 2.16(b), reflects the behavior of the ADEV with a trend $\propto f^{-1}$, where f is the spectral frequency, for big f (short t), like a flicker frequency modulation noise, and a trend independent from f for the region where there should be the white frequency modulation.

In conclusion, I have developed a stabilization system for the 578 nm laser with the employment of a long distance optical fiber link programming a digital PI which uses a Direct Digital Synthesizer as correction actuator, obtaining an improvement of the laser stability of about two order of magnitude. In summary the figures 2.17 and 2.18 report a comparison of the ADEV and the PSD before and after the work.

In the next chapter we will show the results related to an experiment realized with ultracold ^{173}Yb gases in which this experimental system for the 578 nm laser stabilization has been crucial in order to perform the measurements, that required long measurement times, of the order of few hours.

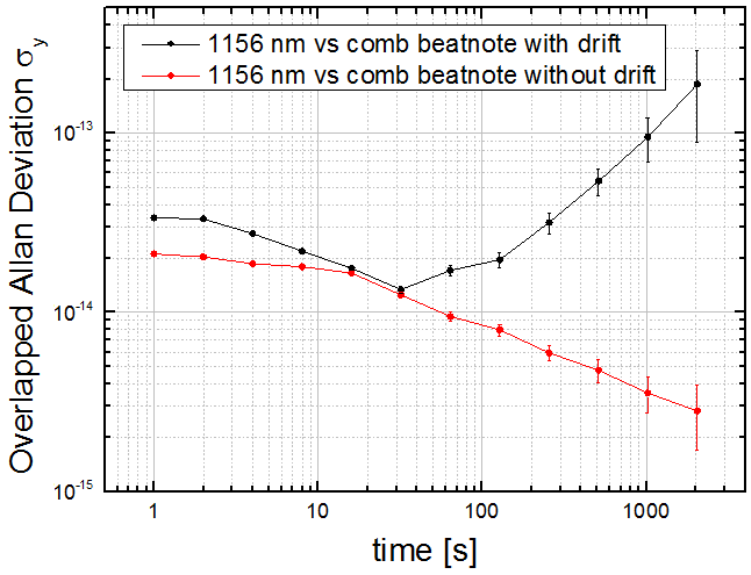

Figure 2.17: Comparison of the overlapped Allan deviations without (black dataset) and with (red dataset) the correction system implemented. Already for times lower than an hour the stability of the clock laser is implemented of two order of magnitude.

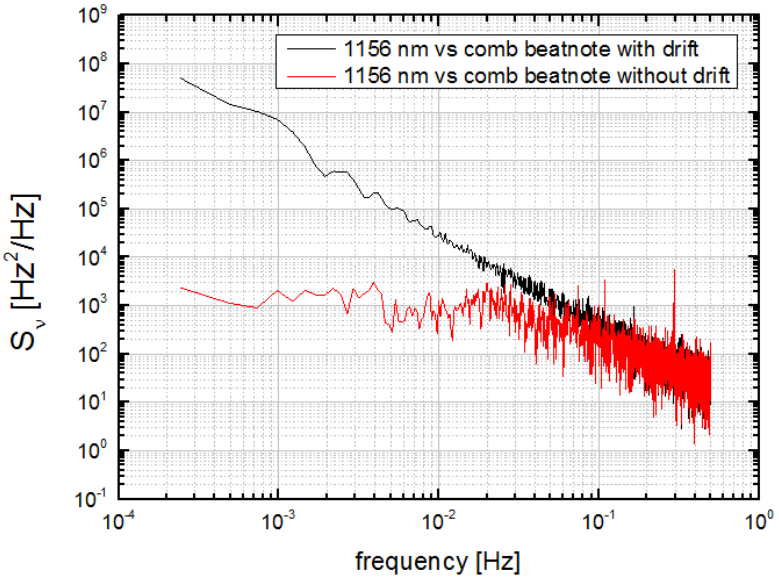

Figure 2.18: Comparison of the power spectral densities without (black dataset) and with (red dataset) the correction system implemented.

Chapter 3

$^1S_0 \rightarrow {}^3P_0$ absolute frequency measurement for ^{173}Yb

A first application of the new 578 nm laser setup is the measurement of the absolute frequency of the doubly forbidden transition $^1S_0 \rightarrow {}^3P_0$ for the isotope ^{173}Yb. This measurement can not only improve the experimental knowledge of this value, but also show the utility and effectiveness of a link system such as the LIFT for high-precision ultracold gases experiment. Recalling the Eq. 2.3, I highlight that this transition frequency was known before this master thesis work with an uncertainty of just 4.4 kHz and that ref. [41] is the only experimental measurement of this value in literature.

In this chapter I will describe the methods utilized to prepare the measurement and the analysis done for the absolute frequency evaluation with its uncertainty. About that it has been chosen to perform nuclear spin selective differential measurements in order to achieve an higher precision due to the estimate of systematic uncertain effects caused by magnetic fields and optical lattice frequency. I will illustrate differential measurements that allow us to remove the first order Zeeman shift and from which we extract the transition center. Over more, we will show also measurements thanks to which we have calibrated the systematic effects, as the second order Zeeman shift and the differential light shift.

I will also evidence the improvements produced by the implementation of the optical fiber link reference, showing the differences in these measurements with and without such a stabilization system.

3.1 $^1\mathrm{S}_0 \rightarrow {}^3\mathrm{P}_0$ transition theory

Until now we have denoted the $ns^2\ {}^1\mathrm{S}_0 \rightarrow nsnp\ {}^3\mathrm{P}_0$ transition as "doubly forbidden", let's see now why and which are the mechanism that permit the excitation of this transition in alkaline-earth atoms and more specifically in Ytterbium. This transition breaks the selection rules that require both $\Delta S = 0$ and J_i and J_f not simultaneously null. With ΔS we indicate the variation of the total internal spin quantum number and its rule represent the separation between the singlet and triplet spin states. J_i and J_f are the total electronic spin quantum numbers for the initial and final states respectively.

About the possibility to realize $\Delta S \neq 0$, it is allowed by the spin-orbit interaction that mixes states with different S making it no more a good quantum number. Similarly, the $J_i = J_f = 0$ transition is possible in presence of a mixing system for states with different J. Such a mechanism is represented by the hyperfine interaction between the total electronic angular momentum and the nuclear magnetic moment. This for the Ytterbium is the case of the fermionic isotopes, which are the subject of this master thesis.

3.1.1 Fermionic case

The isotopes that belong to this category are the ^{171}Yb and the ^{173}Yb and because of the intrinsic structure of the Ytterbium, having an odd number of nucleons, they are characterized by a nuclear angular momentum $I \neq 0$, and consequently by $F \neq 0$, and they exhibit an hyperfine structure. For these atoms the nuclear magnetic moment $\boldsymbol{\mu}_N$ is different from zero. It interacts with the magnetic field generated by the electrons and, as a result of this hyperfine interaction, $\mathbf{J}$ is no longer a conserved quantity. Since the coupling is much smaller then other interaction terms (e.g. spin-orbit coupling), we employ the first-order perturbation theory in the magnetic-dipole hyperfine interaction to obtain the modified atomic wave functions of the $|{}^3\mathrm{P}_0\rangle$ states, as demonstrated in [45]. Actually in this problem we should consider two types of interaction: the hyperfyne one and the interaction with the electromagnetic field. Anyway since the radiative width of the $^3\mathrm{P}_1$ level is much smaller than the fine-structure energy intervals between the components of the $^3\mathrm{P}_J$ multiplet, we will consider only the hyperfine-structure term and the one relative to the electromagnetic coupling negligible.

The atomic nucleus interacts through its magnetic moment with the magnetic fields $\mathbf{B}_i$ generated by the electrons of the incomplete shells. Therefore

the hyperfine interaction Hamiltonian is:

$$H_{hf} = -\sum_{i=1}^{N} \mathbf{B}_i \cdot \boldsymbol{\mu}_N = \mu_N g_I \sum_{i=1}^{N} \mathbf{B}_i \cdot \mathbf{I}_N \tag{3.1}$$

where μ_N and g_I are respectively the nuclear magneton and the giromagnetic nuclear factor. Since at the lowest order both B_i and I_N are spherical operators of rank one, it is possible to rewrite Eq. 3.1 as following:

$$H_{hf} = 2\mu_B \mu_N g_I \mathcal{T}^{(1)} \cdot \mathbf{I}^{(1)} \tag{3.2}$$

where μ_B is the Bohr magneton, $g_I \mu_N \mathbf{I}^{(1)}$ represents the nuclear magnetic dipole moment operator and $\mathcal{T}^{(1)}$ is an even-parity electronic coupling operator. The outline to obtain the decay ratio is:

$$\begin{cases} |^3\mathrm{P}_0'\rangle = |^3\mathrm{P}_0\rangle^{(0)} + |^3\mathrm{P}_0\rangle^{(1)} \\ \gamma_{^3P_0' \rightarrow {}^1S_0} = \frac{4\alpha_0^3}{3}\omega_0^3 \left|\langle {}^1\mathrm{S}_0| \mathbf{D} |^3\mathrm{P}_0'\rangle\right|^2 \end{cases} \tag{3.3}$$

with $\omega_0 = (E_{^3P_0} - E_{^1S_0})/\hbar$, α_0 the fine structure constant and $\mathbf{D}$ the electric-dipole operator. $\left|^3\mathrm{P}_0'\right\rangle$ is the new eigenstate given by the unperturbed $|^3\mathrm{P}_0\rangle^{(0)}$ state and the mixing $|^3\mathrm{P}_0\rangle^{(1)}$ depending on the first order hyperfine interaction perturbation. To describe the eigenstates we choose the basis $|\alpha(IJ), F, m_F\rangle$ with $\mathbf{F} = \mathbf{I} + \mathbf{J}$ the operator associated to the total angular momentum of the atom and $\alpha(IJ)$ the set of the other quantum numbers that define the state. With this notation we have:

$$|\alpha(IJ), F, m_F\rangle^{(1)} = \sum_{\alpha', J'} |\alpha'(IJ'), F', m_F'\rangle \frac{\langle \alpha'(IJ'), F', m_F' | H_{hf} | \alpha(IJ), F, m_F\rangle}{E(\alpha', J') - E(\alpha, J)} \tag{3.4}$$

Where, considering Eq. 3.2, the explicit form of the matrix elements of H_{hf} is:

$$\begin{aligned} &\langle \alpha'(IJ'), F', m_F' | H_{hf} | \alpha(IJ), F, m_F\rangle = 2\mu_B \mu_N g_I \delta_{FF'} \delta_{m_F, m_F'} \times \\ &\times (-1)^{F+I+J'} \sqrt{\frac{(2I+1)(I+1)}{I}} \begin{Bmatrix} I & I & 1 \\ J & J' & F \end{Bmatrix} \left\langle \alpha', J' \left\| \mathcal{T}^{(1)} \right\| \alpha, J \right\rangle \end{aligned} \tag{3.5}$$

From the expression above we note that H_{hf} does not commute with $\mathbf{J}$, producing eigenstates where $\mathbf{J}$ is not well defined. Since $\mathcal{T}$ is a tensorial operator with rank one, the new system eigenstates will be linear combinations of the unperturbed eigenstates with equal F and $J' = J, J \pm 1$. Therefore the metastable state $|^3\mathrm{P}_0'\rangle$ will be expressed by the relation:

$$\left|^3\mathrm{P}_0'\right\rangle = a \left|^3\mathrm{P}_0\right\rangle + b \left|^3\mathrm{P}_1\right\rangle + c \left|^1\mathrm{P}_1\right\rangle \tag{3.6}$$

with $b, c \ll 1$. This new defined state can decay now to the ground state $|^1\mathrm{S}_0\rangle$ through an electric-dipole transition and the decay rate, as expressed by the second line in Eq. 3.3, is different from zero and becomes:

$$\gamma_{^3P_0' \to ^1S_0} = \mathcal{C}\omega_0^3 |S_0|^2 \tag{3.7}$$

with $\mathcal{C}$ representing a product of various system constants and:

$$S_0 = \frac{\left\langle ^3\mathrm{P}_0 \left\| \mathcal{T}^{(1)} \right\| \alpha' J' \right\rangle \left\langle \alpha' J' \left\| \mathbf{D} \right\| ^1\mathrm{S}_0 \right\rangle}{E_{\alpha' J'} - E_{^3P_0}} \tag{3.8}$$

In the case of the $|^3\mathrm{P}_0'\rangle$ level of ^{173}Yb, from Eq. 3.7 the evaluated decay rate, and consequently the transition linewidth, is 38.5 mHz; it corresponds to a mean lifetime of about 26 s.

At the end of this treatise it deserves a brief mention the case of bosonic isotopes belonging to alkaline-earth atoms; for these atomic species the nuclear spin is null and therefore defect to energetic levels hyperfine structure. The quantum number J associated to the states $|^1\mathrm{S}_0\rangle$ and $|^3\mathrm{P}_0\rangle$ will be exactly equal to zero; without the mixing the decay process from the metastable level could happen only through a two-photon transition that for the alkaline-earth-metals is characterized by an extremely long mean lifetime that is in the case of Ytterbium of the order of a thousand years. For a detailed discussion regarding the natural linewidth see the reference [42]. On the other hand concerning the absorption it has been demonstrated the possibility of a total angular momentum mixing depending on the presence of an external magnetic field able to induce the transition. This technique is called Magnetically Induced Spectroscopy (MIS) and it has been demonstrated in [31] that, defined Δ_{fs} the fine structure splitting, the new eigenstate of the $^3\mathrm{P}_0$ level is:

$$\left|^3\mathrm{P}_0'\right\rangle = \left|^3\mathrm{P}_0\right\rangle + \frac{\Omega_B}{\Delta_{fs}} \left|^3\mathrm{P}_1, m_j = 0\right\rangle \tag{3.9}$$

with:

$$\left\langle ^3\mathrm{P}_1 | \boldsymbol{\mu} \cdot \mathbf{B} | ^3\mathrm{P}_0 \right\rangle \simeq \sqrt{2/3}\mu_B |B| = \hbar\Omega_B \tag{3.10}$$

A transition to this mixed state could now be made directly from the ground state and the $^1\mathrm{S}_0 \to {}^3\mathrm{P}_0'$ Rabi frequency is:

$$\Omega \approx \frac{\Omega}{\Delta\hbar} \left\langle ^1\mathrm{S}_0 | \boldsymbol{d} \cdot \mathbf{E} | ^3\mathrm{P}_1 \right\rangle = \frac{\Omega_L \Omega_B}{\Delta} \tag{3.11}$$

3.2 Measurement system

From the experimental point of view we have already discussed the preparation of an ultracold fermionic ^{173}Yb gas in section 1.2. In this section we

describe the experimental procedures used to manipulate and detect the spin state of the atomic cloud. With the term "spin state" we indicate m_F: the projection on the quantization axis of the total atomic angular momentum F, which for $|^1S_0\rangle$ and $|^3P_0\rangle$ corresponds to the nuclear angular momentum.

3.2.1 Optical pumping

To achieve an ^{173}Yb sample with a well-defined spin state the experimental setup was equipped (before this thesis work) with an optical pumping system. This permits to transfer atomic population between different m_F allowing us to prepare a sample with arbitrary components, both in number and in species, of the spin manifold. The mechanism uses two laser beams in resonance with the transition $^1S_0 \rightarrow {}^3P_1$ at 556 nm with circular polarization σ^+ and σ^-. In this way a population of the ground state $|^1S_0\rangle$ with spin state m_F is moved to states with $m'_F = m_F \pm 1$ of the level $|^3P_1\rangle$. This manipulation happens after loading the atoms in the crossed optical trap within the glass cell, before the switching on of the lattice beams. Two coils, placed symmetrically below and above the glass cell, produce at the center of the cell an uniform magnetic field of 20 G, oriented along the coils axis as shown in Fig. 3.2, which is also the propagation axis of the two optical pumping beams. The magnetic field generates a Zeeman shift of the two levels of about $m_F \times 207$ Hz/G for the $|^1S_0\rangle$ and $m_F \times 680$ kHz/G for the $|^3P_1\rangle$. Because the levels have a different relative Zeeman shift, with that of the $|^1S_0\rangle$ state much smaller than that of the $|^3P_1\rangle$ state, the degeneracy on the transition frequencies between different spin-states is removed: the new level separation ($\sim 680 * 20$ kHz) is much larger than the natural linewidth ($\sim 2\pi \times 180$ kHz). So it is possible to excite selectively the six hyperfine sub-levels of the ground state varying the frequency of the two laser beams. For the arrangement of the optical pumping setup see Fig. 3.2.

As a representative example, we describe the preparation of an atomic cloud with two spin components, $m_F = -5/2$ and $m_F = +3/2$. In Fig. 3.1 we illustrate all the steps outlined below. After loading the atoms in the crossed trap, we use the σ^- polarized beam to excite the transition $|^1S_0, m_F = +5/2\rangle \rightarrow |^3P_1, m_F = +3/2\rangle$ that allows us to transfer optically the $m_F = +5/2$ population of the ground state in the levels $m_F = +1/2$ and $m_F = +3/2$. Varying the beam frequency of 680 kHz$*\Delta(m_F) = 680*3$ kHz $=$ 2.040 MHz we excite now the $|^1S_0, m_F = -1/2\rangle \rightarrow |^3P_1, m_F = -3/2\rangle$ transition, emptying the state $m_F = -1/2$. We repeat the process to optically pump the state $m_F = -3/2$ into the state $m_F = -5/2$. Simultaneously, we use the σ^+ polarized beam set in resonance with the transition $|^1S_0, m_F = +1/2\rangle \rightarrow |^3P_1, m_F = +3/2\rangle$ in order to empty the $m_F = +1/2$ state. With the last

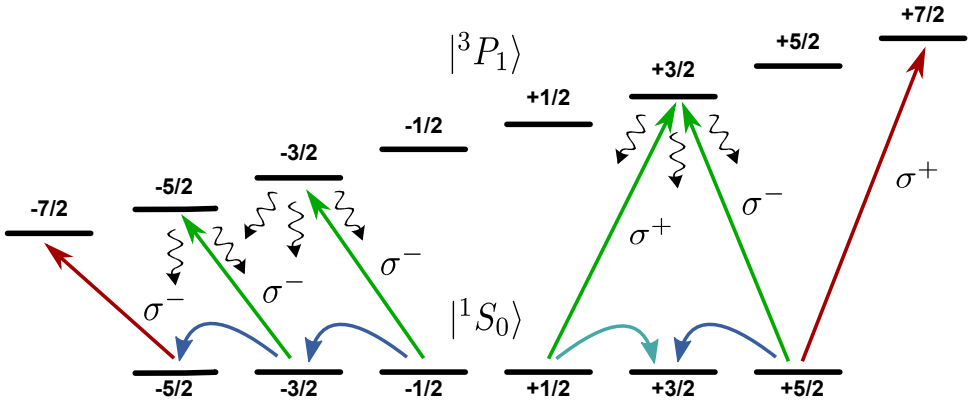

Figure 3.1: Example of the optical pumping method utilized to achieve a polarized atomic sample. Two circularly polarized beams σ^+ or σ^- (green arrows) are used to pump the state $m_F = -5/2, +3/2$ of the level $^1\mathrm{S}_0$. the black wavy arrows indicate the possible decay branch from the excited state. Resonance blast pulses with the closed transitions $|^1\mathrm{S}_0, m_F = \pm 5/2\rangle \rightarrow |^3\mathrm{P}_1, m_F = \pm 7/2\rangle$ (red arrows) are eventually applied to "clear" the atomic mixture from the undesired spin components.

pumping process a part of the $m_F = +1/2$ population has been transferred in the $m_F = +5/2$ state. Finished the pumping stage, all the atoms are in the $m_F = -5/2, +3/2, +5/2$ levels of the ground state. Then, evaporative cooling is performed by reducing the intensity of the crossed trap beams. Therefore a following blast pulse, realized exciting the closed transition $|^1\mathrm{S}_0, m_F = +5/2\rangle \rightarrow |^3\mathrm{P}_1, m_F = +7/2\rangle$, heats the atoms in the state $m_F = +5/2$, forcing them to leave the trap. Experimental evidence proves that this system is quick enough not to cause heating of the remaining atoms in the states $m_F = -5/2$ and $m_F = +3/2$.

In a similar way, it is possible to achieve other spin mixtures simply changing the sequence of the single optical pumpings. It is also possible to select a single spin component exploiting the two closed transitions to blast the population in excess. Concerning the balance between the populations in the two-spin mixture, this is adjustable varying the frequencies of the pump beam in order to change the detuning from the transition resonance and choosing in this way the pumping efficiency. The differences in a "well-balanced" mixture are less than the 5%. It is fair to stress that in principle for the spectroscopy of the $^1\mathrm{S}_0 \rightarrow {}^3\mathrm{P}_0$ transition on a single spin component it is not necessary to prepare a two-spin mixture, but it is a good way to indirectly control that the atom number remain constant, checking that the number of atoms of the out of resonance spin component remains constant during the measurement. Moreover, it will permit to change quickly the

component target of the spectroscopy without changing the experimental routine, except for the 578 nm laser frequency.

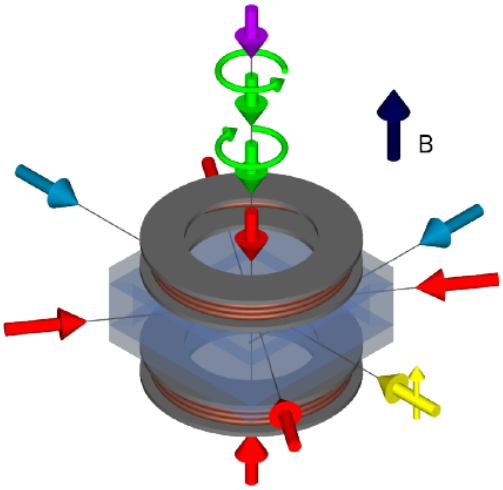

Figure 3.2: Laser beams arrangement at the glass cell: the lattice beams at 759 nm are shown in red, the optical pumping beams at 556 nm in green, the two beams that make up the optical crossed trap in blue, the 578 nm spectroscopy beam in yellow, the 399 nm imaging beam in purple. The figure also shows the coils in Helmholtz configuration to generate the magnetic field, represented with the black arrow.

When the sample is prepared in the state required from the experiment, the optical lattice beams are turned on while the laser beams that make up the optical cross-trap are gradually switched off. For the orientation of the beams in respect of the glass cell see Fig. 3.2.

3.2.2 Optical Stern-Gerlach

In addition to the sample preparation and the spectroscopy routine that will be described in Secs. 3.5 and 3.6, an appropriate imaging system is necessary. The experimental setup has an absorption imaging system that allows us to estimate the number of atoms that are in the electronic ground state $|^1S_0\rangle$. The imaging routine is performed after turning off the lattice beams and leaving the atomic cloud free to expand for a time that varies depending on the experimental requirements from 4 to 25 ms. At this point, after the ballistic expansion, a laser beam at 399 nm in resonance with the $|^1S_0\rangle \rightarrow |^1P_1\rangle$ transition illuminates the atoms and a CCD detector acquires the two-dimensional distribution of light which passes the atomic cloud. With

a fit algorithm, from the collected light it is possible to estimate the physical properties of the system such as the sample dimensions, the central position of the distribution, the number of atoms and their temperature.

For the experimental goals it is important to measure separately the atomic population for each m_F of the two-spin mixture, also as a check of the efficiency of the optical pumping procedure described before. Therefore a laser beam, red-detuned with respect to the transition $|^1\mathrm{S}_0, F = 5/2\rangle \rightarrow |^3\mathrm{P}_1, F = 7/2\rangle$, is exploit to impose a spin-dependent dipole force on the atoms. This method is called Optical Stern-Gerlach (OSG), due to the similarity with the famous Stern and Gerlach's experiment [46]. Consequently the various components are spatially separated and their population can be measured individually by the absorption imaging system already described. The beam used for the OSG routine is detuned with respect to the $^1\mathrm{S}_0 \rightarrow^3 \mathrm{P}_1$ transition by -566 MHz and is characterized by a waist of 50 μm and a power of 4 mW. The beam is displaced from the cloud center in order to make the atoms experience an intensity gradient as shown in Fig. 3.3(a). The light polarization is circularly σ^- and therefore only the $|^1\mathrm{S}_0, F = 5/2, m_F = m_i\rangle \rightarrow |^3\mathrm{P}_1, F = 7/2, m_F = m_i - 1\rangle$ couplings are allowed. Let's see briefly the process that is the basis of this method.

At the origin there is the second-order time-independent perturbation theory: an interaction (Hamiltonian H_{int}) leads to an energy shift of the i-th state (unperturbed energy $\mathcal{E}_i$) that is given by:

$$\Delta(\mathcal{E}_i) = \sum_{j \neq i} \frac{|\langle j\,|H_{int}|\,i\rangle|^2}{\mathcal{E}_i - \mathcal{E}_j}\,, \quad H_{int} = -\boldsymbol{\mu}\cdot\mathbf{E} \tag{3.12}$$

Where for an atom interacting with light the interaction Hamiltonian with the electric dipole operator $\boldsymbol{\mu} = -e\mathbf{r}$ has been considered. Considering the selection rule $\Delta(m_F) = -1$, the energy shift for a system with two levels, each of which is $2F + 1$ degenerate, is, for the ground state:

$$\Delta(\mathcal{E}_i) = \frac{\left|\left\langle {}^3\mathrm{P}_1, F = 7/2, m_F = m_i - 1\,|\boldsymbol{\mu}|^1\,\mathrm{S}_0, F = 5/2, m_F = m_i\right\rangle\right|^2}{\hbar\Delta}\,|E|^2 \tag{3.13}$$

where $\Delta = (\omega - \omega_0)$ is the detuning of the photon with respect to the transition energy $\hbar\omega_0$. Remembering the relations between the transition matrix elements and the corresponding reduced matrix element $\|\mu\|$ and the natural linewidth Γ [47]:

$$|\mu_{m_i, m_i - 1}|^2 = c_i^2\,\|\mu\|^2 = c_i \frac{3\pi\epsilon_0\hbar c^3}{\omega_0^3}\Gamma \tag{3.14}$$

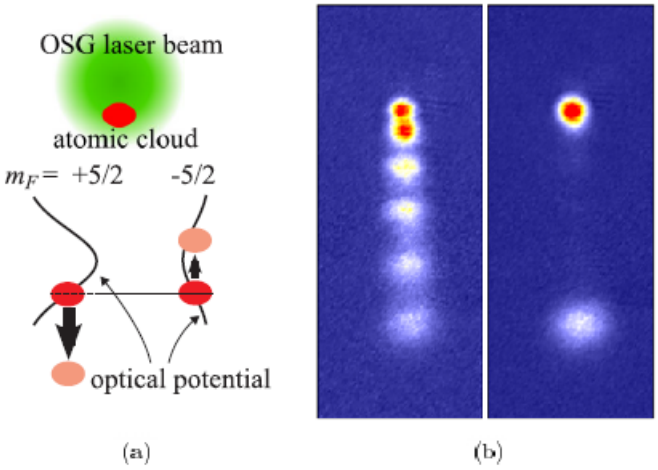

Figure 3.3: (a) Functional scheme of the Optical Stern-Gerlach (OSG) method [48]: a far detuned laser pulse lasting 2.5 ms is used to separate spatially the various component of the spin manifold. Before the imaging a ballistic expansion of 4.5 ms is performed. (b) Pictures of the atomic sample imaged after the OSG for six-component spin system (left) and two-component (right) system. The atoms populations have different densities but are balanced in number.

with $|\mu_{m_i,m_i-1}|$ the matrix element of 3.14, c_i the Clebsh-Gordan coefficient describing the addition of the photon angular momentum to the initial angular momentum states to yield the final angular momentum. Finally, considering that $I = 2\epsilon_0 c\,|E|^2$ and the fact that the laser beam isn't centered on the atomic cloud, we will have $I = I(\mathbf{r})$ and the energy shift will become an optical potential V_i depending on the position, the detuning with respect to the excited states, and by the ground spin state through the Clebsh-Gordan coefficient:

$$V_i = \frac{3\pi c^2 \Gamma}{2\omega_0^3} I(\mathbf{r}) \frac{|c_i|^2}{\Delta_i} \tag{3.15}$$

With the OSG process it is so possible to spatially split the ground states spin components and measure the two atomic population separately. The scheme and the results of this method is reported in Fig. 3.3.

3.3 How to perform the measurement and transition shifts

In a high precision measurement such as the one that we are going to describe, many experimental requirements and expedients are necessary in order to in-

crease the accuracy with which we will evaluate the transition frequency and to reduce as much as possible the uncertainty, that will be represented essentially by the spectroscopic linewidth. Both the precision and the accuracy depend on two general factors: the laser's specifics and the experiment's features.

First of all, it is obviously essential the presence of a frequency standard to compare the spectroscopic measurement to. In our case it will be represented by the INRIM's reference coming from Turin. Concerning the laser, it is characterized by a linewidth of at most 46 Hz, estimated in [28], and the dedrift system developed in this thesis work will guarantee its stability at the level of 10^{-15} on the timescale of an hour.

The precision of a spectroscopic measurement in the optical domain is usually limited by the residual Doppler broadening:

$$\Delta_D = \sqrt{\frac{8k_B T \ln 2}{mc^2}}\nu_0 \tag{3.16}$$

where Δ_D is the FWHM of the Doppler gaussian distribution, k_B the Boltzmann constant, c the speed of light in vacuum, m the atom mass and ν_0 the transition frequency. For an ultracold sample of ^{173}Yb at 100 nK, choosing for $^1S_0 \rightarrow {}^3P_0$ the approximate value $\nu_0 \sim 518$ THz, we found $\Delta_D \sim 280$ kHz. To avoid this issue we perform the measurement on atoms trapped in optical lattices. In the limit in which the atomic wavefuction can be considered well-localized inside a lattice site, the presence of the trapping potential limits the transitions that lead to a change of the atomic motion state. This phenomenon is called Lamb-Dicke effect and we will examine it in depth in Sec. 3.3.1.

On the other hand, an uncertainty on the lattice depth and frequency causes a shift of the discrete levels energies inside the potential well and consequently of the transition frequency, limiting the accuracy. The other contributions to the measurement inaccuracy are the Zeeman shift due to the presence of magnetic fields and the probe shift depending on the 578 nm radiation itself.

3.3.1 Lamb-Dicke regime

We have already mentioned this phenomenon as the basis of the Doppler broadening suppression. We consider an atom trapped in an optical lattice produced by a standing wave of laser light with wavelength λ. The atom wave function will be considered well localized if the uncertainty on its position Δx is much smaller than the lattice wavelength λ. For high lattice depth each

site of the lattice could be approximated with an harmonic well potential. So, we can consider an atom confined in an harmonic unidimensional potential and we write the eigenstate through the notation $|\alpha, n\rangle$, with α set of quantum numbers associated to the electronic state and n corresponding to the harmonic oscillator state of the atomic center-of-mass motion. We define ω_z as the harmonic trap frequency and pick an electric field that characterized by a trap frequency ω_L of the type:

$$E(z) = E_0 e^{-i(\omega_L t - kz)} \tag{3.17}$$

where ω_L is the excitation laser frequency, k is the laser wavevector and z is the coordinate of the center of mass coordinate[1]. In this approximation the transition probability $|g, n\rangle \rightarrow \left|e, n^{'}\right\rangle$, with $|g\rangle$ and $|e\rangle$ that indicate respectively the electronic ground and excited state, will be:

$$P \propto \left|\langle e\,|\mathbf{D}|\,g\rangle \left\langle n'\left|e^{ikz}\right|n\right\rangle\right|^2 \tag{3.18}$$

with $\mathbf{D}$ is the electric-dipole operator. Considering the motion part, we could relate the z coordinate to the creation and annihilation operators through the relation:

$$kz = kz_0(a + a^\dagger) = k\sqrt{\frac{\hbar}{2m\omega_z}}(a + a^\dagger) = \sqrt{\frac{E_r}{\hbar\omega_z}}(a + a^\dagger) = \eta(a + a^\dagger) \tag{3.19}$$

where $E_r = \hbar^2 k^2/2m$ is the recoil energy, $\hbar\omega_z$ represents the energy difference between two harmonic oscillator states that depends on the lattice depth and η is the Lamb-Dicke parameter. If $\eta \ll 1$ we can expand the exponential in 3.18 in series and obtain:

$$\begin{aligned} P &\propto \left|\left\langle n'\left|e^{i\eta(a+a^\dagger)}\right|n\right\rangle\right|^2 = \left|\left\langle n'\left|1 + i\eta(a + a^\dagger) + \mathcal{O}(\eta^2)\right|n\right\rangle\right|^2 = \\ &= \left|\delta_{n,n'} + \eta\sqrt{n+1}\delta_{n',n+1} + \eta\sqrt{n}\delta_{n',n-1}\right|^2 \end{aligned} \tag{3.20}$$

It is evident from 3.20 that transitions which change the motion state of the atom are suppressed at least by an η^2 factor with respect to the case where n is conserved. In optical lattices the transitions with $\Delta n \neq 0$ are called "sidebands" and often those with $\Delta n > 1$ are very unlikely.

In the case of the Yb clock transition the linewidth is much smaller than the sidebands separation and therefore they can be spectrally separated. Furthermore, considering that $\omega_z = 2\frac{E_{R_l}}{\hbar}\sqrt{s}$ [53], where E_{R_l} is the recoil

[1] In this treatise we have disregard the nucleus-electron coordinate since in general much smaller than z.

energy due of the interaction with the lattice field, and $s = 30$ as typical value in our measurements, we obtain an evaluation of the Lamb-Dicke parameter:

$$\eta = \left(\frac{\lambda_l}{\lambda_L}\right) \frac{1}{\sqrt{2}s^{1/4}} \simeq 0.4 \tag{3.21}$$

Therefore $\eta^2 \simeq 0.15$ allows us to consider the Lamb-Dicke regime a good approximation in our experimental conditions.

3.3.2 Zeeman shift

Removed the Doppler limit in spectroscopic precision of the $^1S_0 \rightarrow {}^3P_0$ transition in an optical lattice, the sensitivity to external magnetic field shift is a central problem for the absolute frequency accuracy. Even if the transition $^1S_0 \rightarrow {}^3P_0$ is between states with electronic spin equal to zero, the high precision of this measurement requires to consider also the effects related to the nuclear spin and to other mechanism due to the states mixing.

In the hypothesis of weak magnetic field, directed along the z axis, the Hamiltonian for the Zeeman interaction, is given by:

$$H_z = (-g_S S_z - g_L L_z + g_I I_z)\mu_0 B \tag{3.22}$$

with $g_S \simeq 2$, $g_L = 1$ and g_I the spin, orbital and nuclear angular momentum g-factors respectively, S_z, L_z and I_z the z components of the electron spin and orbital and nuclear angular momentum and $\mu_0 = \mu_B/h$, with μ_B the Bohr magneton. In Eq. 3.22 is used the convention for which g_I contains a multiplicative $\mu_N/\mu_B \approx 1/1836$ factor with respect of the one presented in Eq. 1.1; in absence of state mixing, the g_I factors for the $^1S_0$ and $^3P_0$ are the same and equal to $-1.48 \cdot 10^{-4}$. However, the hyperfine interaction modifies the $^3P_0$ wave function leading to a differential g-factor δg, given by:

$$\delta g = -\frac{\langle {}^3P_0 | H_z | {}^3P_0 \rangle - \langle {}^1S_0 | H_z | {}^1S_0 \rangle}{m_F \mu_B B} \tag{3.23}$$

Its value for the ^{173}Yb has been estimated to be $\delta g = -8.1 * 10^{-5}$ [49]. The resulting linear Zeeman shift of the $^1S_0 \rightarrow {}^3P_0$ transition for linear polarization is:

$$\Delta\nu_z^{(1)} = -\delta g m_F \mu_0 B \simeq m_F B \times 113 \ \frac{\text{Hz}}{\text{G}} \tag{3.24}$$

If we use a single spin projection m_F, the uncertainty related to this effect would be evaluated indirectly by the knowledge of the magnetic field inheriting its relative uncertainty. However, in the spectroscopy is performed

simultaneously on a two spin mixture, it is possible to measure the average transition frequency between two different m_F. In this way we measure directly the differential linear Zeeman shift and we can cancel it. The requirement for such technique is that the magnetic field is intense enough to resolve the sublevels, that in our experimental case is always verified because of the linewidth of the clock transition is extremely narrow. Moreover, we have to consider the second order Zeeman shift $\Delta\nu_z^{(2)}$. This shift arises from second order processes involving levels separated in energy by the fine structure splitting, and is dominated by the interaction between the $^3\mathrm{P}_0$ and the $^3\mathrm{P}_1$ states, since the ground state is separated from all other levels by optical energy. Therefore $\Delta\nu_z^{(2)}$ for linear polarization will be:

$$\begin{aligned}\Delta\nu_z^{(2)} &= -\sum_{F'} \frac{\left|\langle {}^3\mathrm{P}_0, F, m_F| \, H_z \, |{}^3\mathrm{P}_1, F', m_F\rangle\right|^2}{\nu_{{}^3P_1,F'} - \nu_{{}^3P_0}} \simeq \\ &\simeq -\frac{4}{5}\alpha^2 \frac{(g_L - g_S)^2 \mu_0^2}{\nu_{{}^3P_1} - \nu_{{}^3P_0}} B^2 = \eta B^2\end{aligned} \tag{3.25}$$

The approximation in Eq. 3.25 is due to having expressed the matrix elements in terms of pure states, defining α from:

$$\left|{}^3\mathrm{P}_1\right\rangle = \alpha \left|{}^3\mathrm{P}_1^0\right\rangle + \beta \left|{}^1\mathrm{P}_1^0\right\rangle \tag{3.26}$$

and to using the matrix elements given for the cases $F = 5/2$, $m_F = \pm 5/2$ [2].

With $\alpha = 0.992$ [31] we find $\eta \simeq -7.4 \cdot 10^{-2}$ (Hz/G^2).

3.3.3 Lattice frequency uncertainty shift

Now we consider the light shift induced by the trapping light on the $^1\mathrm{S}_0$ and $^3\mathrm{P}_0$ energy levels, causing a frequency shift of the clock transition. We

[2] We have chosen the F value of the ground state and its projection on the quantization axis $|m_F = 5/2|$utilized during the measurements of the Zeeman shift. The Zeeman Hamiltonian connects states with $\Delta J = 0, \pm 1$ and therefore F' could be $F, F \pm 1$. Since in general $-F < m_F < +F$ and in our case $m_F = 5/2$, the transition with $\Delta F = -1$ must be discarded. The remaining generic matrix elements are:

$$\begin{aligned}\left\langle {}^3\mathrm{P}_0^0, F, m_F\right| H_z \left|{}^3\mathrm{P}_1^0, F' = I, m_F\right\rangle &= (g_S - g_L)\mu_0 B m_F \sqrt{\frac{2}{3I(I+1)}} \\ \left\langle {}^3\mathrm{P}_0^0, F, m_F\right| H_z \left|{}^3\mathrm{P}_1^0, F' = I+1, m_F\right\rangle &= (g_S - g_L)\mu_0 B \sqrt{\frac{((I+1)^2 - m_F^2)(4I+6)}{3(I+1)(4(I^2+1)-1)}}\end{aligned} \tag{3.27}$$

where $I = 5/2$.

consider an atom with m mass which interacts with an electric field

$$\mathbf{E}(\mathbf{r},t) = \hat{\mathbf{e}}\frac{1}{2}(E_0(\mathbf{r},t)e^{-i(\omega t+kz)} + h.c.) \tag{3.28}$$

where $\hat{\mathbf{e}}$ and $\omega/2\pi$ are the polarization versor and the frequency of the field, respectively. We have already shown in Eq. 3.12 the interaction between atom and field in the limit that of $E_0(\mathbf{r},t)$ varies spatially on a distance much greater than the atomic dimension. Within this approximation, the interaction generates an energy light shift of the atomic levels, expressed by:

$$\Delta E_n = \frac{1}{4\hbar}\sum_{m\neq n}\frac{\omega_n-\omega_m}{(\omega_m-\omega_n)^2-\omega^2}\left|\langle m\left|\mathbf{D}\cdot\hat{\mathbf{e}}\right|n\rangle\right|^2 E_0^2(\mathbf{r}) \tag{3.29}$$

with $\hbar\omega_i$, $i=\{n,m\}$, the energy of the unperturbed atomic levels and $\mathbf{D}$ the electric dipole moment operator. Eq. 3.29 can be rewritten in term of the atomic polarizability α, defined as:

$$\alpha_n = -\frac{1}{\hbar}\sum_{m\neq n} -\left(\frac{\omega_m-\omega_n}{(\omega_m-\omega_n)^2-\omega^2}\left|\langle m\left|\mathbf{D}\cdot\hat{\mathbf{e}}\right|n\rangle\right|^2\right) \tag{3.30}$$

If we consider a two level system, it will be $m,n=\{e,g\}$, and the differential light shift, also called ac-Stark shift, will assume the form:

$$\Delta E_{eg}(\omega) = \frac{1}{4}(\alpha_g(\omega)-\alpha_e(\omega))E_0^2 \tag{3.31}$$

It is already evident that this term is very important if we want to determinate the absolute transition frequency $^1\mathrm{S}_0 \rightarrow {}^3\mathrm{P}_0$ with high accuracy and it is clear that for spectroscopic measurements in optical lattice it is fundamental to reduce as much as possible ΔE_{eg}. This can be obtained realizing the optical lattice at the wavelength for which the polarizabilities of the ground and excited states are equal, defined magic wavelength λ_m. In the case of Ytterbium clock transition, the choice fell on the wavelength corresponding to 759.35 nm. It has been preferred to others, as for example those at 551.5 nm and 465.4 nm, because it is distant from other resonances and for the feasibility with which it can be achieved. In fact laser light at high power ($\sim$ 0.5 W for every lattice beam) at this wavelength can be obtained by a Titanium-Sapphire laser.

However, since in general the two polarizabilities α_g and α_e are very affected functions of ω, on the differential light shift there are also the contributions, in addition to the scalar term introduced in 3.30, proportionals to

the vectorial and tensorial polarizability of the field. An evaluation of these terms has been done in [50] and results in:

$$\begin{aligned}\Delta\nu_e &= -\{k_e^S + k_e^V \xi m_F + k_e^T[3m_F^2 - F(F+1)]\}s \\ \Delta\nu_g &= -\{k_g^S + k_g^V \xi m_F + k_g^T[3m_F^2 - F(F+1)]\}s\end{aligned} \tag{3.32}$$

where $\Delta\nu_{g,e}$ are the Stark shifts of the single g or e level, $k_{g,e}^S$, $k_{g,e}^V$ and $k_{g,e}^T$ the shift coefficients proportional to the scalar, vector or tensor polarizabilities, $s = U_T/E_R$ is the lattice depth parameter and ξ the degree of elliptical polarization, with $\xi = 0$ that represents the linear polarization, $\xi = \pm 1$ the perfect circulars. For a pure linear polarization (π) of the resonance light the new ac-Stark shift of the transition ($\Delta m_F = 0$) is:

$$\Delta\nu'_{eg} = -[\Delta k^S - \Delta k^T F(F+1)]s - (\Delta k^V m_F \xi + \Delta k^T 3m_F^2)s \tag{3.33}$$

where Δk are the shift coefficient due to the differential polarizability.

Due to the presence of a m_F dependence in Eq. 3.33, the Stark shifts cannot be completely compensated for all of the sublevels simultaneously. This means that we will have different magic wavelength depending on the sublevel used. The significance of this effect depends on the magnitude of the

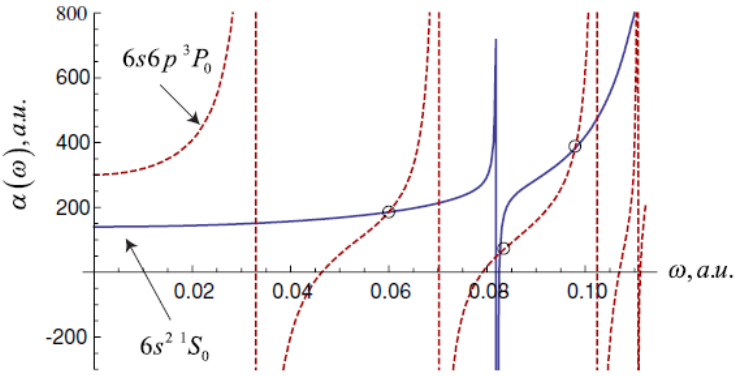

Figure 3.4: Comparison between the polarizabilities estimated of the $|^1S_0\rangle$ and $|^3P_0\rangle$ states of ^{173}Yb [51]. The magic wavelength occurs when the two polarizabilities intersect off resonance (circled points). For ^{173}Yb their values are, from left to right: 759.354 nm (experimental, [52]), 551.5 nm and 465.4 nm.

tensor and vector terms. In the case of $^1S_0$ and $^3P'_0$, they are electronically scalar, hence these effects are expected to be quite small. In Fig. 3.4 the polarizabilities of the $^1S_0$ and $^3P'_0$ system are shown.

Now we can write the transition frequency with the all the shift contributions considered so far, namely both Zeeman (with reference at Eq. 3.24

and 3.25) and light shift:

$$\begin{aligned}\nu_\pi =& \nu_c + \Delta\nu_z + \Delta\nu'_{eg} = \nu_c - \delta g m_F \mu_0 B - \frac{4}{5}\alpha^2 \frac{(g_L - g_S)^2 \mu_0^2}{\nu_{^3P_1} - \nu_{^3P_0}} B^2 + \\ &- \Delta k^S s - [\Delta k^V m_F \xi - \Delta k^T F(F+1) + \Delta k^T 3 m_F^2] s\end{aligned} \tag{3.34}$$

with ν_c the bare transition frequency. In conclusion, we recall that the linear Zeeman shift can be removed performing the spectroscopy with a two spin mixture and underline that the non-scalar polarizability contributions are estimated [52] of the order of 10.2 mHz for a $s = 30$ (the value that will be used in Sec. 3.6 in order to measure the absolute clock transition frequency) and they will be negligible with respect to the others terms.

3.4 Experimental conditions

The objective of this section is to outline in detail the measurement procedure and the physical conditions in which it has been performed. In the first instance we start from the 578 nm laser setup already shown in Sec. 2.1: the laser beam comes from the table with the SHG cavity through a polarization maintaining optical fiber and then it is expanded by a telescope formed by two lenses, up to a waist of 1 mm; this value has been chosen in order to obtain an uniform intensity of the laser on the whole volume affected by the optical lattice, $\sim 100\ \mu\text{m}^3$. This was possible since the 578 nm laser power reached at the end of the fiber is up to 20 mW, more than enough for every spectroscopy measurement of this ultranarrow transition. In fact, the power and the frequency of the laser beam will be variated through the AOM_s driver and the maximum intensity near the cell that we can reach is 700 mW/cm^2, for a power as we already mentioned of 20 mW. This intensity value is much grater than the saturation intensity (of which we discuss in detail at the end of this section), that represents the intensity over which the number of the intensity of the spectroscopic line does not depend from the intensity of the excitation beam. For our experimental purpose will be sufficient power values $\leq 1\ \mu$W. After the telescope, a beam splitter polarizer followed by a $\lambda/2$ and $\lambda/4$ waveplates clear the laser polarization making it linear and parallel to the axis of the magnetic field generated by the coils. Finally a mechanical shutter placed before the glass cell allows us to block and unblock again the excitation radiation in time of the order of 1 ms. The system is shown in Fig. 3.5. The frequency control of the AOM_s driver is done remotely via software through an Agilent 33522A wave generator. The excitation of the clock transition takes place after the atoms have been trapped in the optical lattice beams.

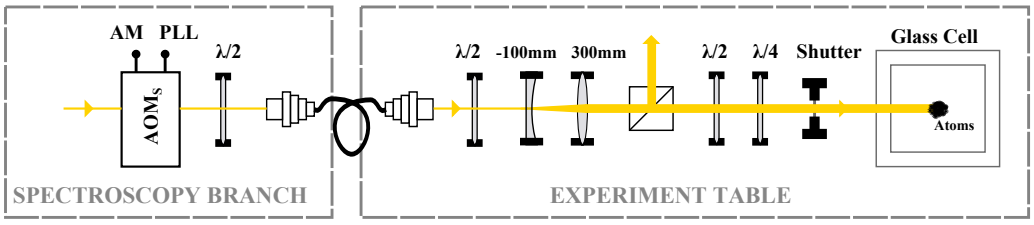

Figure 3.5: Final part of the spectroscopy setup, with reference also to Fig. 2.1. The figure is not in scale: in particular the waist of the laser beam after the telescope, formed by the two lenses, is 1 mm, the radius of the atoms cloud ~ 20 μm.

Now we consider the technique employed to observe this very weak transition. Measuring its fluorescence is very difficult since the scattering rate is too small. An efficient method to make spectroscopy measurements on clock transitions is the *electron shelving* [31]. The basis of this technique is to observe the depletion of the atomic population of one of the two clock states (the ground state in our case) through the absorption measurement on an permitted and easily observed transition after the population transfer into a long-lived *shelving* state (for us, the $^3P_0$). In this way from the atom number of the ground state, known the initial total population, we obtain the number of the excited atoms. In this case the shelving state is the metastable $^3P_0$ itself and the ground state population imaging is done through 399 nm radiation on the $^1S_0 \rightarrow ^1P_1$. The long mean lifetime of the $^3P_0$ of about 23 s prevents unwanted decay ruin the measurement.

From what we have seen, coupled with the fact that every imaging measurement has a *destructive* effect on the sample, two factors become crucial: the atom number stability and the laser frequency stability. In fact, at the same laser frequency we could expect the percentage of non-excited atoms to be the same, but its absolute number will change depending on the total number of atoms, excited and non-excited. This phenomenon causes an amplitude noise on the measurement. Furthermore, the setup is not designed for the precision spectroscopy or to be used as atomic clock, but to perform experiments with degenerate quantum gases. For this reason, the process of atoms cooling and trapping needs 35 s and therefore a frequency spectrum composed by few tens of points needs an acquisition time of about 30 minutes at least. For such long times the problems related to the experimental setup stability could be limiting; anyway the biggest problem, related to the 578 nm laser stability due to the ULE's drift, has been limited with the dedrift system.

Preliminary to the measurement, we need to identify the setpoint $f_{setpoint}$

at which the beatnote between the 1156 nm laser and the optical locked frequency comb has to be stabilized and therefore the frequency at which the 578 nm laser is maintained (see Sec. 2.3.1). To do that, we put the experimental system in conditions near the ones with which the absolute transition frequency measurement will be performed after the evaluation of the systematic uncertainties. So we had set the coils current in order to achieve a magnetic field of about 60 G, an optical lattice beams frequency λ_L near to the magic wavelength, $\nu_L = c/\lambda_L = 394.633$ THz, and finally an optical lattice depth $s = 30$. In particular this last setting could be useless if we would be exactly at the magic wavelength $\lambda_m = c/\nu_m$, since the terms depending on s in the Eq. 3.34 were identically zero; knowing it will allow us to remove the error due to the difference $\Delta\nu_m = \nu_L - \nu_m$ after an opportune calibration (see Sec. 3.5.2).

As spectroscopy frequency f_s of the 578 nm laser we had chosen the frequency of the laser stabilized to the ULE's cavity mode closest to the atomic transition frequency and passing through AOM_s with a frequency modulation of +40 MHz. Thus Eq. 2.1 and 2.2 become:

$$f_s = f_{ULE} + 2f_{AOM_{ULE}} + 40 \text{ MHz} \tag{3.35}$$

and the setpoint will be found changing the AOM_{ULE} frequency. After its evaluation, f_s will represent the zero-point on the x-axis of our spectroscopic measurements. In these conditions preliminary spectroscopy measurements had been performed with different two-spin mixtures in order to make the transition resonance frequencies, affected by the Zeeman shift, symmetrical with respect to the zero-point for opposite m_F. In Fig. 3.6 I report the results of this calibration for $f_{setpoint} = 21.477218$ MHz for the spin mixtures $m_F = \{-5/2, +5/2\}$ and $m_F = \{-5/2, +3/2\}$. The central peaks refer to a system with two atoms placed in a single lattice site, while the lateral peaks are related to the $^1\mathrm{S}_0 \rightarrow ^3\mathrm{P}_0$ single particle transitions of the two different spin components that form the mixture. The results are fitted with a lorentzian distribution and in the caption we report the center values of the resonances. We observe in the top image that the centers of the $m_F = -5/2$ and $m_F = +5/2$ resonances are symmetrical, with a difference between the centers $|x_c(-5/2) - x_c(+5/2)| = 10$ Hz, less than the uncertainties relative to the single resonance. Furthermore, comparing the two images we note that the peak of the $m_F = -5/2$ component remains at the same frequency within the uncertainty and the peak related to the $m_F = +3/2$ component is placed where we expect considering the linear Zeeman shift. Therefore this value of $f_{setpoint}$ was maintained for all the following measurements.

Once decided the setpoint, we can now univocally extract the frequency f_s of the 578 nm spectroscopy laser in function of the INRIM reference fre-

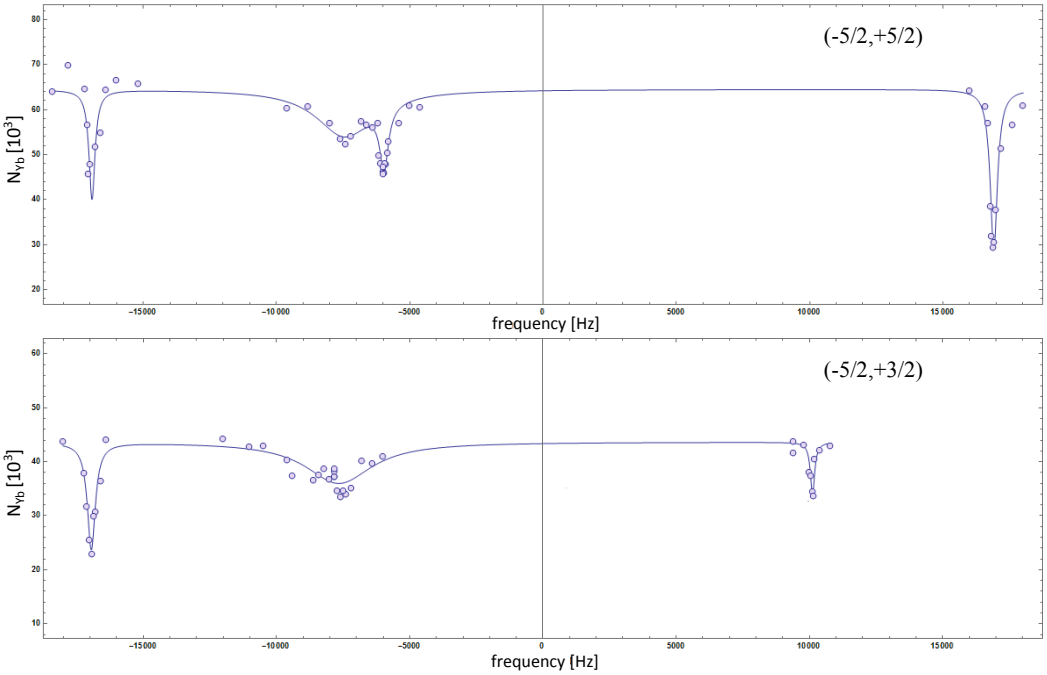

Figure 3.6: Spectroscopy spectra of the clock transition for $\{-5/2, +5/2\}$ (top image) and $\{-5/2, +3/2\}$ (bottom image) mixtures carried out in a 3D optical lattice at a lattice laser frequency $\nu_L = 394.633$ THz with a 578 nm laser power of $P_e = 30$ μW and an exciting time of $t_e = 100$ ms. The lines are lorentzian fits of the data. **Top image**: $x_c(-5/2) = -16923 \pm 19$ Hz, $x_c(+5/2) = 16913 \pm 12$ Hz; the magnetic field evaluated from Eq. 3.24 (considering only the linear term of the Zeeman shift) is $\Delta(f)/[113\ \text{Hz/G} * \Delta(m_F)] \simeq 59.9$ G. **Bottom image**: $x_c(-5/2) = -16947 \pm 13$ Hz, $x_c(+3/2) = 10115 \pm 16$ Hz; The theoretical center expected for the $m_F = +3/2$ component is $x_c(-5/2) + [113\ \text{Hz/G} * 59.9 * 4] \simeq 10128$ Hz, consistent within the measurement uncertainty.

quency. This is possible since the stabilization system discussed in chapter 2 has the effect of maintaining the quantity $2f_l = f_{ULE} + 2f_{AOM_{ULE}}$ constant, and therefore f_s too. In fact, with reference to the expressions 2.7 and 2.8, it can be expressed also in function of the frequency comb parameters:

$$2f_l = N_{1156}\nu_{RR} + \nu_{offset} + f_{setpoint} \tag{3.36}$$

From 2.7, we can also express ν_{RR} as function of the INRIM reference, i.e.:

$$\nu_{RR} = \frac{\nu_{Tu} - \nu_{offset} - f_{beat_{Tu}}}{N_{Tu}} \tag{3.37}$$

With the values given in Eq. 2.6, 2.7 and 2.8, we obtain:

$$f_s = 518\ 294\ 576\ 845\ 700.9\ \text{Hz} \tag{3.38}$$

The uncertainty Δf_s that affects this measurement depends on the ones relative to the $m_F = -5/2, +5/2$ resonances and on the INRIM reference uncertainty; Δf_s will be evaluated in Sec. 3.6. This will be the frequency value around which we will perform the various resonance measurements. The unique contribution that we have not considered yet in this evaluation is the Hydrogen maser shift with respect to the Cesium fountain, that depends on the time at which every measurement is performed (see Sec. 1.3.1).

For the linewidths Γ of the resonances we remark that they depend on the power of the excitation beam, through the relation:

$$\Gamma = \gamma\sqrt{1 + \frac{I}{I_s}} \tag{3.39}$$

Where γ is the natural linewidth, I the intensity of the laser beam and I_s the saturation intensity, defined as [53]:

$$I_s = \frac{\hbar\omega_0^3}{12\pi c^2\tau} \tag{3.40}$$

For the $^1S_0 \rightarrow ^3P_0$ transition of ^{173}Yb it is equal to $\simeq 4.7 \cdot 10^{-9}$ $\frac{\mathrm{mW}}{\mathrm{cm}^2}$. The measurements reported in Fig. 3.6 was done with a very large power of 30 μW corresponding to an intensity $I \simeq 10^{-4}\frac{\mathrm{mW}}{\mathrm{cm}^2}$. If we compare it with I_s we can note that the ratio $I/I_s \gg 1$ and therefore $\Gamma \simeq \gamma\sqrt{I/I_s} \gg \gamma$. This approximation will work for every value of the yellow laser power that we will use (from $\sim$ 600 nW up to $\sim$ mW).

In any case these preliminary measurements have shown the importance of the presence of an absolute reference to which our ultranarrow laser can be compared. This is evident if we decrease the 578 nm laser power at levels near the values used for the precision spectroscopy, ≤ 1 μW, and we try to get a transition spectrum without the dedrift stabilization system for long time in order to acquire many experimental points to achieve a good statistics. In this case, even if we are able to find the resonance, in few minutes, maintaining the AOM$_s$ frequency constant, it will not be visible anymore because of the ULE's drift. Consequently we have performed a measurement on the -5/2 spin component with repeated scans changing the AOM$_s$ frequency and in this way "following" the clock transition; the measurement is reported it in the top image in Fig. 3.7; it is shown the resonance frequency as a function of time. All the resonances have been acquired with the laser not dedrifted. The color of the points refers to the time at which the center of the resonance has been acquired, as shown in the plot legend on the right. We note that, in less than four hours of acquisition, the center of the resonance (or better the laser) has moved by about 1.3 kHz and that for times larger than $\approx$ 10

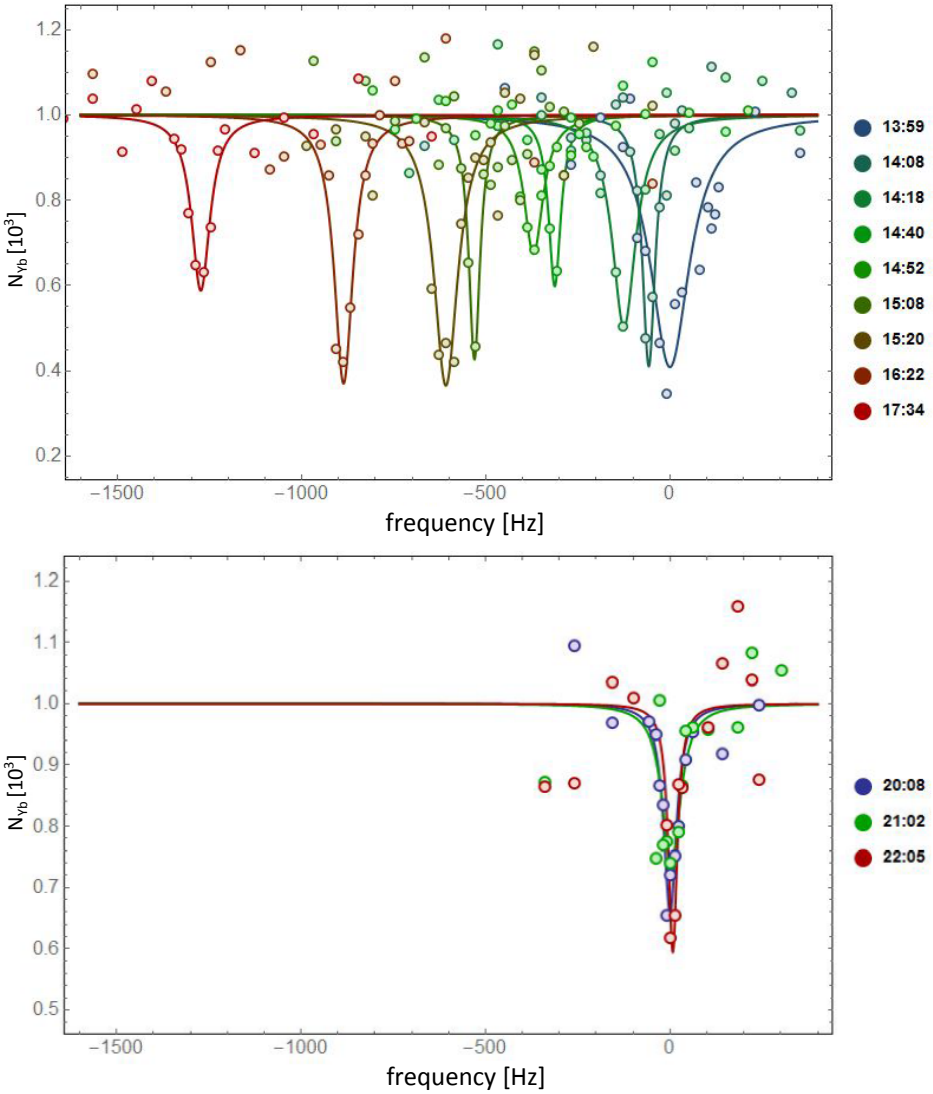

Figure 3.7: $^1S_0 \rightarrow {}^3P_0$ transition frequency measurement for the $m_F = -5/2$ spin component with a 578 nm laser power of $P_e = 1.0$ μW and an exciting time of $t_e = 100$ ms. The lines are lorentzian fits of the data and in the legend on the right is reported the starting time for each group dataset. **Top image**: measurement performed without dedrift correction. The depth and the width of the lines depend on the order of the points acquisition because of the ULE's drift. **Bottom image**: measurement performed with dedrift system. The spectroscopy line remains stable in time.

minutes it is not possible to observe a single resonance line. Then we have performed a similar measurement with the dedrift correction and the results are reported in the bottom image in Fig. 3.7. We note that in about three hours of acquisition the center of the spectroscopy line did not move. It is therefore clear that without the dedrift system that I have implemented and discussed in chapter 2, based on the absolute reference coming from INRIM, such a measurement on a long timescale ($>$ 10 minutes) could not be performed.

3.5 Systematic errors characterization

We have already discussed the various shift contributions to the $^1S_0 \rightarrow ^3P_0$ absolute frequency and in this section we will focus on their evaluation. From now on, every measurement of $^1S_0 \rightarrow ^3P_0$ resonance is performed taking advantage of the absolute INRIM reference and of the dedrift system. We started from the measurement of the magic frequency for the optical lattice. This has been performed, as explained in detail in Sec. 3.5.2, measuring the linear light shift as a function of the lattice depth; this measurement has required a lattice depth characterization, that we describe in Sec. 3.5.1. Once we found the magic frequency for the optical lattice, we have maintained the lattice beam frequency at the magic value and we have measured the resonance frequency at different values of magnetic field in order to estimate the quadratic Zeeman shift contribution, as described in Sec. 3.5.3. We recall that we will compensate the linear Zeeman shift performing the spectroscopy measurements with two different spin components: a $\{-5/2, +5/2\}$ mixture.

3.5.1 Lattice calibration

As we can see in Eq. 3.34, considering only the scalar term of the light shift, the transition frequency is a straight line as a function of the lattice depth parameter s. For this reason an opportune calibration of the lattice depth is fundamental in order to evaluate the possible difference between the lattice beams frequency.The technique used to perform the calibration is based on a lattice beam amplitude modulation, through which we could transfer atomic population from the fundamental band to the second excited one.

We start considering the Hamiltonian of an atom in a lattice: the optical potential that generates the lattice is separable in the various space components and therefore a cubic lattice could be lead back to the solution of the

stationary Schroedinger equation in the one-dimensional case:

$$H_0 = \left[-\frac{\hbar}{2m}\frac{d^2}{dx^2} + sE_R \sin^2(k_L x) \right] \psi = E\psi \tag{3.41}$$

where k_L is the wave-vector associated to the lattice beams and ψ the wave-function; the solutions associated to Eq. 3.41 are the Bloch functions:

$$\psi_{n,q}(x) = e^{iqx} u_{n,q}(x) = e^{iqx} \sum_K c_{K,q}^{(n)} e^{iKx} \tag{3.42}$$

where $u_{n,q}(x)$ is a function with the lattice periodicity, n the band index, q the quasimomentum and K a reciprocal lattice vector. We consider the amplitude modulation as a perturbation of this system, described by the Hamiltonian:

$$H_1 = sE_R \varepsilon \sin^2(k_L x) \cos(\pi f_{mod} t) \tag{3.43}$$

where f_{mod} and ε indicate respectively the frequency and the amplitude of the modulation. It is possible to demonstrate that if f_{mod} corresponds to:

$$f_{mod} = \frac{E_{q,2} - E_{q,0}}{h} \tag{3.44}$$

where $E_{q,n}$ is the energy of the n-th lattice band, then the modulation induce a resonant population transfer from the ground band to the second excited band. In fact, with the perturbation represented in Eq. 3.43, the transition probability from a band n to a band m is [54]:

$$W_{q,q'}^{nm} \propto \left| \sum_K c_{K,q}^{(n)} c_{K,q}^{(m)} (q' + K)^2 \delta_{q,q'} \right|^2 \tag{3.45}$$

From Eq. 3.45 we can see that the transition to an excited band is possible only if the atomic momentum is conserved. Moreover, Eq. 3.43 represents an even operator and presents matrix elements different from zero only between states with the same parity. Therefore, approximating the lattice potential with a harmonic one, that has states with defined and alternating parity, this explains why we use the modulation frequency that matches the fundamental band with the second excited band instead of the first.

Since this process heats the atoms and the lattice has a finite depth, then the transferred atoms are lost. Measuring the residual population as a function of the modulation frequency it is possible to find the resonance condition, corresponding to the condition of Eq. 3.44. Since the difference $E_{q,2} - E_{q,0}$ is a known monotonic function of the lattice depth, knowing f_{mod} we can evaluate the s parameter.

In order to extract s, we rewrite Eq. 3.41 as:

$$\frac{d^2\psi}{d\tilde{x}^2} + \left[\frac{E}{E_R} - \frac{s}{2} + \frac{s}{2}cos(2\tilde{x})\right]\psi = 0 \tag{3.46}$$

where $\tilde{x}$ is kx. In Eq. 3.46 we could recognize the Mathieu equation:

$$y''(z) + [a - 2\tilde{r}\ cos(z)]y(z) = 0 \tag{3.47}$$

imposing $a = E/E_R - s/2$ and $\tilde{r} = -s/4$. The ψ solution of the Eq. 3.46 are named *Mathieu functions* and are of the form:

$$\psi(\tilde{x}) = e^{i\tilde{q}\tilde{x}}\ f(\tilde{x}) \tag{3.48}$$

On the other hand the a parameters are named *characteristic values* of the Mathieu functions and they define the lattice band structure. It is also possible to evaluate a on varying $\tilde{q}$ with $\tilde{r} = -s/4$ fixed through numerical way and to obtain $E_{\tilde{q}} = [a_{\tilde{q}} + s/2]E_R$ from the a definition. For the periodicity of the Mathieu functions, $E_{\tilde{q}=0} = E_{q=0,n=0}$ and $E_{\tilde{q}=2} = E_{q=0,n=2}$. At this point, inserting $E_2(s)$ and $E_0(s)$ in Eq. 3.44, it is possible to plot the behavior of f_{mod} as a function of s, represented in Fig. 3.8.

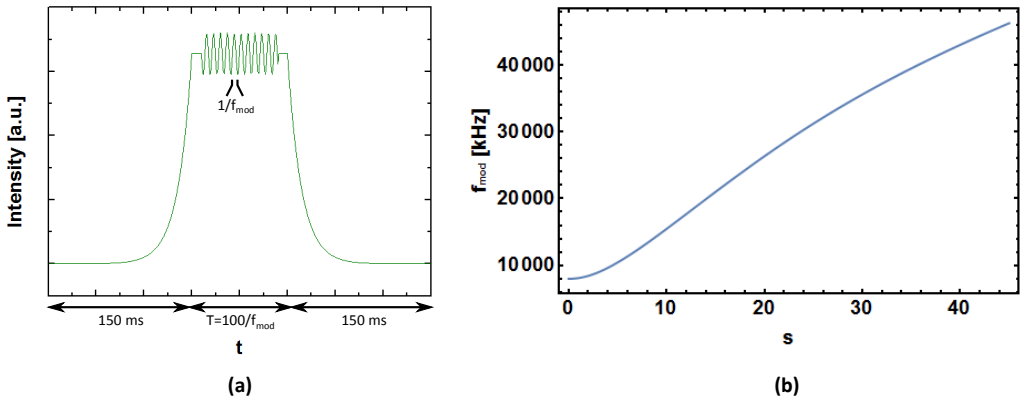

Figure 3.8: Procedure for lattice calibration: **(a)** time dependence of the intensity. **(b)** resonant modulation frequency f_{mod} for the transition between the fundamental and the second excited bands as a function of the lattice depth $s = V_0/E_R$.

The experimental procedure that now we will describe is repeated for each of the three lattice beams. First of all we turn on the beam with an exponential ramp in a time of 150 ms; then we apply an amplitude modulation of about 10% of the unperturbed beam intensity for a time $T = 100/f_{mod}$[3].

[3]The intensity of the unperturbed lattice beam is controlled by using individual AOMs on each of the beam paths.

Finally the beam is switched off, again with a ramp of 150 ms, and we run the imaging process in order to obtain the residual population. The time dependence of the lattice intensity is resumed in Fig. 3.8.

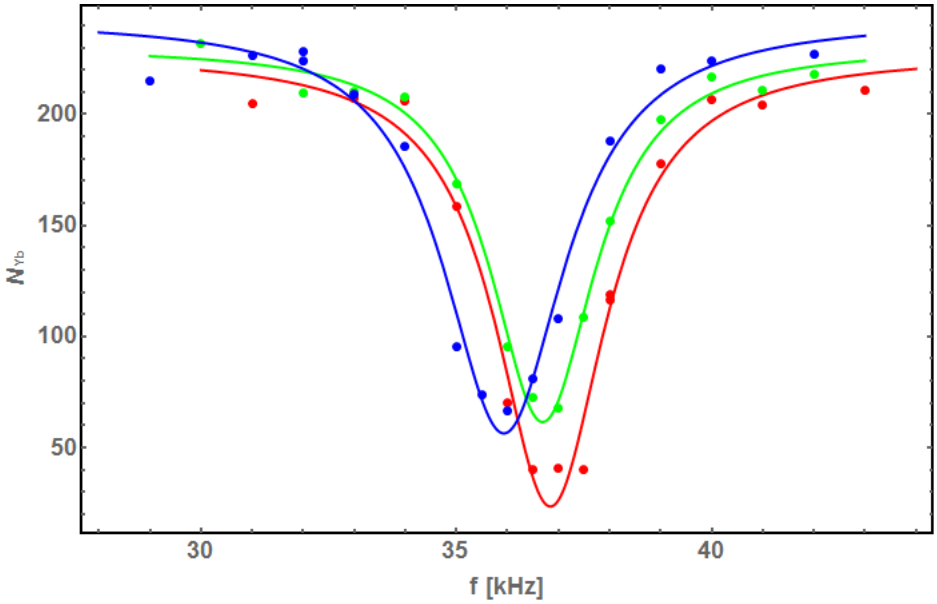

Figure 3.9: Example of lattice calibration for ^{174}Yb: the number of atoms remaining after the modulation is shown as a function of the modulation frequency for each of the three lattice beams, represented with different colors. The curves are a lorentzian fit of the experimental data.

Now once measured f_{mod_i}, where $i = \alpha, \beta, \gamma$ indicates the single lattice beam, varying the frequency of the amplitude modulation in order to obtain the population minimum, we can evaluate the s_i value for each lattice beam; an example of this kind of measurement is represented in Fig. 3.9. Finally the overall lattice depth is given by the geometrical average between the three s_i:

$$s = \sqrt[3]{s_\alpha s_\beta s_\gamma} \tag{3.49}$$

Since the s_i measurements are independent from each other, the error that affects the measurement of s is simply:

$$\Delta s = \frac{1}{3}\left[\frac{\Delta s_\alpha}{s_\alpha} + \frac{\Delta s_\beta}{s_\beta} + \frac{\Delta s_\gamma}{s_\gamma}\right] s \tag{3.50}$$

Finally, we note that the measurements in Fig. 3.9 have been performed with bosonic ^{174}Yb, in order to increase the measurement precision. Indeed, for a fermionic gas, in the limit in which the first band is completely filled,

there are atoms with every quasi-momentum q in the first Brillouin zone, not only in the neighborhood of $q = 0$ as in the bosonic case. Therefore for fermions the modulation frequency interval for which we observe an emptying of the population is greater than for bosons, hence the measurement would be less precise.

3.5.2 Magic wavelength evaluation

With the technique illustrated in the previous section for the calibration of the lattice depth, we have performed the measurements for the magic wavelength evaluation. This has consisted in the measurement of the $^1S_0 \rightarrow ^3P_0$ transition frequency as a function of the lattice depth for different lattice beams frequencies: at the magic frequency, the absolute transition frequency doesn't change varying the s parameter. To perform this measurement we have chosen three different values for the lattice depth; for each we have done a set of three measurements at three different lattice beams frequencies, each performed with two spin components, with the $m_F = \{-5/2, +5/2\}$ mixture.

Therefore for every point we have acquired the resonance for both the spin components, each characterized by a fit uncertainty σ_j on its center, where $j = -5/2, +5/2$ indicates the spin component. From now on, in this type of measurements the absolute frequency value is given by the average between the centers of the two lorentzians and the uncertainty by:

$$\sigma_a = \frac{\sqrt{\sigma^2_{-5/2} + \sigma^2_{+5/2}}}{2} \tag{3.51}$$

To obtain the total error σ of the spectroscopic measurement we must consider also the uncertainty related to the reference link INRIM-LENS σ_L, shown in section 1.3.1, that leads to:

$$\sigma = \sqrt{\sigma_L^2 + \sigma_a^2} \tag{3.52}$$

In order to perform the magic wavelength measurement we have considered as reference value $\lambda_m = 759.354$ nm (see Fig. 3.4), that would corresponds to a magic frequency $\nu_m = 394.799$ THz. The three values of the lattice beams frequency chosen were $\nu_1 = 394194 \pm 2$ GHz, $\nu_2 = 394633 \pm 2$ GHz and $\nu_3 = 395112 \pm 2$ GHz, where the considered uncertainty is the one related to the wave-meter *WaveMaster* COHERENT with witch we have measured the ν_i values. We have chosen an interval of the lattice depth s between 15 and 35, in order to obtain a significant relative change remaining in every case in the Lamb-Dicke regime. The values that we have considered are

$s_1 = 31.1 \pm 0.1$, $s_2 = 23.1 \pm 0.1$ and $s_3 = 18.2 \pm 0.1$. The uncertainties that affect these values are given by the error relative to the f_{mod} evaluation.

For every lattice beams frequency we have grouped the measurements at the three different s values and we have analyzed them with a linear fit as a function of the lattice depth, since we consider only the scalar term of the light-shift as we said at the end of the section 3.3.3. The results are shown with the red, blue, yellow and green data in Fig. 3.10. The angular

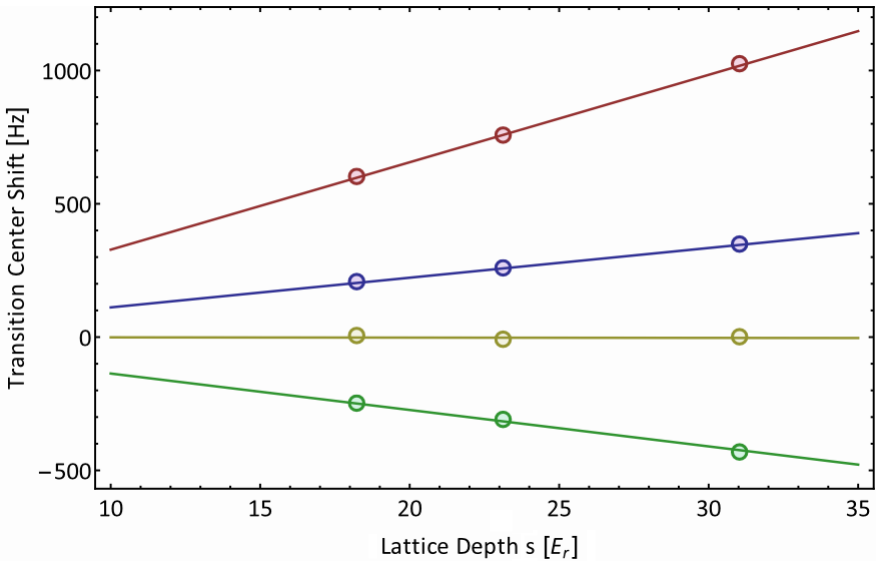

Figure 3.10: Shift of the ^{173}Yb $^1S_0 \rightarrow ^3P_0$ transition frequency versus lattice power for 4 separate lattice wavelengths. As the lattice wavelength is increased, the differential polarizability (slope of the lines) goes from negative, through zero at the magic frequency $\nu_m = 394845 \pm 5$ GHz, to positive.

coefficients of the fitted lines are plotted in Fig. 3.11 as a function of the lattice frequency. These coefficients were in turn fitted with a linear function of the beams frequency in order to obtain the intercept with the x-axis. This is justified by the fact that in the neighborhood of the magic wavelength the polarizabilities of the two electronic levels have a linear dependence on the lattice frequency, as we can see in Fig. 3.4; therefore the ac-Stark shift, proportional to the differential polarizability, is as a function of the frequency a straight line too. The result that we obtain, shown in Fig. 3.11, exhibits as magic frequency for the lattice beams the value:

$$\nu_m = 394845 \pm 5 \text{ GHz} \tag{3.53}$$

The resulting slope m represents the shift in frequency of the resonance as a function of the mismatch from the magic frequency, in unit of recoil energy; the value obtained from the fit is $\zeta = -51 \pm 1$ (mHz/E_R)*(1/GHz).

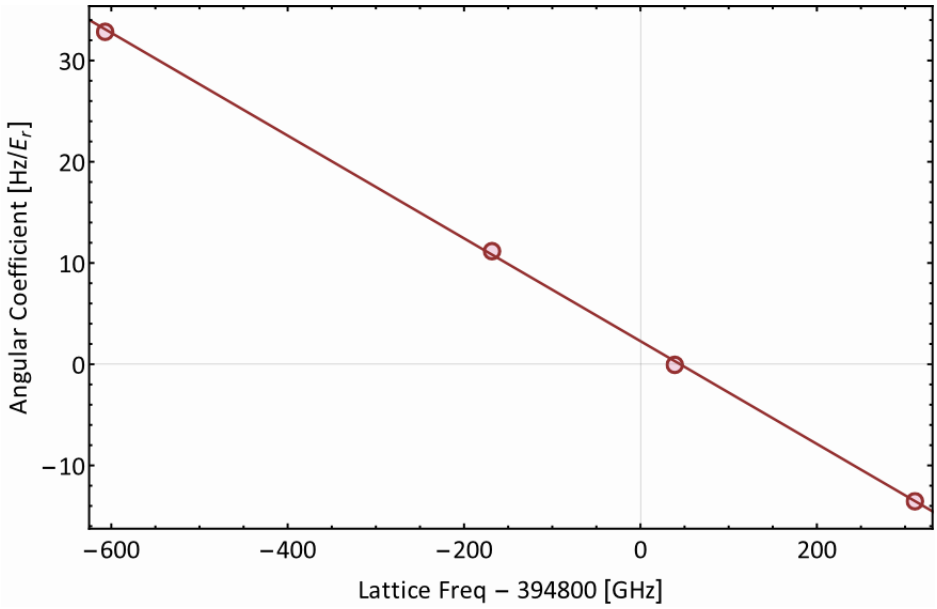

Figure 3.11: Differential polarizability plotted as a function of lattice frequency.

With reference to Eq. 3.33, the ac-Stark shift $\Delta\nu'_{eg}$ of the absolute transition frequency, considering only the scalar term of the differential polarizability Δk^S, can now be expressed as:

$$\Delta\nu'_{eg} = \zeta\Delta_\nu s \tag{3.54}$$

where $\Delta_\nu = (\nu_L - \nu_m)$ is the difference between the lattice beam frequency and $\zeta\Delta_\nu$ is exactly Δk^S. Since for the next measurements we have maintained the lattice beam frequency at the value $\nu_L = 394841 \pm 2$ GHz, we will consider $\Delta_\nu = 4$ GHz in order to estimate $\Delta\nu'_{eg}$ and its uncertainty. In fact, it will contribute to the systematic uncertainty budget of the absolute frequency measurement, carried out with a lattice depth of $[(31.1 \pm 0.1) \cdot E_R]$, with an error $\sigma_{\Delta\nu'_{eg}}$:

$$\sigma_{\Delta\nu'_{eg}} = |\sigma_s\zeta\Delta_\nu| + |\sigma_\zeta s\Delta_\nu| + |\sigma_{\Delta_\nu}\zeta s| \tag{3.55}$$

where σ_s, σ_ζ and σ_{Δ_ν} are the uncertainty relative to s, ζ and Δ_ν, respectively. The error on Δ_ν is:

$$\sigma_{\Delta_\nu} = \sqrt{\sigma^2_{\nu_m} + \sigma^2_{\nu_L}} = \sqrt{5^2 + 2^2}\ \text{GHz} \simeq 5.4\ \text{GHz} \tag{3.56}$$

Therefore the contribution to the absolute frequency uncertainty at lattice frequency $\nu_L = 394841 \pm 2$ GHz is:

$$\sigma_{\Delta\nu'_{eg}} \simeq 8.7\ \text{Hz} \tag{3.57}$$

and finally the light shift is:

$$\Delta\nu'_{eg} = -6.3 \pm 8.7 \text{ Hz} \tag{3.58}$$

3.5.3 Quadratic Zeeman contribute

In this section we will discuss the evaluation of the quadratic Zeeman shift term. For this purpose we have performed $^1S_0 \rightarrow ^3P_0$ transition frequency measurements at various values of magnetic field, in the range between 3 G and 60 G.

The measurements for the transition frequency were performed on the same system as for the magic wavelength evaluation, a two-spin system with {-5/2,+5/2} mixture, and therefore we have analyzed them in the same way. It is evident that in order to perform correctly the evaluation of the systematic quadratic Zeeman shift a correct assessment of the magnetic field is necessary. About this, the distance $\Delta\nu_r$ between the two resonance peaks depends only on the linear Zeeman term and therefore from its value we can determine the magnetic field value. So we have performed several measurements of the $^1S_0 \rightarrow ^3P_0$ transition peaks distance of the {-5/2,+5/2} spin mixture and evaluated the magnetic field value (see Eq. 3.24):

$$B = \frac{\Delta\nu_z^{(1)}}{113 \ \frac{\text{Hz}}{\text{G}}} \Delta m_F = \frac{\Delta\nu_r}{113 \ \frac{\text{Hz}}{\text{G}}} 5 \tag{3.59}$$

Moreover, from the numerous sets of measurements performed on the transition we can obtain information regarding the precision with which we generate the magnetic field. In fact, the stability of the distance between the peaks for a fixed magnetic field value reflects exactly the precision that we have on the magnetic field. An evaluation of this uncertainty is reported in Fig. 3.12. The error bars are given by the uncertainty σ of the center of the spectroscopic measurement of the two resonances as expressed in Eq. 3.52; we can consider the value of the standard deviation of the measurements set, of the order of 0.03 G, as global uncertainty for the stability of the magnetic field.

Taking this into account, we have performed the measurement of the resonance frequency for five values of magnetic field, whose results are shown in Fig. 3.13. The points represent the average of the two resonance centers as a function of the magnetic field (in this case the error bars are too small to be shown). The points are fitted with a quadratic function in order to evaluate the quadratic Zeeman coefficient η expressed in Eq. 3.25. The experimental result is $\eta = -0.065 \pm 0.002$ Hz/G^2. In Fig. 3.13 we have removed a constant

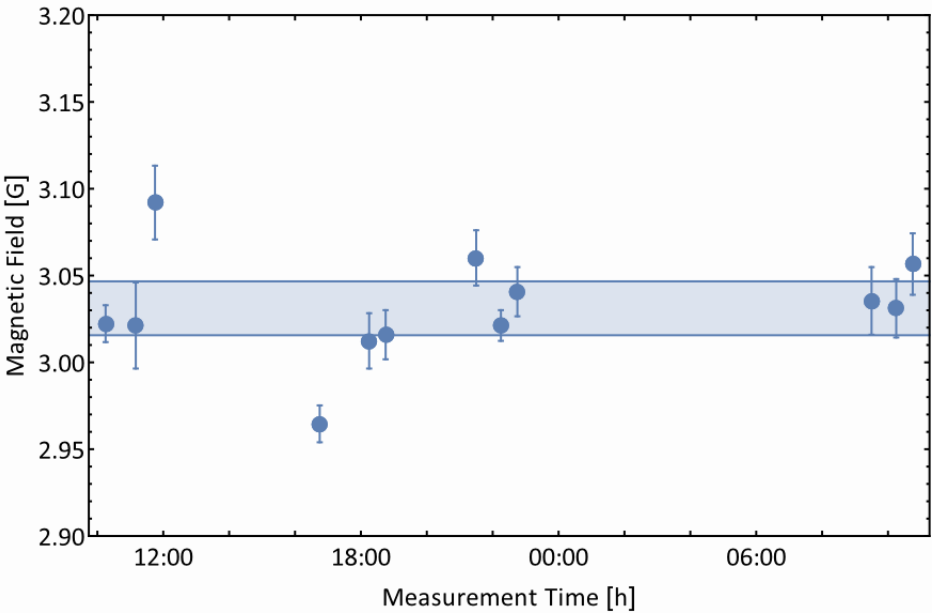

Figure 3.12: Plot of the magnetic field value for various measurement datasets as a function of the acquisition time, extracted by the linear Zeeman shift obtained from the transition peaks distance of the {-5/2,+5/2} spin mixture. This measurements was carried out in days 08/03/2015 and 08/04/2015. The error bars are given by the uncertainty of the center of the two resonances and the highlight region indicates the magnetic field values inside the standard deviation uncertainty.

frequency bias due to the fact that the measurement for the setpoint of the 578 nm laser frequency, discussed in section 3.4, has carried out at a field $B \neq 0$ and at a lattice frequency different from the magic one of about 200 GHz: this has conducted to residual linear Zeeman and ac-Stark shifts, that are quantified in the next section. It is simply an offset with respect to the transition frequency and therefore its subtraction doesn't change the uncertainty on our evaluation of the quadratic Zeeman shift. The evaluated quadratic Zeeman shift $\Delta\nu_z^{(2)}$ of Eq. 3.25 and its uncertainty contribution to the absolute frequency for the measurement value $B = 3.04 \pm 0.03$ G are:

$$\Delta\nu_z^{(2)} = \eta B^2 \simeq -0.060 \text{ Hz} \tag{3.60}$$

$$\sigma_{\Delta\nu_z^{(2)}} = B^2\Delta\sigma_\eta + 2B\eta\sigma_B \simeq 0.03 \text{ Hz} \tag{3.61}$$

This uncertainty represents a negligible contribution with respect to the errors related to the magic frequency and to the spectroscopy linewidths.

Finally, another contribution on the absolute frequency uncertainty is the light shift due to the presence of the exciting radiation at 578 nm, called probe

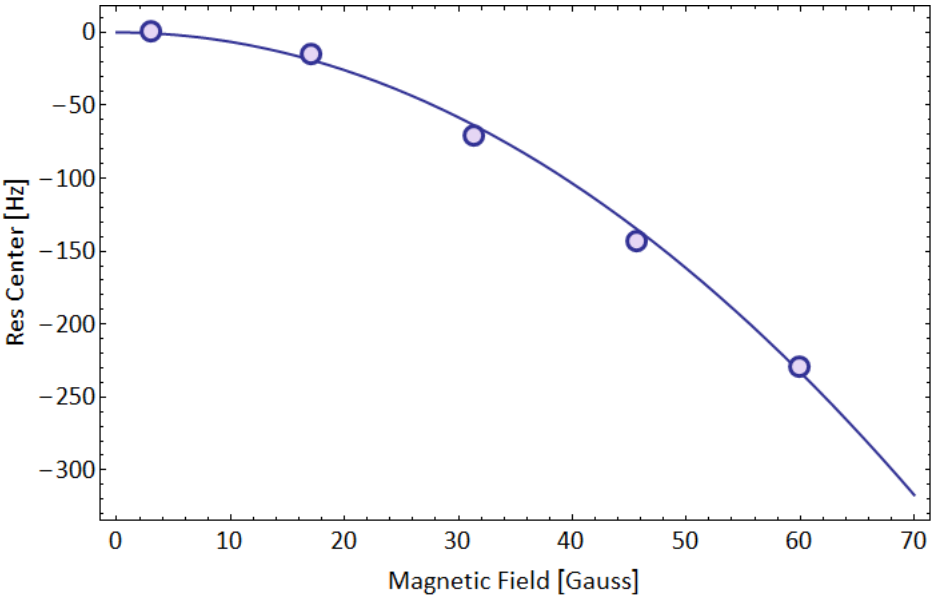

Figure 3.13: Plot and quadratic fit of $^1S_0 \rightarrow {}^3P_0$ transition frequency as a function of the magnetic field.

light shift. This shift is induced by the nonresonant interaction of the probe light with other atomic levels and could be important for large intensities and narrow clock transitions. The shift coefficient in Yb is 17 mHz/(mW/cm^2) [31], that corresponds to a shift < 1 mHz in our typical measurements with power $P \sim 1$ μW and a waist $w_0 = 1$ mm: completely negligible with respect to the other terms of the systematic uncertainty budget.

3.6 Absolute transition frequency evaluation

After having discussed the various elements concerning the evaluation of the systematic effects in the absolute transition frequency and the relative uncertainty, in this section we describe and report its measurement.

The specific experimental conditions were a magnetic field of $B = 3.04 \pm 0.03$ G, a 578 nm laser power of ~ 600 nW for an excitation time $t_e = 100$ ms, a lattice depth $s = 31.1 \pm 0.1$ and a lattice frequency $\nu_L = 394841 \pm 2$ GHz. Each experimental cycle, corresponding to the production of the ultracold sample and to its interrogation, lasts 32 s. The two-spin mixture is $m_F = \{-5/2, +5/2\}$, with a number of atoms $\sim 20 \cdot 10^3$ for each spin component. The temperature of the atomic cloud is $T \simeq 0.2\ T_F \simeq 20$ nK, with T_F the Fermi temperature for a degenerate ^{173}Yb gas. In order to obtain a statistics of at least three data for every 578 nm laser frequency value and as a test

of the laser and link stability, the measurement was held for about 12000 s. In Fig. 3.14 we report the spectroscopy measurement: we plot the number of atoms in the ground state after the excitation pulse as a function of the laser frequency. The error bars are evaluated as the standard deviations of the various measurements at the same frequency. The line is a lorentzian fit of the data.

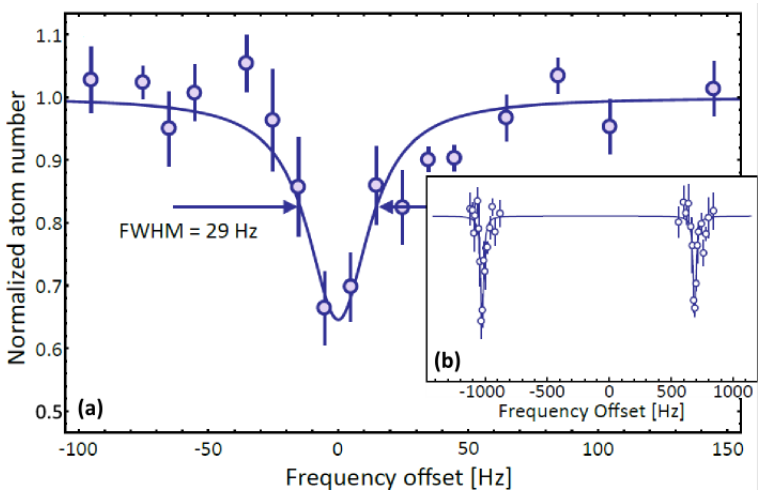

Figure 3.14: Spectrum of the ^{173}Yb $^1S_0 \rightarrow {}^3P_0$ transition carried out on the spin mixture {-5/2,+5/2} with an acquisition time of about 11800 s with a 578 nm laser power of $P_e < 1$ μW and an excitation time of $t_e = 100$ ms. **(a)** Resonance for the $m_F = -5/2$ spin component (re-centered in 0 on the x-axis). **(b)** Spectroscopy of the $m_F = \{-5/2, +5/2\}$ spin mixture.

We have evaluated the average of the two single-resonance centers and we have obtained that the spectroscopy resonance center is $\nu_a = -167.6 \pm 1.4$ Hz. Recalling Eq. 3.51, the error is given by the mean square root of the uncertainties on the center of the single resonances. This bias represents the residual Zeeman and ac-Stark shifts due to the fact that the measurement for the setpoint of the 578 nm laser frequency shown in Fig. 3.6 was carried out at different magnetic field and lattice frequency conditions from the ones of this measurement.

Considering what has been said so far in this chapter, we can now estimate the absolute transition frequency of the clock transition for ^{173}Yb. First of all with reference to the section 3.4 we must add the 578 nm laser frequency f_s: 518 294 576 845 406.1 $\pm$ 5.3 Hz. Its uncertainty σ_L in 3.52 is related to the lock chain to the INRIM reference, where the main contributions are the uncertainty on the stability of the 578 nm laser, evaluated as the Allan deviation on the measurement time of the beatnote with the frequency

comb optical locked to the absolute INRIM reference, and the INRIM reference frequency (that affects the repetition rate of the frequency comb); these uncertainties are of the same order and, since the stabilization is performed on the 1156 nm laser, affect the 578 nm source with a 2 multiplicative factor. In this f_s value we have considered also the correction given by the discrepancy of the Hydrogen maser frequency at the time of the measurement with the respect to the reference value, extracted from the comparison with the Cesium fountain. We so obtain:

$$\nu_{abs} = 518\ 294\ 576\ 845\ 238.5 \pm 5.5 \text{ Hz} \tag{3.62}$$

At this point we should consider the systematic shifts with their uncertainties. The quadratic Zeeman shift $\Delta\nu_z^{(2)}$ and the uncertainty related to the evaluation of the magic frequency have been discussed in previous sections and evaluated in Eq. 3.60 and 3.57. However, these are not the only systematic effects that need to be taken into account.

Atomic frequency references are defined by ideal systems, with atoms in a zero-temperature environment. Since physical realizations deviate from this condition, the transition frequency has to be corrected for the black-body radiation produced by the environment. This radiation source affects the absolute frequency as an additional Stark shift, $\Delta\nu_{BB}$, that for Ytterbium at temperature equal to 300 K corresponds to a shift of $\Delta\nu_{BB} = -1.2774 \pm 0.0006$ Hz [55]. Concerning the effective ambient temperature experienced by the atomic cloud, the peculiarity of our experimental setup helps us. In fact, in a typical atomic physics experiment, the measurements are performed in a chamber where the atoms arrive directly from the oven. In this way the radiation coming from that direction is greater and rather difficult to be estimated. In our case, instead, we perform the measurements in the glass cell, away from the ovens. Therefore, we can consider the room temperature (≈ 295 K) as the effective ambient temperature.

Furthermore, the measurement is non-local and the gravity potential is substantially different in Turin and Florence, that have an orthometric height of ~ 240 m and ~ 40 m, respectively. The altitude of the measurement location enters the gravitational redshift, which produces a shift of the transition frequencies, measured in two places with an altitude difference Δh, equal to $\Delta\nu = \nu_0 g \Delta h/c^2$, where g is the gravity acceleration and ν_0 the unshifted transition frequency. The redshift correction to be applied in Florence was calculated during a dedicated geodetic campaign [56], following the methods described in [57]. This correction compensates for the Florence altitude and makes the final result valid at a zero orthometric height.

All these terms dependent on the experimental conditions have been evaluated and the results are shown in table 3.1. The total error is the square

root of the sum of all the contributions squared.

Table 3.1: Summary table of the absolute frequency evaluation of the transition $^1S_0 \rightarrow {}^3P_0$ of ^{173}Yb.

	$\nu_{\mathbf{abs}}$ [Hz]	$\mathbf{\Delta}(\nu_{\mathbf{abs}})$ [Hz]
Spectroscopy measurement:	518 294 576 845 238.5	5.5
	Correction [Hz]	**Uncertainty** [Hz]
Quadratic Zeeman:	+0.60	0.03
Magic frequency:	+6.3	8.7
Black body radiation:	+1.24	0.05
Gravitational redshift:	−2.121	0.005
Total:	518 294 576 845 245	10

In conclusion, we note that this measurement is consistent with the previous evaluation of $518\,294\,576\,847.6 \pm 4.4$ kHz [41] within the experimental uncertainties and represents an improvement on the frequency precision of over two orders of magnitude. We note that our measurement has been performed on an experimental setup that is not designed for high-precision spectroscopy, because of the very low measurement rate that is determined by the long preparation cycle. Nevertheless, the long-term remote stabilization of the clock laser that I have implemented allows the realization of long measurements, which are always referenced to the primary frequency standards. This is a first demonstration of the novel possibilities that the experimental setup for the stabilization of the ultranarrow 578 nm laser discussed in this thesis opens for experiments on ultracold Ytterium gases.

Conclusions

This thesis work was realized as a part of the experiment dedicated to the study of degenerate Ytterbium quantum gases running at *University of Florence-European Laboratory for Non-Linear Spectroscopy* (UNIFI-LENS). The main goal of the thesis was the development of a stabilization system for the an ultranarrow 578 nm clock laser (realized before this master thesis work) in order to perform quantum simulation experiments with Ytterbium ultracold gases. This laser source is used to excite the $^1S_0 \rightarrow ^3P_0$ clock transition of Ytterbium, characterized by a natural linewidth $\Gamma = 2\pi \times 6$ mHz (mean lifetime $\tau > 20$ s), in order to coherently control the electronic degree of freedom of this two-electron atom.

To realize my purpose I exploited the long-distance optical fiber link LIFT that connects *Istituto Nazionale di Ricerca Metrologica* (INRIM) in Turin to UNIFI-LENS. First of all, I characterized the stability of the 578 nm laser source performing frequency measurements using a frequency comb, stabilized with the absolute optical reference coming from INRIM. Then I implemented the experimental system in order to cancel the laser residual frequency drift. This work consisted in the realization of an experimental setup that extracts an error signal from the absolute optical reference of INRIM and automatically actuates the correction with a feed-back technique through a Direct Digital Synthesizer (DDS). This method has led to an improvement of about two orders of magnitude, from ~ 100 Hz to ~ 1 Hz, of the laser stability at 1000 s. Furthermore, the remotely-stabilized clock laser is always referenced to the primary standard operating at INRIM.

As a first application of this new experimental setup, we have performed the absolute frequency measurement of the doubly forbidden transition $^1S_0 \rightarrow ^3P_0$ of ^{173}Yb. The improved stability of the clock laser allowed us to determine the line center with a statistical uncertainty of only 5.5 Hz (corresponding to a fractional uncertainty of $1.1 \cdot 10^{-14}$). Furthermore, we have performed experimental studies of several systematic effects, including the quadratic Zeeman shift and the ac-Stark shift induced by the optical lattice trapping light. The evaluated absolute transition frequency is $\nu_{abs} = 518\,294\,576\,845\,245 \pm 10$ Hz,

consistent with previous evaluation within the experimental uncertainties and represents an improvement on the precision of this frequency value of over two orders of magnitude.

This is a clear demonstration of the utility of an optical fiber link for atomic physics experiments. We note that the absolute frequency measurement reported in this thesis has been performed on an experimental setup that is not designed for high-precision spectroscopy, because of the very low measurement rate that is determined by the long preparation cycle. Nevertheless, the long-term remote stabilization of the clock laser that I have implemented allows the realization of long-lasting measurements, which are always referenced to an absolute frequency standard.

The next goals of the experiment will involve the use of the $^1S_0 \rightarrow ^3P_0$ transition for quantum simulation applications. The new setup that I have implemented could significantly expand the range of experiments that it is possible to perform, with the added values of long-term stability and metrological precision: among these, we mention the possibility of accurate tests of the SU(N) interaction symmetry, the use of orbital magnetic Feshbach resonances for the study of fermionic superfluidity in a new system made by atoms in different electronic states, the reliable manipulation of qubits based on the electronic state for quantum information applications.

Bibliography

[1] I. Bloch, J. Dalibard, S. Nascimbène*Quantum simulations with ultracold quantum gases*. Nat. Phys. **8**, 2012. 1, 8

[2] M. Lewenstein, A. Sanpera, V. Ahufinger, *Ultracold Atoms in Optical Lattices*. Oxford University Press, 2012. 1

[3] M. Greiner, O. Mandel, T. Esslinger, et al., *Quantum phase transition from a superfluid to a Mott insulator in a gas of ultracold atoms*. Nature **415**, 2002. 1

[4] A. V. Gorshkov, M. Hermele, V. Gurarie, et al., *Two-orbital SU(N) magnetism with ultracold alkaline-earth atoms*. Nat. Phys. **6**, 2010. 1

[5] N. Poli, C. W. Oates, P. Gill et al., *Optical atomic clocks*. La rivista del Nuovo Cimento **36**, Issue 12, 2013. 1

[6] H. S. Margolis, R. M. Godun, P. Gill et al., *International timescales with optical clocks (ITOC)*. Proceedings of the Joint UFFC, EFTF and PFM Symposium, 2013. 2, 12

[7] J. F. Cliche, B. Shillue, *Precision timing control for radioastronomy: maintaining femtosecond synchronization in the Atacama Large Millimeter Array*. IEEE Contr. Syst. Mag. **26**, 2006. 2, 12

[8] S. Schiller, *Feasibility of giant fiber-optic gyroscopes*. Phys. Rev. A **87**, 2013. 2, 12

[9] M. Mancini, G. Pagano, G. Cappellini et al., *Observation of chiral edge states with neutral fermions in synthetic Hall ribbons*. Science **349**, 2015. 2

[10] N. Poli, Z. W. Barber, N. D. Lemke et al., *Frequency evaluation of the doubly forbidden* $^1S_0 \rightarrow {}^3P_0$ *transition in bosonic* ^{174}Yb. Phys. Rev. A **77**, 2008. 7

[11] A. J. Daley, M. M. Boyd, J. Ye et al., *Quantum Computing with Alkaline-Earth-Metal Atoms*. Phys. Rev. Lett. **101**, 2008. 2

[12] N. Hinkley, J. A. Sherman, N. B. Phillips, et al., *An Atomic Clock with 10^{-18} Instability*. Science **341**, 2013. 7

[13] M. A. Cazalilla, A. M. Rey, *Ultracold Fermi gases with emergent SU(N) symmetry*. Reports on Progress in Physics **77**, 2014. 7

[14] G. Pagano, M. Mancini, G. Cappellini et al., *A strongly interacting gas of two-electron fermions at an orbital Feshbach resonance*. arXiv:1509.04256, 2015. 8

[15] M. L. Wall, A. P. Koller, S. Li et al., *Synthetic spin-orbit coupling in an optical lattice clock*. arXiv:1509.05846, 2015. 1, 8

[16] M. Mancini, *Realizzazione sperimentale di un gas quantistico degenere di atomi di Itterbio*. Master Thesis, 2012. 9

[17] G. Pagano, *Many-body physics with Ytterbium Fermi gases in optical lattices: from one-dimensional systems to orbital magnetism*. PhD Thesis, 2015. 9

[18] L. Livi, *Trasporto ottico di atomi ultrafreddi a lunga distanza*. Bachelor Thesis, 2012. 10

[19] A. Bauch, J. Achkar, S. Bize, D. Calonico et al., *Comparison between frequency standards in Europe and the USA at the 1e-15 uncertainty level*. Metrologia **43**, 109–120, 2006. 11

[20] C. Daussy, O. Lopez, A. Amy-Klein et al., *Long-distance frequency dissemination with a resolution of* 10^{17}. Phys. Rev. Lett. **94**, 203904, 2005. 11

[21] F. Levi, D. Calonico, A. Mura et al., *LIFT: the Italian Link for Time and Frequency*. IEEE xplore, 477-480, 2013. 12

[22] D. Calonico, E. K. Bertacco, C. E. Calosso et al., *High-accuracy coherent optical frequency transfer over a doubled 642-km fiber link*. Appl. Phys. B **117**, Issue 3, 2014. 12, 17

[23] C. Clivati *Realization of a phase-coherent optical fiber link for the comparison of remote atomic clocks*. Tesi di dottorato, 2014. 13, 34

[24] C. Clivati, D. Calonico, C. E. Calosso et al., *Planar-waveguide external cavity laser stabilization for an optical link with 10^{-19} frequency stability.* IEEE Trans. Ultrason. Ferroelectr. Freq. Contr. **58**, pp. 2582-2587 (2011). 13

[25] J. Ye, S. Cundiff, *Femtosecond optical frequency comb. Principle, Operation and Applications.* Springer, 2005. 18

[26] G. Cappellini *Sviluppo di un sistema laser per la codifica di qubit su atomi degeneri di Itterbio.* Tesi magistrale, 2012. 27

[27] L. F. Livi *Creazione di stati atomici coerenti tramite transizioni proibite in gas di fermioni ultrafreddi.* Tesi magistrale, 2014. 27, 30

[28] G. Cappellini, P. Lombardi, M. Mancini et al., *A compact ultranarrow high-power laser system for experiments with 578 nm Ytterbium clock transition.* Rev. Sci. Instrum. **86**, 073111, 2015. 29, 60

[29] T.W. Hansch, B. Couillaud *Laser frequency stabilization by polarization spectroscopy of a reflecting reference cavity.* Optics Communications **35**, 3, 1980. 29

[30] E. D. Black *An introduction to Pound–Drever–Hall laser frequency stabilization.* Am. J. Phys. **69**, 1, 2001. 30

[31] Z. Barber *Ytterbium Optical Lattice Clock.* PhD Thesis, 2003. 5, 30, 54, 63, 67, 81

[32] F. M. Phelps, *Airy Points of a Meter Bar.* Am. J. Phys. **34**, 419-422, 1966. 31

[33] T. Kessler, C. Hagemann, C. Grebing et al., *A sub-40-mHz-linewidth laser based on a silicon single-crystal optical cavity.* Nat. Phot. **6**, 2012. 32

[34] G. Cappellini, M. Mancini, G. Pagano et al., *Direct Observation of Coherent Interorbital Spin-Exchange Dynamics.* Phys. Rev. Lett. **113**, 120402, 2014. 8, 31

[35] D. W. Allan *Statistics of Atomic Frequency Standards.* Proc. of the IEEE **54**, 2, 1966. 34, 37

[36] D.A. Howe, D.W. Allan and J.A. Barnes *Properties of signal sources and measurement methods.* pages 464–469, Frequency Control Symposium 35, 1981. 35

[37] Erik Benkler, Christian Lisdat, Uwe Sterr *On the relation between uncertainties of weighted frequency averages and the various types of Allan deviations*. Metrologia **52**, 2015. 40

[38] Lionel Cordesses *Direct Digital Synthesis: a Tool for Periodic Wave Generation*. Signal Processing Magazine, IEEE (Volume:21 , Issue: 4). 2004. 44

[39] http://www.analog.com/en/products/rf-microwave/direct-digital-synthesis-modulators/ad9910.html#product-documentation. 44

[40] 0. A. Howe, 0. W. Allan, and J. A. Barnes *Properties of Signal Sources and Measurement Methods*. Proceedings of the 35th Annual Symposium on Frequency Control, 1981. 49

[41] C.W. Hoyt, Z.W. Barber, C.W. Oates et al., *Observation and Absolute Frequency Measurements of the* $^1S_0 \rightarrow {}^3P_0$ *Optical Clock Transition in Neutral Ytterbium*, Phys. Rev. Lett. **95**, 083003, 2005. 51, 84

[42] R. Santra, K. V. Christ, C. H. Greene, *Properties of metastable alkaline-earth-metal atoms calculated using an accurate effective core potential*. Phys. Rev. A, **69**, 042510, 2004. 54

[43] B.G. Wybourn and L. Smentek, *Optical Spectroscopies of Lanthanides: magnetic and hyperfine interactions*. CRC press, 2007.

[44] M. Weissbluth, *Atoms and Molecules*. Academic Press, 1978.

[45] S. G. Porsev, A. Derevianko, *Hyperfine quenching of the metastable* $^3P_{0,2}$ *states in divalent atoms*. Phys. Rev. A **69**, 042506, 2004. 52

[46] S. Taie, Y. Takasu, S. Sugawa et al., *Realization of a SU(2)×SU(6) System of Fermions in a Cold Atomic Gas*. Phys. Rev. Lett. **105**, 2010. 58

[47] R. Grimm, Matthias Weidemüller *Optical Dipole Traps for Neutral Atoms*. Advances In Atomic, Molecular, and Optical Physics, Vol. **42**, 2000. 58

[48] S. Taie, Y. Takasu, S. Sugawa et al., *Realization of a SU(2) X SU(6) System of Fermions in a Cold Atomic Gas*. Phys. Rev. Lett. **105**, 190401, 2010. 59

[49] S. G. Porsev, A. Derevianko, E. N. Fortson, *Possibility of an optical clock using the* $6^1S_0 \rightarrow 6^3P_0^0$ *transition in* $^{171,173}Yb$ *atoms held in an optical lattice.* Phys. Rev. A **69**, 021403, 2004. 62

[50] M. M. Boyd, T. Zelevinsky, A. D. Ludlow et al., *Nuclear spin effects in optical lattice clocks.* Phys. Rev. A **76**, 022510, 2007. 65

[51] V. A. Dzuba, A. Derevianko, *Dynamic polarizabilities and related properties of clock states of the ytterbium atom.* J. Phys. B: At. Mol. Opt. Phys. **43**, 2010. 5, 6, 65

[52] Z. W. Barber, J. E. Stalnaker, N. D. Lemke et al. *Optical Lattice Induced Light Shifts in an Yb Atomic Clock.* Phys. Rev. Lett. **100**, 103002, 2008. 65, 66

[53] M. Inguscio, L. Fallani, *Atomic Physics: precise measurements & ultracold matter.* Oxford University Press, 2013. 61, 70

[54] B. Hundt, *Momentum-Resolved Optical Lattice Modulation Spectroscopy on Bose-Fermi Mixtures.* Diploma Thesis, 2011. 73

[55] K. Beloy, J. A. Sherman, N. D. Lemke et al., *Determination of the* $5d6s^3D_1$ *state lifetime and blackbody-radiation clock shift in Yb.* Phys. Rev. A **86**, 2012. 83

[56] A. Cina, private communication. 83

[57] D Calonico, A. Cina, I. H. Bendea et al., *Gravitational redshift at INRIM.* Metrologia **44**, 2007. 83